EFFICIENT COMPUTATION OF LAYERED MEDIUM GREEN'S FUNCTION AND ITS APPLICATION IN GEOPHYSICS

A Dissertation

Presented to

the Faculty of the Department of Electrical and Computer Engineering

University of Houston

In Partial Fulfillment

of the Requirements for the Degree

Doctor of Philosophy

in Electrical Engineering

by

Dawei Li

May 2016

EFFICIENT COMPUTATION OF LAYERED MEDIUM GREEN'S FUNCTION AND ITS APPLICATION IN GEOPHYSICS

Dawei Li

Approved:

Chair of the Committee
Ji Chen, Professor
Electrical and Computer Engineering

Committee Members:

Donald R. Wilton, Professor
Electrical and Computer Engineering

David R. Jackson, Professor
Electrical and Computer Engineering

Jiefu Chen, Assistant Professor
Electrical and Computer Engineering

Driss Benhaddou, Associate Professor
Engineering Technology

Aria Abubakar, Interpretation Engineering Manager, Schlumberger

Suresh K. Khator, Associate Dean
Cullen College of Engineering

Badri Roysam, Professor and Chair
Electrical and Computer Engineering

Acknowledgements

First and foremost, I would like to express my gratitude to my adviser Prof. Ji Chen who guided me, helped me throughout the last five years of my study at University of Houston. I am extremely grateful for the trust and freedom he gave to explore on my own. None of this work was possible without his great encouragement and support. My sincerest appreciation also goes to my co-adviser Prof. Donald R. Wilton for his generous help and patient discussions that helped me sort out the technical details of my work. I always feel happy and relieved to see his happy face when dealing with difficulties during my research. The enthusiasm, persistence working attitude towards engineering and science of my advisers has inspired me much and will continue to impact my career and life.

I am also grateful to Prof. David R. Jackson who taught me a lot about electromagnetic theory and answered many research questions. I enjoyed the insightful discussions we had. Many thanks to Prof. Stuart A. Long whose strict antenna course helped me well understand the antenna engineering.

I would also like to thank Dr. Arial Abubakar and Dr. Keli Sun in Houston Formation Evaluation Center (HFE), Schlumberger for offering the internship opportunity in summer 2014 and 2015. The amazing projects and products developed in HFE impressed me how outstanding engineering improves people's everyday life, and the experience I gained at their $R\&D$ center had a great impact on my Ph.D research.

Many thanks to the committee members of my dissertation: Dr. Jiefu Chen and Dr. Driss Benhaddou, for their great suggestions to my dissertation.

Finally, I would like to thank the colleagues and friends in the Applied Electromagnetic Lab (AEL): Dr. Yan Liu, Dr. Zubiao Xiong, Dr. Shi Feng, Dr. Xichen Guo, Dr. Jianfeng Zheng, Xin Huang, Qingyan Wang, Qi Zeng, Mengna Yang, Jingshen Liu, Ran Guo, Xiaohe Ji, Sohini Sengupta and Krishna Kota for their help and friendship.

Study and life are colorful and full of joy with their company.

Last, but not least, my deepest and warmest appreciation goes to my wife, Mrs. Xinyu Liu and my parents for their constant support, encouragement and unconditional love all these years. This dissertation is dedicated to them.

EFFICIENT COMPUTATION OF LAYERED MEDIUM GREEN'S FUNCTION AND ITS APPLICATION IN GEOPHYSICS

An Abstract

of a

Dissertation

Presented to

the Faculty of the Department of Electrical and Computer Engineering

University of Houston

In Partial Fulfillment

of the Requirements for the Degree

Doctor of Philosophy

in Electrical Engineering

by

Dawei Li

May 2016

Abstract

This dissertation is mainly focused on the efficient computation of Green's function and electromagnetic scattering problems in layered media. The layered medium Green's functions (LMGFs), together with various algorithms based on them, are particular powerful methods to solve electromagnetic problems in layered media. The significance of this work is to understand the physics of the electromagnetic wave propagation and interaction with complex scatterers in multi-layered media, and also to arrive at a few fast and efficient computational algorithms.

The LMGFs can be categorized into traditional ones and mixed-potential ones. The first type of Green's function directly calculates the field due to a dipole source and the resulting semi-analytic Sommerfeld integrals (SIs) appearing in the traditional Green's function components can be evaluated extremely fast and accurately, finding various applications in forward and inverse modeling in geophysical prospecting. The mixed-potential LMGF is mostly useful for the formulation of system matrices appearing in method of moments for solving scattering problems in layered media because of its less singular nature. For both types of LMGFs, a few techniques, such as asymptotic analysis, singularity extraction, and the weighted average method are developed for the fast convergence of the resulting generalized Sommerfeld integrals. The calculation of correction term added to the scalar potential for vertical currents, give rise to a few efficient methods for the evaluation of the so-called half-line source potential (HLSP).

In order to further reduce matrix fill time when solving 3-D problems using the method of moments, a 3-D simplex interpolation approach is developed for interpolating the spectral-domain integral terms. A simple but efficient approach is to allocate an interpolation table covering all appropriate source and test point combinations, but to populate data points on the fly only as needed. To remove

all unbounded singularities a second-level singularity extraction is also needed for curl-type operators to further regularize the spectral integrals, permitting a uniform tabulation density.

Three types of problem: geophysical prospecting, antenna, and radiation problems, are employed to demonstrate the accuracy and efficiency of our algorithm. In each case, good agreements are achieved between our results and results completed by independent approaches.

Table of Contents

List of Figures

List of Tables

Chapter 1

Introduction

The efficient and fast computation of fields in layered medium is very important in many applications, with frequencies ranging from extremely low to optical frequencies, in geophysical prospecting, remote sensing, microstrip circuits, antennas, and optical waveguides [1–14]. Layered medium Green's function (LMGF) and various technique developed based on them, are particular powerful methods to solve electromagnetic scattering problems in layered medium. This thesis is mostly aimed at investigating computational algorithms using LMGFs and improving their efficiency. Without loss of generality, this work starts from general electromagnetic theory with applications slightly emphasizing geophysical problems involving complex uniaxial anisotropic medium.

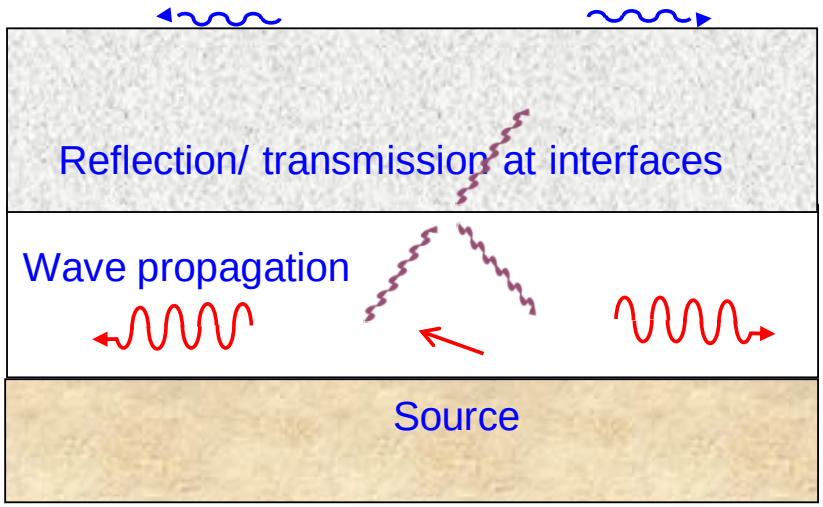

Figure 1.1. Model of planar multi-layered medium.

1.1 Dissertation Overview

The content of the thesis is organized as the following.

Chapter 2 first reviews traditional layered medium Green's function (TD-LMGF) [15]. The TD-LMGF directly calculates the electromagnetic field due to electric or magnetic dipole in a layered medium, and is particularly useful in geophysical prospecting industry [16, 17]. The formulation is based on uniaxial unisotropic medium where the electromagnetic parameters, permittivity and permeability are different in the transverse and vertical directions. The TD-LMGF is derived analytically using transmission line theory in the spectral domain and then integrating back to the spatial domain using inverse Fourier transforms. In order to accelerate the convergence of TD-LMGF, asymptotic behaviors of different components of the TD-LMGF are analyzed and their corresponding asymptotice forms are extracted. The TD-LMGF discussed here is super-hyper singular for the evaluation of impedance matrix in the integral equations formulation and thus is not proper for solving scattering problems.

In Chapter 3, the mixed-potential layered medium Green's function (MP-LMGF), which is less singular and more suitable for integral equation formulation in layered medium, is discussed. Various acceleration techniques for evaluation of MP-LMGF, for example, the discrete complex image method (DCIM) [18–24], the steepest descent path method (SDPM) [25–28] and fast Hankel transform method (FHTM) [29–31] have been developed in the last few decades. In our approach, asymptotic analysis [32], singularity extraction [33], the weighted average method [34–36], simplex interpolation [37–39] are combined for the acceleration of LMGF computation and matrix filling. The evaluation of this type of Green's function results in 14 independent Sommerfeld integrals(SIs). The calculation of scalar potential kernels give rise to the so-called half-line source potential (HLSP) [40]. Efficient evaluation of this HLSP is also important for the fast convergence of the scalar potential and several numerical approaches are developed to achieve that.

In Chapter 4, the equivalent current model is used to formulate the integral equation

based on the equivalence principle. Then the integral equation is transformed into a matrix equation in order to solve for the induced current on the surface of scatterers. The algorithms are bench-tested against reference results from other publications.

Chapter 5 discusses the second-level of singularity extraction method. In general, the spatial curl-type Green's function that appears in the MFIE, PMCHWT and hybrid FEM [41–43] formulations is more singular than the other MP-LMGFs. Using one-level of singularity subtraction, the remaining spatial integrals still contain a logarithm singularity arising from the "quasi-static" image source, which causes the interpolation scheme to lose accuracy. Hence, a higher-order asymptotic subtraction is needed in order to remove all of the unbounded behavior.

Chapter 6 applies the second-level of singularity extraction method to study the singular behavior of the curl-type Green's function, which has a great impact on the MFIE formulation. When the surface of the scatterer sits on the interface between layers, the MFIE formulation has to be corrected in order to account for the reflection from boundary [44, 45]. In this case, three different types of singular kernels, delta function singularity, logarithmic singularity and hyper-singularity coming from the image sources emerge and different transformation schemes are used to perform the source singular integration accurately.

In Chapter 7, three problems are used as examples to demonstrate the efficiency and accuracy of our algorithm. In the first example, we apply the TD-LMGF to calculate the triaxial induction tool response [46, 47], ignoring the effect of borehole and tool mandrel. Then the PMCHWT formulation is employed to calculate the tool response by taking account the borehole effect. As an second example, we apply our solvers to the modeling of an antenna sitting above the ground and sea water to observe the broadband input impedance. At last, a cubic scatter sitting on the interface between two layers excited by a vertical electric current dipole is studied.

In this case, the MFIE formulation is corrected to account for the reflection from the boundary. In all cases, numerical results show good agreements are achieved compared to independent methods. Finally, in Chapter 8, conclusions and remarks are made and several possible improvements and future research topics are discussed.

Chapter 2

Traditional Layered Medium Green's Function

In order to calculate the electromagnetic field in layered media, it's necessary to compute the layered medium Green's function (LMGF). The Green's function is the impulse response of a point dipole source in the surrounding medium or the field at an observation point due to a unit source located at some source point. Once the Green's function is known, the field due to a general source can be obtained by linear superposition.

2.1 Scalarization of Maxwell's Equation

Consider an arbitrarily-oriented electric or magnetic dipole source embedded inside a multi-layered medium, we wish to calculate the field distribution at any arbitrary point [1]. The electromagnetic parameters of each layer are the relative complex unixial anisotropic [48–51] permeability and permittivity dyadics denoted as $\underline{\underline{\boldsymbol{\mu}}} = \underline{\underline{\mathcal{I}}}_t \mu_t + \hat{\mathbf{z}}\hat{\mathbf{z}}\mu_z$ and $\underline{\underline{\boldsymbol{\varepsilon}}} = \underline{\underline{\mathcal{I}}}_t \varepsilon_t + \hat{\mathbf{z}}\hat{\mathbf{z}}\varepsilon_z$. Starting from Maxwell's equations,

$$\nabla \times \mathbf{E} = -j\omega\mu_0 \underline{\underline{\boldsymbol{\mu}}} \cdot \mathbf{H} - \mathbf{M}, \quad \nabla \times \mathbf{H} = j\omega\varepsilon_0 \underline{\underline{\boldsymbol{\varepsilon}}} \cdot \mathbf{E} + \mathbf{J}, \tag{2.1}$$

because the medium varies only in the z direction, the field is translation invariant in the x and y directions, if we define a 2D Fourier transform pair,

$$\tilde{\mathbf{F}}(\mathbf{k}_\rho) = \int_{-\infty}^{\infty}\int_{-\infty}^{\infty} \mathbf{F}(\boldsymbol{\rho})\, e^{j\mathbf{k}_\rho \cdot \boldsymbol{\rho}} dxdy \tag{2.2}$$

and

$$\mathbf{F}(\boldsymbol{\rho}) = \frac{1}{(2\pi)^2} \int_{-\infty}^{\infty}\int_{-\infty}^{\infty} \tilde{\mathbf{F}}(\mathbf{k}_\rho)\, e^{-j\mathbf{k}_\rho \cdot \boldsymbol{\rho}} dk_x dk_y. \tag{2.3}$$

where $\boldsymbol{\rho} = x\hat{\boldsymbol{x}} + y\hat{\boldsymbol{y}}$ and apply them to Eq. (2.1), we can transform the two curl equations into the following equations in spectral domain

$$\tilde{\nabla} \times \tilde{\mathbf{E}} = -j\omega\mu_0 \underline{\underline{\boldsymbol{\mu}}} \cdot \tilde{\mathbf{H}} - \tilde{\mathbf{M}}, \quad \tilde{\nabla} \times \tilde{\mathbf{H}} = \quad j\omega\varepsilon_0 \underline{\underline{\boldsymbol{\varepsilon}}} \cdot \tilde{\mathbf{E}} \; + \tilde{\mathbf{J}}. \tag{2.4}$$

If we let the vector fields be $\tilde{\mathbf{F}} = \tilde{\mathbf{F}}_t + \hat{\mathbf{z}}\,\tilde{F}_z$, we can separate the transverse and longitudinal components of the spectral equation, yielding vector transmission line equations

$$\frac{d}{dz}\tilde{\mathbf{E}}_t = \frac{1}{j\omega\varepsilon_0\varepsilon_t}(k_t^2 - \nu^e \mathbf{k}_\rho \mathbf{k}_\rho \cdot)(\tilde{\mathbf{H}}_t \times \hat{\boldsymbol{z}}) + \mathbf{k}_\rho \frac{\tilde{J}_z}{\omega\varepsilon_0\varepsilon_z} - \tilde{\mathbf{M}}_t \times \hat{\boldsymbol{z}} \tag{2.5}$$

and

$$\frac{d}{dz}\tilde{\mathbf{H}}_t = \frac{1}{j\omega\mu_0\mu_t}(k_t^2 - \nu^e \mathbf{k}_\rho \mathbf{k}_\rho \cdot)(\hat{\boldsymbol{z}} \times \tilde{\mathbf{E}}_t) + \mathbf{k}_\rho \frac{\tilde{M}_z}{\omega\mu_0\mu_z} - \hat{\boldsymbol{z}} \times \tilde{J}_z. \tag{2.6}$$

Here $k_t = k_0\sqrt{\mu_t\varepsilon_t}$ denotes the transverse wavenumber, $k_0 = \omega\sqrt{\mu_0\varepsilon_0}$ denotes the free-space wavenumber and $\nu^e = \varepsilon_t/\varepsilon_z, \nu^h = \mu_t/\mu_z$ denote the electric and magnetic anisotropy ratios respectively. If we further define a rotated coordinate system with two orthogonal transverse unit vectors

$$\hat{\mathbf{u}} = \frac{k_x}{k_\rho}\hat{\mathbf{x}} + \frac{k_y}{k_\rho}\hat{\mathbf{y}}, \qquad \hat{\mathbf{v}} = \hat{\mathbf{z}} \times \hat{\mathbf{u}} \; = -\frac{k_y}{k_\rho}\hat{\mathbf{x}} + \frac{k_x}{k_\rho}\hat{\mathbf{y}}, \tag{2.7}$$

the transverse component of electric and magnetic fields can be expressed as

$$\tilde{\mathbf{E}}_t = \hat{\mathbf{u}}\,\tilde{E}_u + \hat{\mathbf{v}}\tilde{E}_v, \quad \tilde{\mathbf{H}}_t = \hat{\mathbf{u}}\tilde{H}_u + \hat{\mathbf{v}}\,\tilde{H}_v. \tag{2.8}$$

Substituting Eq. (2.8) into the vector transmission line equation Equation 2.5, and Equation 2.6, and Equating components in each direction yields

$$\frac{d\tilde{E}_u}{dz} = \frac{(k_z^e)^2}{j\omega\varepsilon_0\varepsilon_t}\tilde{H}_v \; + \frac{k_\rho}{\omega\varepsilon_0\varepsilon_z}\tilde{J}_z - \tilde{M}_v, \tag{2.9}$$

and

$$\frac{d\tilde{H}_v}{dz} = \quad \frac{k_t^2}{j\omega\mu_0\mu_t}\tilde{E}_u \; - \tilde{J}_u, \tag{2.10}$$

for the $\tilde{E}_u$ and $\tilde{H}_v$ components and equations

$$\frac{d\tilde{E}_v}{dz} = -\frac{k_t^2}{j\omega\varepsilon_0\varepsilon_t}\tilde{H}_u \; + \tilde{M}_u, \tag{2.11}$$

and

$$\frac{d\tilde{H}_u}{dz} = \quad -\frac{\left(k_z^h\right)^2}{j\omega\mu_0\mu_t}\tilde{E}_v + \frac{k_\rho}{\omega\mu_0\mu_t}\tilde{M}_z \; + \tilde{J}_v, \tag{2.12}$$

for the $\tilde{E}_v$ and $\tilde{H}_u$ components. The above two sets of equations characterize transverse magnetic (TM) and transverse electric (TE) waves respectively. If we further define the wave impedances as

$$Z^e = \frac{k_z^e}{\omega\varepsilon_0\varepsilon_t}, \quad Z^h = \frac{\omega\mu_0\mu_t}{k_z^h}, \tag{2.13}$$

and sources as

$$\begin{aligned} v^e &= \tfrac{k_\rho}{\omega\varepsilon_0\varepsilon_z}\tilde{J}_z - \tilde{M}_v, i^e = \; -\tilde{J}_u, \\ i^h &= -\tfrac{k_\rho}{\omega\mu_0\mu_t}\tilde{M}_z \; - \tilde{J}_v, v^h = \tilde{M}_u, \end{aligned} \tag{2.14}$$

the above equations simplify to the scalar transmission line equations below with V, I denoting $\tilde{E}_u, \tilde{H}_v$ or $\tilde{E}_v, \tilde{H}_u$ for $\alpha = e, h$ respectively

$$\begin{aligned} -\tfrac{d}{dz}V^\alpha &= jk_z^\alpha Z^\alpha I^\alpha - v^\alpha, \\ -\tfrac{d}{dz}I^\alpha &= jk_z^\alpha Y^\alpha V^\alpha \; - \; i^\alpha, \end{aligned} \qquad \alpha = e, h \tag{2.15}$$

where the superscript e or h corresponds to TM and TE wave polarization respectively. It has physical meanings that the field produce by a dipole inside the transverse anisotropic layered medium can be decoupled into TE and TM waves. They propagate through different layers with different wave impedance independently.

The above classical transmission line equation has closed-form solutions and if we write the field directly as

$$\begin{aligned} \tilde{\mathbf{E}} &= \left\langle \underline{\underline{\tilde{\mathcal{G}}}}^{EJ}; \tilde{\mathbf{J}} \right\rangle + \left\langle \underline{\underline{\tilde{\mathcal{G}}}}^{EM}; \tilde{\mathbf{M}} \right\rangle, \\ \tilde{\mathbf{H}} &= \left\langle \underline{\underline{\tilde{\mathcal{G}}}}^{HJ}; \tilde{\mathbf{J}} \right\rangle + \left\langle \underline{\underline{\tilde{\mathcal{G}}}}^{HM}; \tilde{\mathbf{M}} \right\rangle, \end{aligned} \tag{2.16}$$

the dyadic Green's function $\underline{\underline{\tilde{\mathcal{G}}}}^{EJ}$ has the form of

$$\underline{\underline{\tilde{\mathcal{G}}}}^{EJ} = -\hat{\mathbf{u}}\hat{\mathbf{u}}V_i^e - \hat{\mathbf{v}}\hat{\mathbf{v}}V_i^h + \hat{\mathbf{z}}\hat{\mathbf{u}}\frac{k_\rho}{\omega\varepsilon_0\varepsilon_z}I_i^e + \hat{\mathbf{u}}\hat{\mathbf{z}}\frac{k_\rho}{\omega\varepsilon_0\varepsilon'_z}V_v^e + \hat{\mathbf{z}}\hat{\mathbf{z}}\frac{1}{j\omega\varepsilon_0\varepsilon'_z}\left[\frac{k_\rho^2}{j\omega\varepsilon_0\varepsilon_z}I_v^e - \delta\left(z-z'\right)\right]. \tag{2.17}$$

Here ε'_z and ε_z denote the vertical relative permmitivity in source and observation layers receptively. The rest of the dyadic Green's functions can be derived similarly or found in [1].

2.2 Transmission line analogy

As we discussed above, the spectral components of the TD-LMGF are expressed using voltage and current on transmission lines which can be easily solved for. Using the transmission line analogy, the dipole source is modeled as parallel current and series voltage generator, depending on the source type and orientation. Each layer is modeled as a section of transmission line with a different characteristic impedance and propagation constant. This analogy is illustrated in Figure 2.1. In this section, we will discuss and analyze the solution of the transmission line voltage and current using different methods.

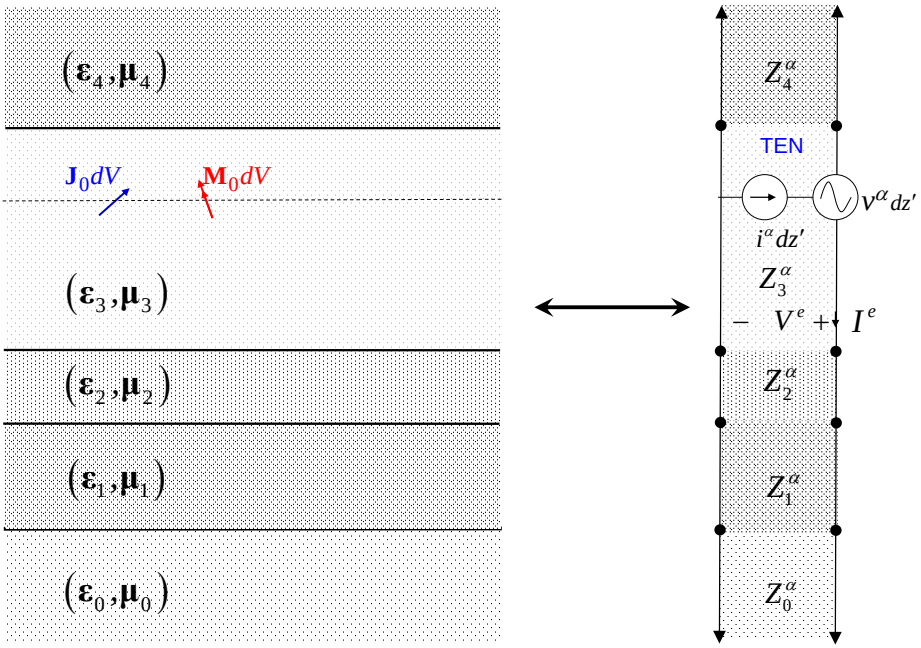

Figure 2.1. Transmission line analogy for transformed transverse fields.

2.2.1 S-Matrix Method

Calculation of voltage and current distribution using the S-Matrix can be summarized as follows:

1. Locate the layer number for source point and observation point.

2. Calculate the total impedance (TE/TM mode) looking up and down from the source point recursively, starting from the most top and most bottom layers using the equation

$$Z_{in} = Z_0 \frac{Z_L + jZ_0 \tan(k_z d)}{Z_0 + jZ_L \tan(k_z d)}. \tag{2.18}$$

3. Calculate the voltage and current right above and below the source point due to the unit series voltage and parallel current sources.

4. Use the S-Matrix to propagate the current and voltage from source point to

observation point using the equations

$$\begin{pmatrix} V_o \\ I_o \end{pmatrix} = \begin{pmatrix} \cos(k_z d) & -jZ_0 \sin(k_z d) \\ -j/Z_0 \sin(k_z d) & \cos(k_z d) \end{pmatrix} \begin{pmatrix} V_i \\ I_i \end{pmatrix}. \tag{2.19}$$

5. Substitute the obtained voltage and current for each component of the spectral-domain LMGFs.

The S-Matrix described above is a simple and elegant method to calculate the voltage and current everywhere along the transmission line. However, when the wave is evanescent, the S-Matrix may become exponentially large resulting in unstable numerical results due to numerical overflow. To be more specific, when the horizontal wavenumber k_ρ increases, the vertical wavenumber k_z approaches $-jk_\rho$ and becomes larger and larger. In this case, the element of S-Matrix becomes exponentially large and the resulting voltage and current will first start to oscillate and eventually blow up from numerical point of view. This will cause convergence problems for Sommerfeld integrals. Hence an alternative approach is desired.

2.2.2 Propagation Method

The propagation method is a more robust way of calculating transmission line current and voltage distribution. Let us first introduce the generalized reflection coefficient in the following.

2.2.2.1 Generalized Reflection Coefficient

The generalized reflection coefficient denotes the reflection coefficient looking to the left and to the right respectively at any point of a line. The expression for the generalized reflection coefficient looking left $\overleftarrow{\Gamma}^{\alpha}_{n+1}$ and looking right $\overrightarrow{\Gamma}^{\alpha}_{n-1}$ at interface $n+1$ and $n-1$, respectively can be written as

$$\overleftarrow{\Gamma}^{\alpha}_{n+1} = \frac{\Gamma^{\alpha}_{n+1,n} + \overleftarrow{\Gamma}^{\alpha}_{n} t^{\alpha}_{n}}{1 + \Gamma^{\alpha}_{n+1,n} \overleftarrow{\Gamma}^{\alpha}_{n} t^{\alpha}_{n}}, \tag{2.20}$$

$$\overrightarrow{\Gamma}^{\alpha}_{n-1} = \frac{\Gamma^{\alpha}_{n-1,n} + \overrightarrow{\Gamma}^{\alpha}_{n} t^{\alpha}_{n}}{1 + \Gamma^{\alpha}_{n-1,n} \overrightarrow{\Gamma}^{\alpha}_{n} t^{\alpha}_{n}}, \tag{2.21}$$

where

$$\Gamma^{\alpha}_{ij} = \frac{Z^{\alpha}_{j} - Z^{\alpha}_{i}}{Z^{\alpha}_{j} + Z^{\alpha}_{i}}, \qquad t^{\alpha}_{n} = e^{-jk^{\alpha}_{zn} d_n}, \tag{2.22}$$

with d_n being the thickness of layer n. The detailed derivation of Equation 2.20 and Equation 2.21 can be found at various literature [1], [52] and will be skipped here due to the limited content.

2.2.2.2 Transmission Line Green's Function

The voltage due to the current source V^{α}_{i} will be shown below as an example; the rest of the components $V^{\alpha}_{v}, I^{\alpha}_{v}, I^{\alpha}_{i}$ can be found using the transmission line equations Eq. (2.15).

A. $m = n$

When the source and observation points are both inside layer n, as illustrated in Figure 2.2, the V^{α}_{i} can be written as the general solution [52]

$$V^{\alpha}_{i} = \frac{Z^{\alpha}_{n}}{2} e^{-jk^{\alpha}_{zn}|z-z'|} + A_n e^{-jk^{\alpha}_{zn} z} + B_n e^{jk^{\alpha}_{zn} z}. \tag{2.23}$$

At the right interface $z = z_{n+1} (z_{n+1} > z')$, we have

$$B_n e^{jk^{\alpha}_{zn} z_n} = \overrightarrow{\Gamma}^{\alpha}_{n} \left(\frac{Z^{\alpha}_{n}}{2} e^{-jk^{\alpha}_{zn}|z_{n+1}-z'|} + A_n e^{-jk^{\alpha}_{zn} z_{n+1}} \right). \tag{2.24}$$

At the left interface $z = z_n (z_n < z')$, we have

$$A_n e^{-jk^{\alpha}_{zn} z_n} = \overleftarrow{\Gamma}^{\alpha}_{n} \left(\frac{Z^{\alpha}_{n}}{2} e^{-jk^{\alpha}_{zn}|z_n-z'|} + B_n e^{jk^{\alpha}_{zn} z_n} \right). \tag{2.25}$$

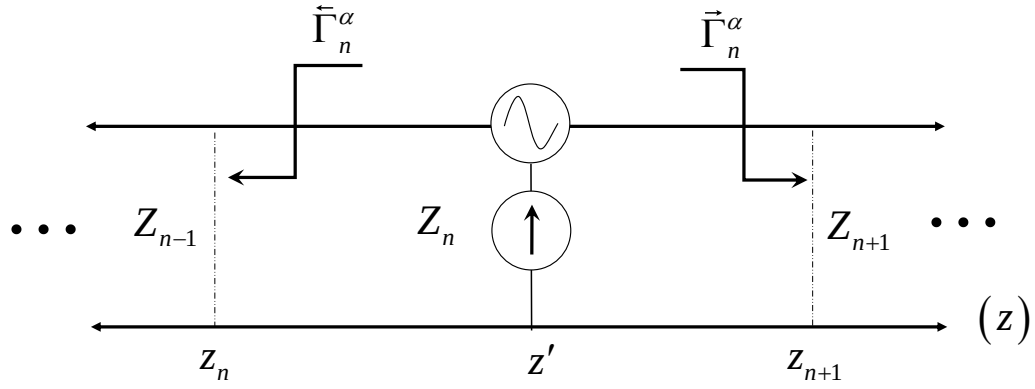

Figure 2.2. Source and observation points both in the same transmission line section.

Solving for A_n and B_n using the above two equations 2.24 and 2.25, and substituting back into Eq. (2.23), we obtain

$$V_i^{\alpha} = \frac{Z_n^{\alpha}}{2}\left[e^{-jk_{zn}^{\alpha}|z-z'|} + \frac{1}{D_n^{\alpha}}\sum_{p=1}^{4} R_{np}^{\alpha} e^{-jk_{zn}^{\alpha}\varsigma_{np}}\right], \tag{2.26}$$

where we denote

$$\begin{aligned} D_n^{\alpha} &= 1 - \overleftarrow{\Gamma}_n^{\alpha}\vec{\Gamma}_n^{\alpha} t_n^{\alpha}, R_{n1}^{\alpha} = \vec{\Gamma}_n^{\alpha}, \\ R_{n2}^{\alpha} &= \overleftarrow{\Gamma}_n^{\alpha}, R_{n3}^{\alpha} = R_{n4}^{\alpha} = \overleftarrow{\Gamma}_n^{\alpha}\vec{\Gamma}_n^{\alpha}, \end{aligned} \tag{2.27}$$

and

$$\begin{aligned} \varsigma_{n1} &= 2z_{n+1} - (z+z'), \varsigma_{n2} = (z+z') - 2z_n, \\ \varsigma_{n3} &= 2d_n + (z-z'), \varsigma_{n4} = 2d_n - (z-z'). \end{aligned} \tag{2.28}$$

B. $m < n$

In this case, we will consider the observation layer m below the source layer n and

$z < z'$. The the voltage at section $i+1$ can be written as

$$V^{\alpha}(z) = A_{i+1} e^{jk^{\alpha}_{z_{i+1}} z} \left(1 + \overleftarrow{\Gamma}^{\alpha}_{i+1} e^{-j2k^{\alpha}_{z_{i+1}} |z - z_{i+1}|}\right) \tag{2.29}$$

and the voltage at section i can be written as

$$V^{\alpha}(z) = A_i e^{jk^{\alpha}_{z_i} z} \left(1 + \overleftarrow{\Gamma}^{\alpha}_{i} e^{-j2k^{\alpha}_{z_i} |z - z_i|}\right). \tag{2.30}$$

Equating the above two equations at the junction z_{i+1} as shown in Figure 2.3

$$V^{\alpha}_{+}(z_{i+1}) = V^{\alpha}_{-}(z_{i+1}) = V^{\alpha}(z_{i+1}), \tag{2.31}$$

we have

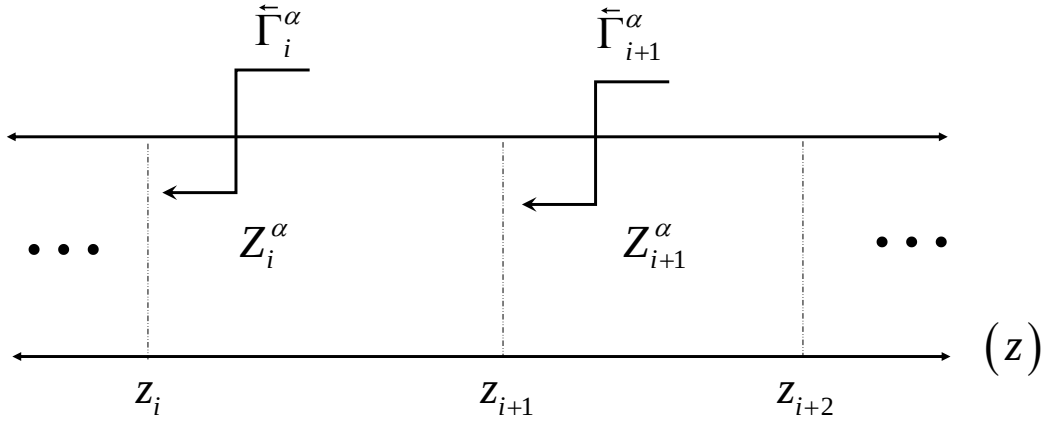

Figure 2.3. Voltage continuity at the junction z_{i+1} between section i and section $i+1$.

$$\frac{A_i}{A_{i+1}} = \frac{e^{jk^{\alpha}_{z_{i+1}} z_{i+1}} \left(1 + \overleftarrow{\Gamma}^{\alpha}_{i+1}\right)}{e^{jk^{\alpha}_{z_i} z_{i+1}} \left(1 + \overleftarrow{\Gamma}^{\alpha}_{i} e^{-j2k^{\alpha}_{z_i} d_i}\right)}. \tag{2.32}$$

Thus we can obtain the formula relating the voltage of a section from the starting

point to its endpoint by

$$\frac{V^{\alpha}\left(z_i\right)}{V^{\alpha}\left(z_{i+1}\right)}=\frac{A_i\left(1+\overleftarrow{\Gamma}_i^{\alpha}\right)e^{jk_{z_i}^{\alpha}z_i}}{A_{i+1}\left(1+\overleftarrow{\Gamma}_{i+1}^{\alpha}\right)e^{jk_{z_{i+1}}^{\alpha}z_{i+1}}}=\frac{\left(1+\overleftarrow{\Gamma}_i^{\alpha}\right)e^{-jk_{z_i}^{\alpha}d_i}}{1+\overleftarrow{\Gamma}_i^{\alpha}e^{-j2k_{z_i}^{\alpha}d_i}}. \tag{2.33}$$

Using the above relation recursively, we may propagate the voltage from $z=z_n$ to $z=z_{m+1}$ on one hand, so that

$$V^{\alpha}\left(z_{m+1}\right)=V^{\alpha}\left(z_n\right)\prod_{i=m+1}^{n-1}\frac{V^{\alpha}\left(z_i\right)}{V^{\alpha}\left(z_{i+1}\right)}. \tag{2.34}$$

On the other hand, at observation section m, the voltage $V^{\alpha}(z)$ at the observation point is related to $V^{\alpha}(z_{m+1})$ at the endpoint of section m as

$$\frac{V^{\alpha}\left(z\right)}{V^{\alpha}\left(z_{m+1}\right)}=\frac{\tau_{m,m-1}e^{-j2k_{z_m}^{\alpha}\left(z_{m+1}-z\right)}}{1+\overleftarrow{\Gamma}_m^{\alpha}e^{-j2k_{z_m}^{\alpha}d_m}},\tau_{m,m-1}=1+\overleftarrow{\Gamma}_m^{\alpha}e^{-j2k_{z_m}^{\alpha}\left(z-z_m\right)}. \tag{2.35}$$

Finally, along with Eq. (2.34), we obtain the solution

$$V^{\alpha}\left(z\right)=\frac{V^{\alpha}\left(z\right)}{V^{\alpha}\left(z_{m+1}\right)}V^{\alpha}\left(z_{m+1}\right)=V^{\alpha}\left(z_n\right)\prod_{i=m+1}^{n-1}\frac{V^{\alpha}\left(z_i\right)}{V^{\alpha}\left(z_{i+1}\right)}\frac{\tau_{m,m-1}e^{-j2k_{z_m}^{\alpha}\left(z_{m+1}-z\right)}}{1+\overleftarrow{\Gamma}_m^{\alpha}e^{-j2k_{z_m}^{\alpha}d_m}}. \tag{2.36}$$

The process of voltage propagation is illustrated in Figure 2.4.

C. $m>n$

If the observation layer is above the source layer and $z>z'$, we can repeat the derivation above to obtain the solution. However, we can also use the reciprocity principle to simplify the problem, for example, by exchanging the source position and observation position, we may be able to use the algorithm developed in the above case. The derivation of reciprocity principal for transmission line theory can be found in [53].

In the above derivation, we only analyze the V_i^{α} component. The other TLGF

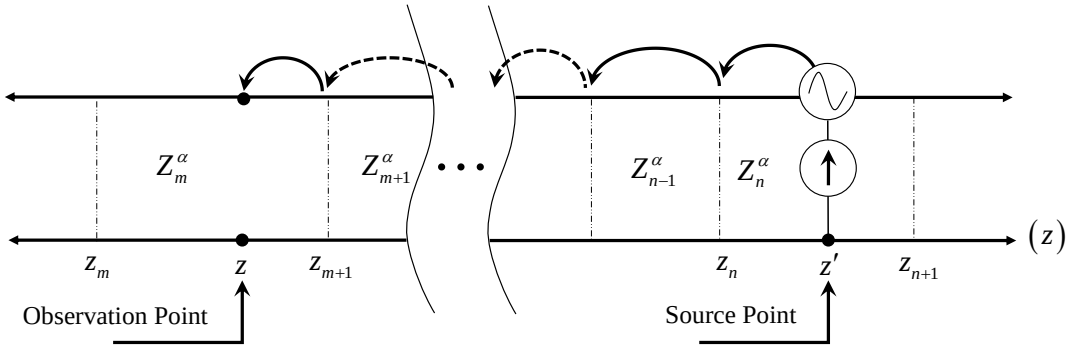

Figure 2.4. Illustration of the propagation method: voltage propagates the from source point z' to z when $z < z'$.

component V_v^α, I_v^α, I_i^α can be derived from telegraph equation similarly.

2.3 Spatial LMGF

Using inverse 2-D Fourier transform, the above spectral-domain LMGF can be converted back to the spatial domain. Because the 2-D Fourier transform is defined as a double-infinite integral, it's not efficient numerically. By introducing the Hankel transform defined in Eq. (2.37), we can reduce the double infinite integral to a single semi-infinite integral.

$$\frac{1}{(2\pi)^2}\int_{-\infty}^{\infty}\int_{-\infty}^{\infty}\begin{bmatrix}\sin n\varphi\\ \cos n\varphi\end{bmatrix}\tilde{F}\left(k_\rho\right)e^{-jk_\rho\cdot(\rho-\rho')}dk_xdk_y=(-j)^n\begin{bmatrix}\sin n\gamma\\ \cos n\gamma\end{bmatrix}S_n\left\{\tilde{F}\left(k_\rho\right)\right\}, \tag{2.37}$$

where

$$\varphi\equiv\tan^{-1}\left(k_y/k_x\right),\gamma\equiv\tan^{-1}(y-y')/(x-x'), \tag{2.38}$$

and

$$S_n\left\{\tilde{F}\left(k_\rho\right)\right\}=\frac{1}{2\pi}\int_0^\infty\tilde{F}\left(k_\rho\right)J_n\left(k_\rho\left|(\rho-\rho')\right|\right)k_\rho dk_\rho, n=0,1,2, \tag{2.39}$$

defines the Hankel transform of $\tilde{F}(k_\rho)$. The price we pay is the appearance of Bessel functions inside the integral of Eq. (2.39). With a rigorous derivation, 16 independent integrals are found and are introduced as follows to simplify of notation and calculation:

$$I_1 = S_0\left\{V_i^e + V_i^h\right\}, \quad I_2 = S_0\left\{I_v^h + I_v^e\right\}, \tag{2.40}$$

$$I_3 = S_0\left\{V_v^e + V_v^h\right\}, \quad I_4 = S_0\left\{I_i^e + I_i^h\right\}, \tag{2.41}$$

$$I_5 = S_0\left\{k_\rho^2 I_v^e\right\}, \quad I_6 = S_0\left\{k_\rho^2 V_i^h\right\}, \tag{2.42}$$

$$I_7 = S_1\left\{k_\rho V_v^e\right\}, \quad I_8 = S_1\left\{k_\rho I_i^h\right\}, \tag{2.43}$$

$$I_9 = S_1\left\{k_\rho V_i^h\right\}, \quad I_{10} = S_1\left\{k_\rho I_v^e\right\}, \tag{2.44}$$

$$I_{11} = S_1\left\{k_\rho V_v^h\right\}, \quad I_{12} = S_1\left\{k_\rho I_i^e\right\}, \tag{2.45}$$

$$I_{13} = S_2\left\{V_i^e - V_i^h\right\}, \quad I_{14} = S_2\left\{I_v^h - I_v^e\right\}, \tag{2.46}$$

$$I_{15} = S_2\left\{V_v^e - V_v^h\right\}, \quad I_{16} = S_2\left\{I_i^h - I_i^e\right\}. \tag{2.47}$$

Using the above independent integrals, the Green's function relating electric current to electric field $\underline{\underline{G}}^{EJ}$ can be expressed below with the diagonal terms being

$$G_{xx}^{EJ} = -\frac{1}{2}I_1 + \frac{1}{2}\cos 2\gamma I_{13}, \tag{2.48}$$

$$G_{yy}^{EJ} = -\frac{1}{2}I_1 - \frac{1}{2}\cos 2\gamma I_{13}, \tag{2.49}$$

$$G_{zz}^{EJ} = \frac{1}{j\omega\varepsilon_0\varepsilon'_z}\left[\frac{-1}{j\omega\varepsilon_0\varepsilon_z}I_5 - \delta\left(\boldsymbol{r}-\boldsymbol{r'}\right)\right], \tag{2.50}$$

and the off-diagonal terms being

$$G_{xy}^{EJ} = \frac{1}{2}\sin 2\gamma I_{13}, \quad G_{xz}^{EJ} = \frac{\cos\gamma}{j\omega\varepsilon_0\varepsilon'_z}I_7, \tag{2.51}$$

$$G_{yx}^{EJ} = \frac{1}{2}\sin 2\gamma I_{13}, \quad G_{yz}^{EJ} = \frac{\sin\gamma}{j\omega\varepsilon_0\varepsilon'_z}I_7, \tag{2.52}$$

$$G_{zx}^{EJ} = \frac{\cos\gamma}{j\omega\varepsilon_0\varepsilon_z} I_{12}, \quad G_{zy}^{EJ} = \frac{\sin\gamma}{j\omega\varepsilon_0\varepsilon_z} I_{12}. \tag{2.53}$$

The other Green's functions can be also derived in a similar fashion thus will not be listed here due to the limitation of context. It should be mentioned that the $\hat{z}\hat{z}$ component of the above Green's function is obtained using

$$\delta\left(\boldsymbol{\rho} - \boldsymbol{\rho'}\right) = \frac{1}{2\pi} \int_0^\infty J_0\left(k_\rho \left|\rho - \rho'\right|\right) k_\rho dk_\rho \tag{2.54}$$

or

$$\delta\left(x - x'\right)\delta\left(y - y'\right) = \frac{1}{\left(2\pi\right)^2} \int_{-\infty}^{\infty}\int_{-\infty}^{\infty} e^{-j\mathbf{k}_{\boldsymbol{\rho}}\cdot\left(\boldsymbol{\rho}-\boldsymbol{\rho'}\right)} dk_x dk_y. \tag{2.55}$$

The delta function here contributes to the field inside the source region.

2.4 Sommerfeld Integrals in TD-LMGF

As we can see, the evaluation of the TD-LMGF relies on the efficient calculation of the 16 independent integrals from Eq. (2.40) to Eq. (2.47). Evaluation of these SIs is difficult due to the presence of poles and other singularities in the complex plane [54–57]. In addition, the integrands are slowly decaying and oscillatory on the real axis. In our approach, we subtracted the corresponding asymptotic forms of the integral in the spectral domain and then restored the removed terms in spatial domain forms [33]. The removed terms are expressed as closed-form expressions which come from the radiation directly from the source or "quasi-static" images. Such asymptotic extractions result in a spectral integrand that decays faster by a factor of k_ρ^2 or more, where k_ρ is the spectral integration number, and even renders some otherwise diverging integrands integrable when the observation point is in the source plane.

Taking the geometry of Figure 2.5 as an example, the source point is at z' and the observation point is at z. The major contribution to the total field is the direct

radiated field and the reflected field coming from "quasi-static" image sources. These terms contain high spectrum components that make convergence difficult. When we are performing the integration, if we subtract these components from the integrand, the integral will converge faster. After that, the subtracted terms can be added back using available closed-form identities.

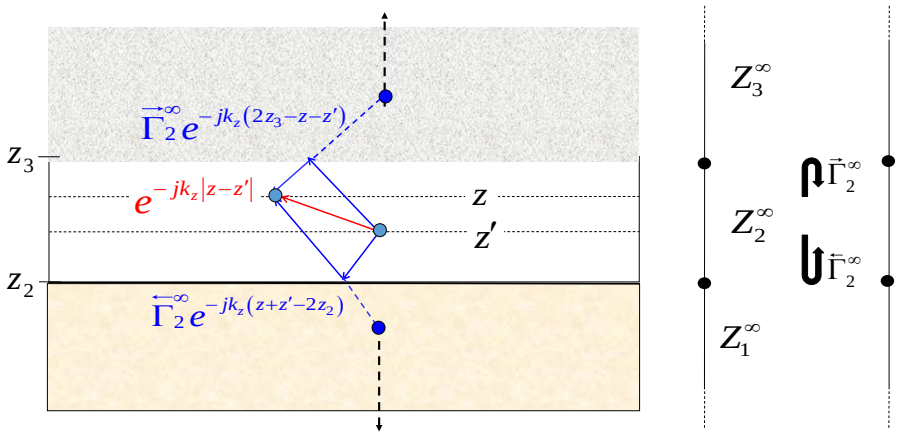

Figure 2.5. The direct and quasi-static image contributions to potential in layered media.

In the rest of this chapter, we will first perform the analysis of integrand behaviors and derive their corresponding asymptotic forms for the generalized SIs. After that, all the closed-form identities that may be useful for the TD-LMGF calculation will be introduced.

2.4.1 Integrand Behavior

The SIs that appear in spatial TD-LMGF have the form of [34]

$$I = \int_0^{\infty} \underbrace{G\left(z, z'; k_\rho\right) J_v\left(k_\rho \rho\right) k_\rho}_{f(k_\rho)} dk_\rho, v = 0, 1, 2, \tag{2.56}$$

where $G\left(z,z';k_\rho\right)$ is the spectral domain Green's function of the layered medium. Its corresponding asymptotic forms can be expressed as

$$G\left(z,z';k_\rho\right)\sim\frac{e^{-\varsigma k_\rho}}{k_\rho^{\mu}}\left[C+\mathrm{O}\left(k_\rho^{-1}\right)\right]. \tag{2.57}$$

The asymptotic behaviors of Bessel function used above for large arguments are

$$J_v\left(k_\rho\rho\right)\sim\sqrt{\frac{2}{\pi k_\rho\rho}}\cos\left(k_\rho\rho-v\frac{\pi}{2}-\frac{\pi}{4}\right),v=0,1,2. \tag{2.58}$$

Thus we have the asymptotic behavior of the integrand as

$$f\left(k_\rho\right)=\frac{e^{-\varsigma k_\rho}}{k_\rho^{d}}\sum_{i=0}^{\infty}\frac{c_i}{k_\rho^{i}}p\left(k_\rho\right),\alpha=\mu-1/2. \tag{2.59}$$

Here $p(k_\rho)$ is a periodic function ($p=2\pi/\rho,\rho>0$) behaving as *cos* or *sin* function depending on the order of the Bessel function. When $\rho=0$, it becomes to a constant. For each integrand, d is the decay order of the leading term respect to k_ρ. From transmission line theory, the asymptotic behavior of the transmission line voltage and current can be easily derived so that

$$V_i^e,I_v^h\sim\mathrm{O}\left(k_\rho e^{-k_\rho\varsigma}\right),\quad V_v^\alpha,I_i^\alpha\sim\mathrm{O}\left(e^{-k_\rho\varsigma}\right),\text{ and }V_i^h,I_v^e\sim\mathrm{O}\left(k_\rho^{-1}e^{-k_\rho\varsigma}\right). \tag{2.60}$$

According to the analysis above, the convergence of the integrand can be categorized into two types below.

Case 1: if the observation point is above or below the source plane ($\varsigma>0$), the integrand decay exponentially. The convergence of all the 16 integrals is guaranteed.

Case 2: if the observation point is exactly on the source plane ($\varsigma=0$), the integrand "decays" algebraically by the order of d . The above 16 integrand diverge in general and the singularity extraction is needed for the integrand to reach convergence.

2.4.2 Asymptotic Analysis

Before introducing the singularity extraction technique, it is necessary to discuss about the asymptotic analysis. The asymptotic form of the integrand characterizes the behavior of the integrand in the high spectrum, thus control the convergence of the integral in the spectral domain.

Starting from Fresnel reflection coefficient,

$$\overleftarrow{\Gamma}_l^{\alpha} = \frac{Z_{l-1}^{\alpha} - Z_l^{\alpha}}{Z_{l-1}^{\alpha} + Z_l^{\alpha}}, \tag{2.61}$$

for TM case, we have

$$\overleftarrow{\Gamma}_l^{e} = \frac{\left(\frac{k_z^e}{\omega\varepsilon_0\varepsilon_t}\right)_{l-1} - \left(\frac{k_z^e}{\omega\varepsilon_0\varepsilon_t}\right)_l}{\left(\frac{k_z^e}{\omega\varepsilon_0\varepsilon_t}\right)_{l-1} + \left(\frac{k_z^e}{\omega\varepsilon_0\varepsilon_t}\right)_l}. \tag{2.62}$$

When k_ρ becomes very large, the asymptotic reflection coefficient (ARC) looking from left is

$$\overleftarrow{\Gamma}_l^{e} \sim \overleftarrow{\Gamma}_l^{e,\infty} = \frac{\left(\sqrt{\varepsilon_t\varepsilon_z}\right)_l - \left(\sqrt{\varepsilon_t\varepsilon_z}\right)_{l-1}}{\left(\sqrt{\varepsilon_t\varepsilon_z}\right)_l + \left(\sqrt{\varepsilon_t\varepsilon_z}\right)_{l-1}}. \tag{2.63}$$

For TE case, the ARC looking from left has the corresponding term

$$\overleftarrow{\Gamma}_l^{h} \sim \overleftarrow{\Gamma}_l^{h,\infty} = \frac{\left(\sqrt{\mu_t\mu_z}\right)_{l-1} - \left(\sqrt{\mu_t\mu_z}\right)_l}{\left(\sqrt{\mu_t\mu_z}\right)_{l-1} + \left(\sqrt{\mu_t\mu_z}\right)_l}. \tag{2.64}$$

In order to calculate the ARC looking from right, we just need to replace $l-1$ to $l+1$. These ARCs are also referred as static reflection coefficients, because they have the same expression as the reflection coefficient for static electric or magnetic charge.

2.4.3 Closed-form Identities For Singularity Extraction

The singularity extraction process can be demonstrated as

$$I = \int_0^{\infty} \tilde{F}\left(k_\rho\right) J_n\left(k_\rho\rho\right) k_\rho \, dk_\rho = I^{res} + I^{ext}, \tag{2.65}$$

where $\tilde{F}(k_\rho)$ represent the spectral integrand and I^{res} and I^{ext} is the difference integral after extraction and the extracted terms

$$I^{res} = \int_0^\infty \left[\tilde{F}(k_\rho) - \tilde{F}^\infty(k_\rho)\right] J_n(k_\rho \rho)\, k_\rho\, dk_\rho \tag{2.66}$$

and

$$I^{ext} = \int_0^\infty \tilde{F}^\infty(k_\rho)\, J_n(k_\rho \rho)\, k_\rho\, dk_\rho \tag{2.67}$$

respectively with $\tilde{F}^\infty(k_\rho)$ being the asymptotic form of $\tilde{F}(k_\rho)$.

The extracted term I^{ext} is usually calculated in closed form, and a collection of Sommerfeld and related identities (SRIs) are found to be useful for accelerating the calculation of those SIs [18], [20], [58].

Firstly, let us define

$$G^\alpha = \frac{e^{-jk_t R^\alpha}}{4\pi R^\alpha}, \quad p^\alpha = e^{-jk_z^\alpha |\varsigma|} \tag{2.68}$$

with

$$R^\alpha = \sqrt{\rho^2/\nu^\alpha + z^2}. \tag{2.69}$$

Then the identities associated with zero-order Hankel transform are

$$I_A = S_0\left\{\frac{p^\alpha}{2jk_z^\alpha}\right\} = \frac{1}{\nu^\alpha} G^\alpha, \tag{2.70}$$

$$I_B = S_0\left\{\frac{p^\alpha}{2}\right\} = \frac{|\varsigma|\,\eta}{\nu^p (R^\alpha)^2} G^\alpha, \tag{2.71}$$

$$I_C = S_0\left\{\frac{jk_z^\alpha p^\alpha}{2}\right\} = \frac{G^\alpha}{(R^\alpha)^2}\left(\varsigma^2 \frac{3\eta - (k_t R^\alpha)^2}{\nu^\alpha (R^\alpha)^2} - \frac{\eta}{\nu^\alpha}\right), \tag{2.72}$$

$$I_D = S_0\left\{\frac{k_\rho^2 p^\alpha}{2\,(jk_z^\alpha)}\right\} = \frac{k_t^2 I_A + I_C}{v^\alpha}. \tag{2.73}$$

The identities associated with first-order Hankel transform are

$$I_E = S_1\left\{\frac{p^\alpha}{2k_\rho}\right\} = \frac{R^\alpha e^{-jk_t|\varsigma|} - |\varsigma|\, e^{-jk_t R^\alpha}}{4\pi\rho R^\alpha}, \tag{2.74}$$

$$I_F = S_1\left\{\frac{k_\rho p^\alpha}{2jk_z^\alpha}\right\} = \frac{\rho\eta}{(\nu^\alpha)^2}\frac{G^\alpha}{(R^\alpha)^2}, \tag{2.75}$$

$$I_G = S_1\left\{\frac{k_\rho p^\alpha}{2}\right\} = \frac{1}{(\nu^\alpha)^2}\frac{\rho\,|\varsigma|}{R^\alpha}\frac{3\eta - (k_t R^\alpha)^2}{(R^\alpha)^3}G^\alpha, \tag{2.76}$$

$$I_H = S_1\left\{\frac{jk_z^\alpha p^\alpha}{2k_\rho}\right\} = \frac{jk_t e^{-jk_t|\varsigma|}}{4\pi\rho} + \frac{\rho_v^2 - jk_t R^\alpha|\varsigma|^2}{(R^\alpha)^2}\frac{G^\alpha}{\rho}, \tag{2.77}$$

$$I_I = S_1\left\{\frac{p^\alpha}{2jk_z^\alpha k_\rho}\right\} = \frac{e^{-jk_t|\varsigma|} - e^{-jk_t R^\alpha}}{4\pi jk_t\rho}, \tag{2.78}$$

and the identities associated with second-order Hankel transform are

$$I_J = S_2\left\{\frac{jk_z^\alpha p^\alpha}{2}\right\} = \frac{2}{\rho}I_H - I_C, \tag{2.79}$$

$$I_K = S_2\left\{\frac{p^\alpha}{2jk_z^\alpha}\right\} = \frac{2}{\rho}I_I - I_A, \tag{2.80}$$

$$I_L = S_2\left\{\frac{p^\alpha}{2}\right\} = \frac{2}{\rho}I_E - I_B. \tag{2.81}$$

Using the above SRIs, the original diverging generalized SIs may turn to exponentially decaying integrals after singularity extraction. The worst case appears when the observation and source points are both on the layer interface when the static image point coincides with the observation point. Since the reflected spectrum doesn't have a closed-form expression in general, a integrand that decay faster by a factor of k_ρ^2 in the spectral domain can be obtained by extracting the leading-order asymptotic terms.

2.4.4 Weighted Average Method

Using the above singularity extraction, the remaining integrand differences still may be highly oscillating functions when the observation point and source point are near the layer interface. To further accelerate the convergence of those SIs, the

weighted average method (WAM) [34] is analyzed and employed.

Let us define

$$S = \int_a^{\infty} f(\xi)d\xi = \sum_{i=0}^{\infty} u_i \quad \text{with} \quad u_i = \int_{\xi_{i-1}}^{\xi_i} f(\xi)d\xi, \tag{2.82}$$

where $a < \xi_0 < \xi_1 < \xi_2 < \cdots$ and $\lim_{n\to\infty}\xi_n \to \infty$ is a sequence of break points selected according to the asymptotic behavior of the integrand, for example, the zero point or local peak point. Then the integral can be written as a summation of

$$S_n = \sum_{i=0}^{n} u_i, \tag{2.83}$$

with a remainder integral defined as

$$r_n = S_n - S = -\int_{\xi_n}^{\infty} f(\xi)d\xi. \tag{2.84}$$

The current extrapolation techniques all focus on the acceleration of this integral remainder. Among them, the weighted average method is one of the most robust and efficient methods. Below we review and illustrate the theory of the weighted average method briefly.

The weighted average method defines a translated series,

$$S'_n = \frac{W_n S_n + W_{n+1} S_{n+1}}{W_n + W_{n+1}} = S + \frac{r_n + \eta r_{n+1}}{1+\eta}, \tag{2.85}$$

ideally, if we choose

$$\eta = -\frac{r_n}{r_{n+1}}, \tag{2.86}$$

then S'_n= S suggests the translated finite integrals are the exact infinite integrals. Because r_n do not have a closed form in general, the leading term of its asymptotic

form is used to estimate the coefficient η. For example, the asymptotic analysis shows that the remainder behaves as

$$r_n \sim a_0 w_n + \mathrm{O}\left(\xi_n^{-1}\right) \quad \text{with} \quad w_n = (-1)^{n+1} \frac{e^{-nq\varsigma}}{\xi_n^{\alpha}}, \tag{2.87}$$

thus we have

$$\frac{r_n}{r_{n+1}} = \frac{w_n}{w_{n+1}} \left(1 + \frac{a_1 q}{a_0 \xi_n \xi_{n+1} + a_1 \xi_n}\right) \sim \frac{w_n}{w_{n+1}} \left(1 + \mathrm{O}\left(\xi_{n+1}^{-2}\right)\right). \tag{2.88}$$

If we choose $\eta = -\frac{w_n}{w_{n+1}}$, then

$$1 + \eta = 1 - \frac{w_n}{w_{n+1}} = 1 + e^{-q\varsigma} \frac{\xi_{n+1}}{\xi_n} \sim \mathrm{O}\left(1\right), \tag{2.89}$$

and the translated remainder behaves asymptotically as

$$\frac{{r'}_n}{r_n} = \frac{r_n + \eta r_{n+1}}{r_n + \eta r_{n+1}} = \frac{1 + \eta \frac{r_{n+1}}{r_n}}{1 + \eta} \sim \frac{1 - \frac{w_n}{w_{n+1}} \frac{w_{n+1}}{w_n} \left[1 + \mathrm{O}\left(\xi_n^{-2}\right)\right]}{\mathrm{O}\left(1\right)} \sim \mathrm{O}\left(\xi_n^{-2}\right). \tag{2.90}$$

This means the translated remainder becomes a scaled version of the original remainder and we can employ this approach repeatedly. The recursive process can be expressed clearly using Figure 2.6.

2.5 Numerical Examples

As a first example, we will validate the identities we introduced previously using the homogeneous medium configuration illustrated in Figure 2.7. The results are shown in the Tables 2.1, 2.2 and 2.3. The left-hand side is obtained by performing pure numerical integration and the right-hand side is calculated using closed-form expressions. Their values are the same for the decimal places shown.

As a second example, we consider a five layered stratified medium with both source point and observation point with a distance of 0.2236 m located between the interface

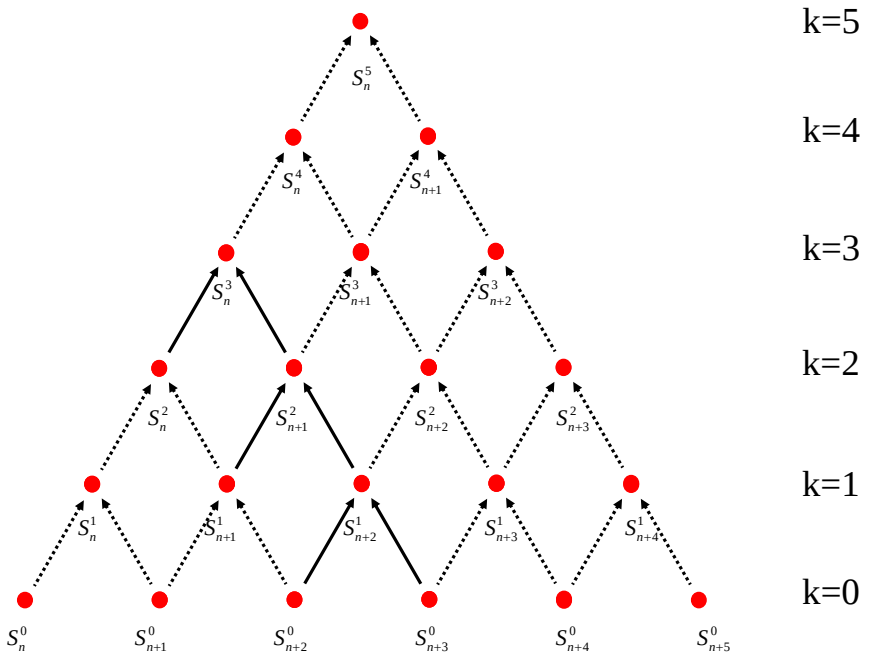

Figure 2.6. Illustration of recursive scheme for weighted average method.

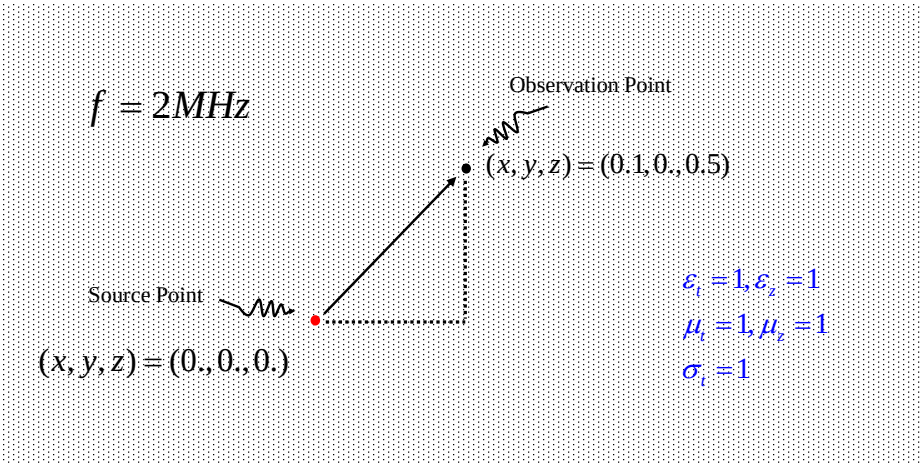

Figure 2.7. Configuration of Sommerfeld and related identities validation.

of layer 2 and layer 3 as on the left side of Figure 2.8. The frequency is set to be 2 MHz. The conductivity of each layer is listed in Figure 2.8 with unit of [S/m]. The relative permititivity and permeability of layers are set to be 1. Figure 2.9 plots the integrand in the spectral domain before and after we subtract the corresponding

Table 2.1. SIR results with $\sigma_z/\sigma_t = 2$ for TM polarization

Identity	Real(LHS)	Imag(LHS)	Real(RHS)	Imag(RHS)
A	7.8501e-03	-7.0698e-02	7.8501e-03	-7.0698e-02
B	2.2693e-01	-3.0084e-01	2.2693e-01	-3.0084e-01
C	1.8406e+00	-9.5475e-01	1.8406e+00	-9.5475e-01
D	1.4482e+00	- 2.1578e+00	1.4482e+00	-2.1578e+00
E	1.2585e-02	-1.5859e-02	1.2585e-02	-1.5859e-02
F	9.0765e-02	-1.2034e-01	9.0765e-02	-1.2034e-01
G	9.1774e-01	-6.2262e-01	9.1774e-01	-6.2262e-01
H	1.0367e-01	-5.2044e-02	1.0367e-01	-5.2044e-02
I	5.1406e-04	-3.6907e-03	5.1406e-04	-3.6907e-03
J	2.3275e-01	-8.6128e-02	2.3275e-01	-8.6128e-02
K	2.4311e-03	-3.1162e-03	2.4311e-03	-3.1162e-03
L	2.4780e-02	-1.6344e-02	2.4780e-02	-1.6344e-02

Table 2.2. SIR results with $\sigma_z/\sigma_t = 2$ for TE polarization

Identity	Real(LHS)	Imag(LHS)	Real(RHS)	Imag(RHS)
A	5.1211e-03	-3.6893e-02	5.1211e-03	-3.6893e-02
B	1.2562e-01	-1.5848e-01	1.2562e-01	-1.5848e-01
C	1.0337e+00	-5.1954e-01	1.0337e+00	-5.1954e-01
D	4.5107e-01	-6.0048e-01	4.5107e-01	-6.0048e-01
E	6.6148e-03	-8.1386e-03	6.6148e-03	-8.1386e-03
F	2.5123e-02	-3.1697e-02	2.5123e-02	-3.1697e-02
G	2.5698e-01	-1.6730e-01	2.5698e-01	-1.6730e-01
H	5.4889e-02	-2.7137e-02	5.4889e-02	-2.7137e-02
I	2.8856e-04	-1.8850e-03	2.8856e-04	-1.8850e-03
J	6.4132e-02	-2.3192e-02	6.4132e-02	-2.3192e-02
K	6.5013e-04	-8.0662e-04	6.5013e-04	-8.0662e-04
L	6.6796e-03	-4.2875e-03	6.6796e-03	-4.2875e-03

asymptotic forms. As we can see, the subtractions result in a spectral integrand decaying faster by a factor of k_ρ^2 and makes the originally divergent integral converge.

The third example validate results using singularity extraction method. We move

Table 2.3. SIR results with $\sigma_z/\sigma_t = 0.5$ for TM polarization

Identity	Real(LHS)	Imag(LHS)	Real(RHS)	Imag(RHS)
A	2.8849e-03	-1.8848e-02	2.8849e-03	-1.8848e-02
B	6.6124e-02	-8.1365e-02	6.6124e-02	-8.1365e-02
C	5.4851e-01	-2.7120e-01	5.4851e-01	-2.7120e-01
D	1.2546e-01	-1.5838e-01	1.2546e-01	-1.5838e-01
E	3.3930e-03	-4.1232e-03	3.3930e-03	-4.1232e-03
F	6.6133e-03	-8.1358e-03	6.6133e-03	-8.1358e-03
G	6.8080e-02	-4.3385e-02	6.8080e-02	-4.3385e-02
H	2.8268e-02	-1.3861e-02	2.8268e-02	-1.3861e-02
I	1.5265e-04	-9.5264e-04	1.5265e-04	-9.5264e-04
J	1.6856e-02	-6.0203e-03	1.6856e-02	-6.0203e-03
K	1.6821e-04	-2.0522e-04	1.6821e-04	-2.0522e-04
L	1.7357e-03	-1.0983e-03	1.7357e-03	-1.0983e-03

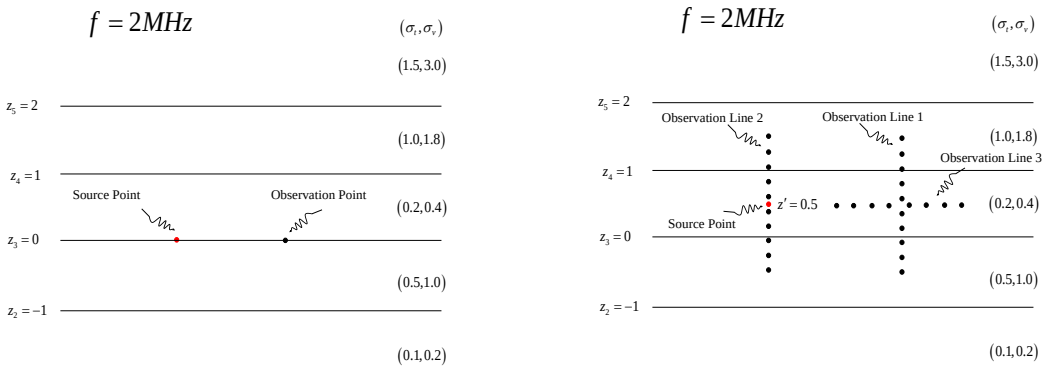

Figure 2.8. Configurations of five layers of stratified medium for (left) singularity extraction and (right) integrand observation.

the source point inside the third layer and put three observation lines with each corresponding different convergence behaviors of the integrand. The configuration is illustrated on the right side of Figure 2.8. For the first observation line ($\rho > 0$ and $\varsigma > 0$), the integrand oscillates and decays exponentially. The integral result I_1 is plotted in Figure 2.10. For the second line ($\rho = 0$ and $\varsigma > 0$), the integrand decays exponentially. The integral result I_1 is plotted in Figure 2.11. Because the integral

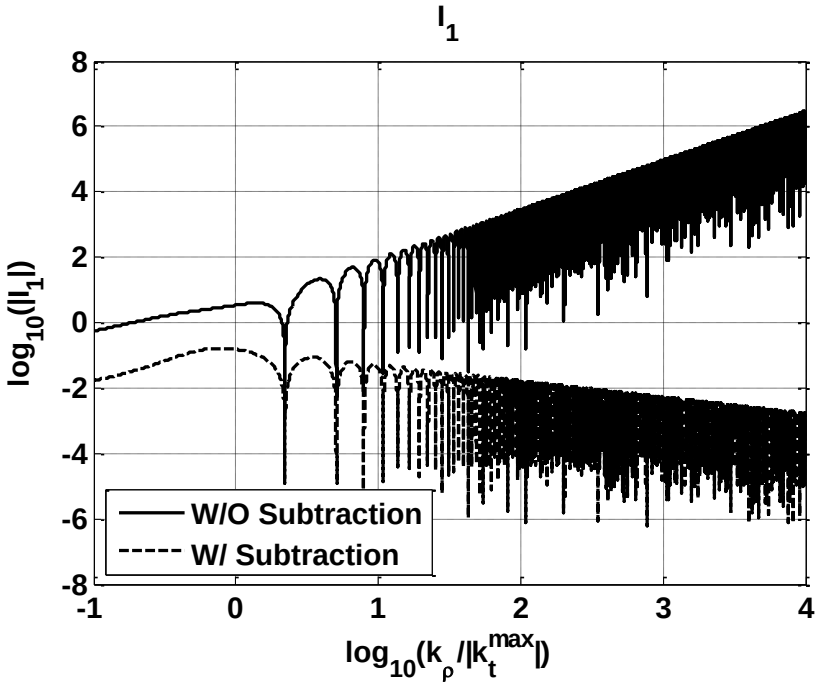

Figure 2.9. Comparison of integrand spectra for I_1 with and without singularity extraction.

blows up as we approach to the source point, a log-scale of the integral value is plotted in Figure 2.11. For the third line ($\rho > 0$ and $\varsigma = 0$), the integrand oscillates and decays algebraically and the integral result I_{16} is plotted in Figure 2.12. In this figure, the "+" and "-" indicate we approaching the source plane in a limiting sense from above or below.

As a final example, we use the Green's function developed in this chapter to calculate the field distribution due to the dipole source in layered media. The configuration and parameters of each layer is shown in Figure 2.13. The source point is located at $(x = 0, y = 0, z = -1.4)$ m and the observation line is along $(-3 < x < 3, y = 1, z = -0.3)$ m. Figure 2.14 plots the electric field if the source dipole is of electric type. Figure 2.15 plots the electric field if the source dipole is of magnetic type. This results agree well with reference [59].

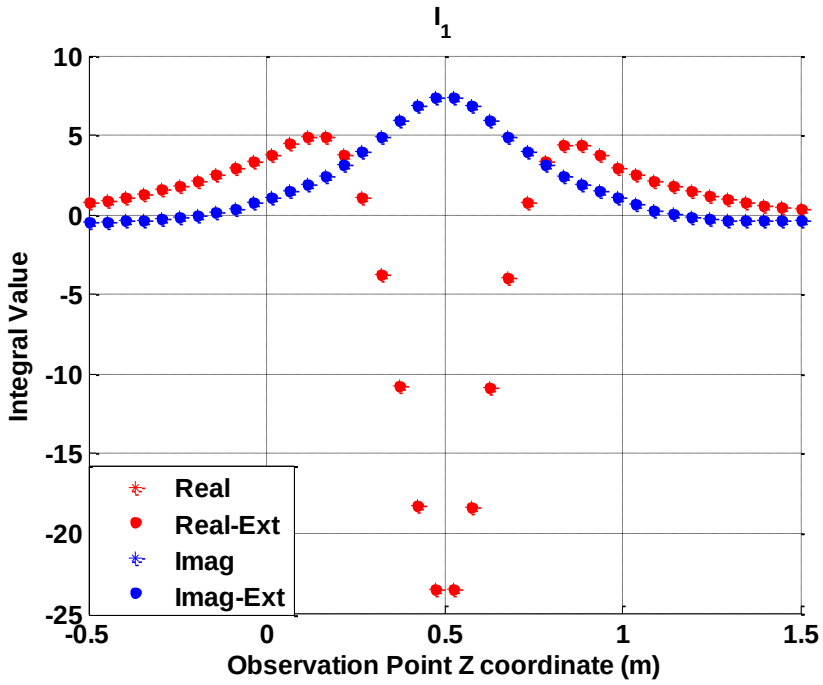

Figure 2.10. The integral I_1 on the first observation line, $\rho > 0$ and $\varsigma > 0$.

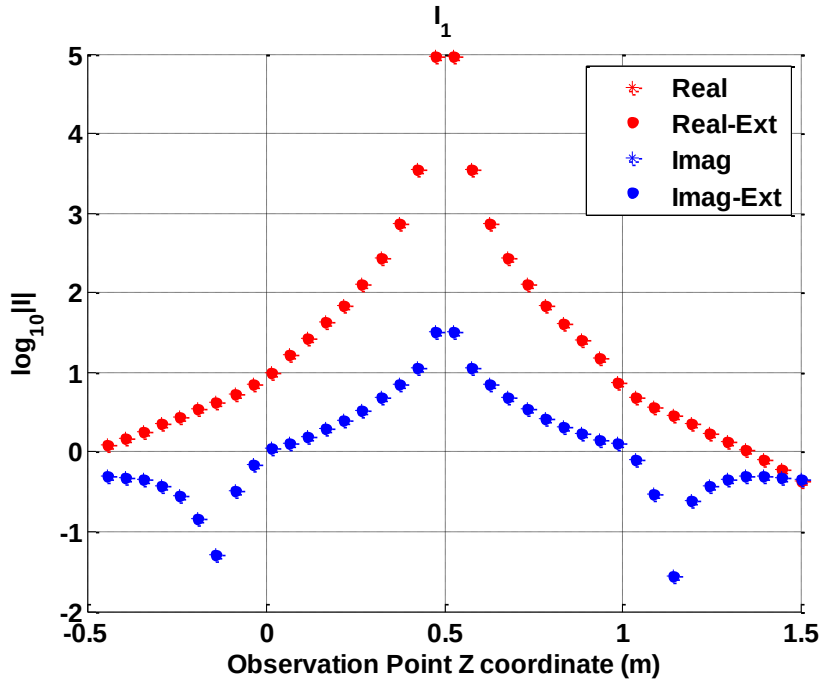

Figure 2.11. The integral I_1 on the second observation line, $\rho = 0$ and $\varsigma > 0$.

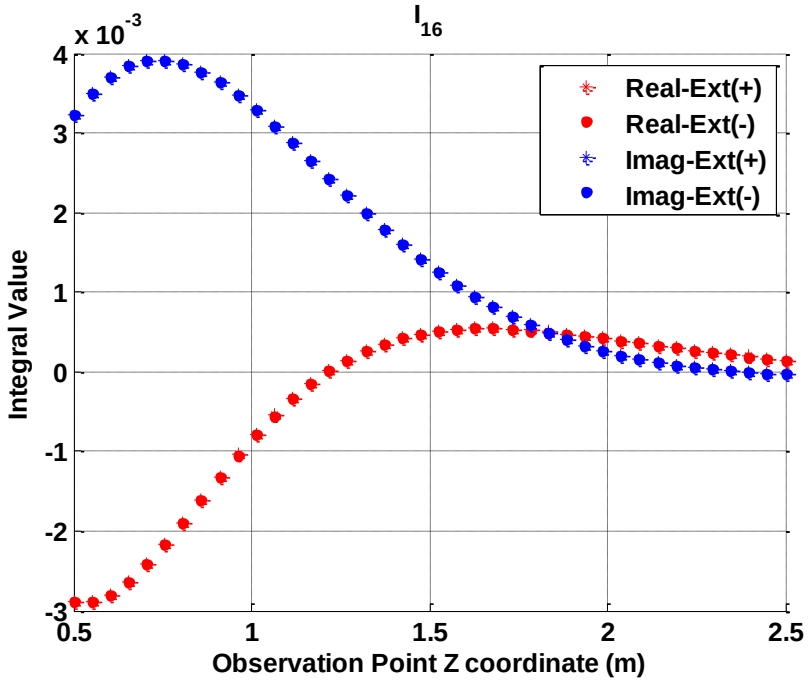

Figure 2.12. The integral I_16 on the third observation line $\rho > 0$ and $\varsigma = 0$. The "+" and "-" indicate we approach the source plane in a limiting sense from above or below.

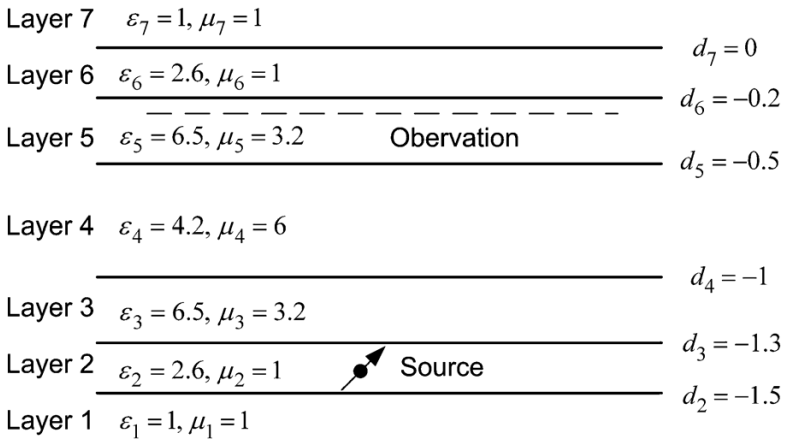

Figure 2.13. An electric or magnetic dipole is radiating in a seven-layer medium (unit: m). The operating frequency is 300 MHz, and the layer parameters are shown in the figure.

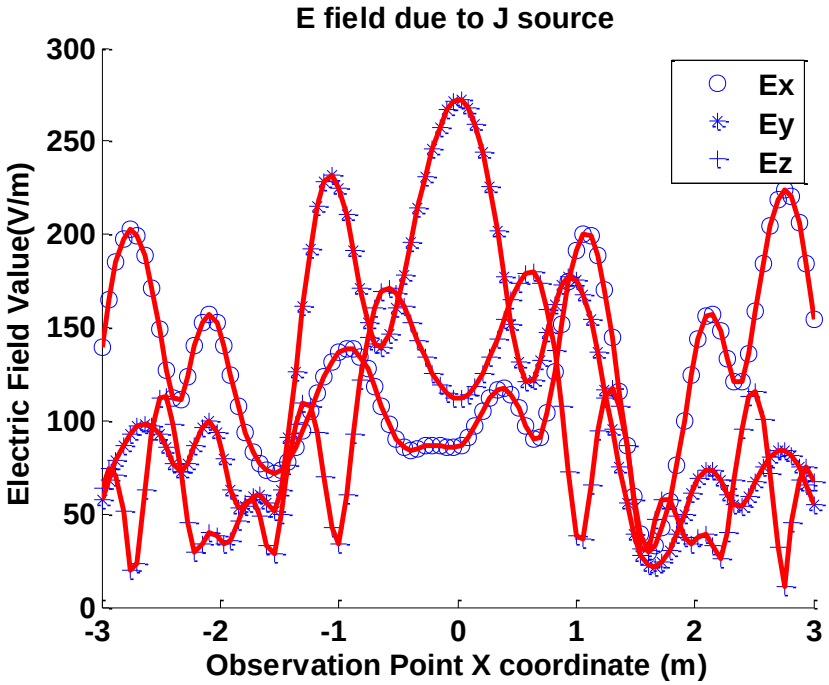

Figure 2.14. The electric field distribution on the observation line due to the electric dipole.

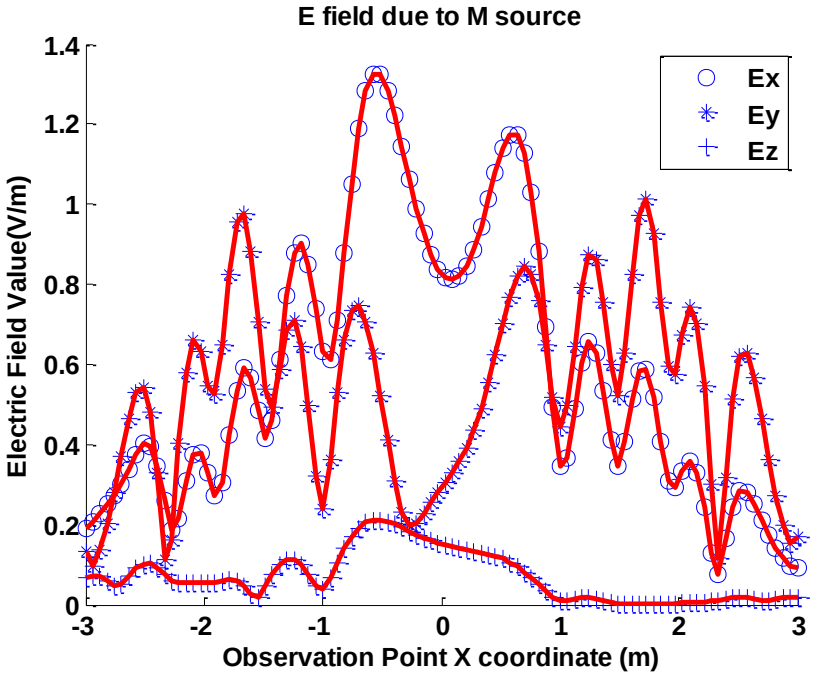

Figure 2.15. The electric field distribution on the observation line due to the magnetic dipole.

Chapter 3

Mixed-Potential Layered Medium Green's Function

When solving the currents induced on scatterers in layered media, the dyadic Green's function may be used to formulate the integral equation which are then solved by method of method. The method of moments casts the integral equations into matrix using the subspace projection method. The TD-LMGF discussed in Chapter 2 is too singular for numerical processing as its counterpart in homogeneous media. The highest singularity order is of $O(1/R^3)$ (also called super-hyper singularity) and thus is not suitable for numerical processing. In this chapter we will focus on a less singular type of LMGF that we used for integral equation.

3.1 Mixed-Potential Representation

Michalski proposed three types of mixed-potential layered medium Green's function (MP-LMGF) [60]. Among them, the type of formulation C is now widely used and most popular among computational electromagnetic society. The mixed-potential representation remove one order of singularity by taking divergence gradient respecting to the source current and remove another order of singularity by introducing a gradient respect to the observation coordinates. The resulted generalized Sommerfeld integrals (SIs) appearing in the potential kernels are less singular in spatial domain and converges fast in spectral domain.

To begin with, we can represent the electric and magnetic field as vector and scalar potentials [1]

$$\mathbf{E} = -j\omega\mathbf{A} - \nabla\Phi - \frac{1}{\varepsilon_0}\nabla\times\mathbf{F}, \quad \mathbf{H} = -j\omega\mathbf{F} - \nabla\Psi + \frac{1}{\mu_0}\nabla\times\mathbf{A}, \tag{3.1}$$

where the vector potentials are related to the electric and magnetic source via

$$\mathbf{A}(\mathbf{r}) = \mu_0 \int_S \underline{\underline{\mathcal{G}}}^A(\mathbf{r},\mathbf{r}') \cdot \mathbf{J}(\mathbf{r}')\, dS', \qquad \mathbf{F}(\mathbf{r}) = \varepsilon_0 \int_S \underline{\underline{\mathcal{G}}}^F(\mathbf{r},\mathbf{r}') \cdot \mathbf{M}(\mathbf{r}')\, dS', \quad (3.2)$$

and the scalar potentials are

$$\Phi(\mathbf{r}) = -\frac{1}{j\omega\varepsilon_0}\left(\int_S \nabla' \cdot \mathbf{J}(\mathbf{r}')\ K^{\Phi}(\mathbf{r},\mathbf{r}')\, dS' + \int_S \hat{\mathbf{z}} \cdot \mathbf{J}(\mathbf{r}')\ P_z(\mathbf{r},\mathbf{r}')\ dS'\right) \quad (3.3)$$

and

$$\Psi(\mathbf{r}) = -\frac{1}{j\omega\mu_0}\left(\int_S \nabla' \cdot \mathbf{M}(\mathbf{r}')\ K^{\Psi}(\mathbf{r},\mathbf{r}')\, dS' + \int_S \hat{\mathbf{z}} \cdot \mathbf{M}(\mathbf{r}')\, Q_z(\mathbf{r},\mathbf{r}')\ dS'\right). \quad (3.4)$$

The Green's function kernel again do not have a close form. Their dyadic and scalar components are expressed as 2D Fourier integrals below:

$$\begin{bmatrix} \underline{\underline{\mathcal{G}}}(\mathbf{r},\mathbf{r}') \\ G(\mathbf{r},\mathbf{r}') \end{bmatrix} = \frac{1}{(2\pi)^2} \int_{-\infty}^{\infty}\int_{-\infty}^{\infty} \begin{bmatrix} \tilde{\underline{\underline{\mathcal{G}}}}(\mathbf{k}_\rho, z, z') \\ \tilde{G}(\mathbf{k}_\rho, z, z') \end{bmatrix} e^{-j\mathbf{k}_\rho\cdot(\rho-\rho')} dk_x dk_y\,. \quad (3.5)$$

The spectral MP-LMGF components are also expressed using transmission line voltage and current similar to TD-LMGF in Chapter 2. For that associated with electric current, we have magnetic vector potential dyadic Green's function as

$$\tilde{\underline{\underline{\mathcal{G}}}}^A(\mathbf{k}_\rho, z, z') = \begin{bmatrix} \frac{1}{j\omega\mu_0} V_i^h & 0 & 0 \\ 0 & \frac{1}{j\omega\mu_0} V_i^h & 0 \\ \frac{\mu_t k_x}{jk_\rho^2}\left(I_i^h - I_i^e\right) & \frac{\mu_t k_y}{jk_\rho^2}\left(I_i^h - I_i^e\right) & \frac{\mu_t}{j\omega\varepsilon_0\varepsilon_z'} I_v^e \end{bmatrix}, \quad (3.6)$$

the scalar potential kernel and vertical current correction term as

$$\tilde{K}^{\Phi}(\mathbf{k}_\rho, z, z') = j\omega\varepsilon_0 \frac{V_i^e - V_i^h}{k_\rho^2}, \qquad \tilde{P}_z(\mathbf{k}_\rho, z, z') = k_0^2 {\mu'}_t \frac{V_v^h - V_v^e}{k_\rho^2} \quad (3.7)$$

The curl of magnetic vector potential dyadic Green's function is

$$\tilde{\nabla}\times\underline{\underline{\tilde{\mathcal{G}}}}^{A}\left(\mathbf{k}_t,z,z'\right) = \begin{bmatrix} -\frac{k_xk_y}{k_\rho^2}\left(I_i^h-I_i^e\right) & -\frac{k_y^2}{k_\rho^2}\left(I_i^h-I_i^e\right)+I_i^h & -\frac{k_y}{\omega\varepsilon_0\varepsilon_z'}I_v^e \\ \frac{k_x^2}{k_\rho^2}\left(I_i^h-I_i^e\right)-I_i^h & \frac{k_xk_y}{k_\rho^2}\left(I_i^h-I_i^e\right) & \frac{k_x}{\omega\varepsilon_0\varepsilon_z'}I_v^e \\ \frac{k_y}{\omega\mu_0\mu_z}V_i^h & -\frac{k_x}{\omega\mu_0\mu_z}V_i^h & 0 \end{bmatrix}. \quad (3.8)$$

The spectral MP-LMGFs associated with magnetic current can be derived by imposing duality principal.

3.1.1 Indepedent Hankel Transform

With rigorous derivation, 14 integrals are found to be independent and are introduced here for simplification of notation and calculation, which are

$$I_1 = S_0\left\{V_i^h\right\}, \quad I_2 = S_0\left\{I_v^e\right\}, \quad (3.9)$$

$$I_3 = S_0\left\{I_i^h+I_i^e\right\}, \quad I_4 = S_0\left\{V_v^e+V_v^h\right\}, \quad (3.10)$$

$$I_5 = S_0\left\{\frac{V_i^h-V_i^e}{k_\rho^2}\right\}, \quad I_6 = S_0\left\{\frac{V_v^h-V_v^e}{k_\rho^2}\right\}, \quad (3.11)$$

$$I_7 = S_0\left\{\frac{I_v^e-I_v^h}{k_\rho^2}\right\}, \quad I_8 = S_0\left\{\frac{I_i^e-I_i^h}{k_\rho^2}\right\}, \quad (3.12)$$

$$I_7 = S_1\left\{\frac{I_i^e-I_i^h}{k_\rho}\right\}, \quad I_8 = S_1\left\{\frac{V_v^h-V_v^e}{k_\rho}\right\}, \quad (3.13)$$

$$I_{11} = S_1\left\{k_\rho V_i^h\right\}, \quad I_{12} = S_1\left\{k_\rho I_v^e\right\}, \quad (3.14)$$

$$I_{13} = S_2\left\{I_i^e-I_i^h\right\}, \quad I_{14} = S_2\left\{V_v^h-V_v^e\right\}. \quad (3.15)$$

Among these 14 integrals, 8 of them are associated with zero-order Bessel function, 4 of them are associated with first-order Bessel function and the rest two of them are associated with second-order Bessel function. Even though the second-order Bessel function can be further expressed as linear combination of zero-order and first-order Bessel functions, we still end up with 14 independent integrals in total after replacement. In this work we just use the above notations.

After substitution of the above integrals to the previous derived MP-LMGFs, we have the spatial form in the following

$$\underline{\underline{\mathcal{G}}}^{A}(\mathbf{r},\mathbf{r}') = \begin{bmatrix} \frac{1}{j\omega\mu_0} I_1 & 0 & 0 \\ 0 & \frac{1}{j\omega\mu_0} I_1 & 0 \\ \mu_t \cos\gamma I_9 & \mu_t \sin\gamma I_9 & \frac{\mu_t}{j\omega\varepsilon_0 \varepsilon'_z} I_2 \end{bmatrix}, \tag{3.16}$$

$$K^{\Phi} = -j\omega\varepsilon_0 I_5, \qquad P_z = k_0^2 \mu'_t I_6, \tag{3.17}$$

and

$$\nabla \times \underline{\underline{\mathcal{G}}}^{A}(\mathbf{r},\mathbf{r}') = \begin{bmatrix} -\frac{1}{2}\sin 2\gamma I_{13} & \frac{1}{2}\left(I_3 + \cos 2\gamma I_{13}\right) & -\frac{1}{j\omega\varepsilon_0\varepsilon'_z}\sin\gamma I_{12} \\ \frac{1}{2}\left(-I_3 + \cos 2\gamma I_{13}\right) & \frac{1}{2}\sin 2\gamma I_{13} & \frac{1}{j\omega\varepsilon_0\varepsilon'_z}\cos\gamma I_{12} \\ \frac{\sin\gamma}{j\omega\mu_0\mu_z} I_{11} & -\frac{\cos\gamma}{j\omega\mu_0\mu_z} I_{11} & 0 \end{bmatrix}. \tag{3.18}$$

The same exercise may be repeated to obtain the MP-LMGFs associated with magnetic current.

3.2 Sommerfeld Integrals Acceleration

3.2.1 Asymptotic Analysis

The asymptotic analysis here is the same as that introduced in chapter 2 for TD-LMGFs, the only difference is that the closed-form identities may be a little different due to the weak singularity of MP-LMGFs, such as the rise of half-line source potential.

3.2.2 Half-Line Source Potential

After rigorous derivation, two extra Sommerfeld related identities apart from the closed-form identities introduced in chapter 2, may be needed for the acceleration of the generalized SIs appearing in MP-LMGFs. The first identity is the spectral Green's function having a second order of decaying respect to k_z^{α} and its right hand

side can be interpreted as the potential caused by a half-line source [40].

$$I_M = S_0 \left\{ \frac{e^{-jk_z^\alpha |\varsigma|}}{2(jk_z^\alpha)^2} \right\} = \frac{1}{\nu^\alpha} \int_{|\varsigma|}^{\infty} \frac{e^{-jk_t R^\alpha}}{4\pi R^\alpha} ds, \tag{3.19}$$

with

$$R^\alpha = \sqrt{\rho^2/\nu^\alpha + s^2}. \tag{3.20}$$

If we define

$$G_z^\alpha(\rho, |\varsigma|) \equiv \int_{|\varsigma|}^{\infty} \frac{e^{-jk_t R^\alpha}}{4\pi R^\alpha} ds, \tag{3.21}$$

the identity M can be further simplified for notation as

$$I_M = S_0 \left\{ \frac{e^{-jk_z^\alpha |\varsigma|}}{2(jk_z^\alpha)^2} \right\} = \frac{1}{\nu^p} G_z^\alpha(\rho, |\varsigma|). \tag{3.22}$$

The second identity that might be useful is

$$I_N = S_0 \left\{ \frac{e^{-jk_z^\alpha |\varsigma|}}{2(jk_z^\alpha)^3} \right\} = -\frac{1}{\nu^\alpha} \left[j \frac{e^{-jk_t R^\alpha}}{4\pi k_t} + |\varsigma| G_z^\alpha(\rho, |\varsigma|) \right]. \tag{3.23}$$

This corresponding to a higher-order of decaying of the integrand respect to k_z^α compared to identity M. As we know, the half-line source potential is firstly introduced in the reference [40] for homogeneous lossless isotropic medium. We can easily expand it to lossy uniaxial anisotropic medium here.

3.2.2.1 Method 1: Exponential Integral Representation

Since we have $R^\alpha = \sqrt{\rho^2/\nu^\alpha + s^2}$ and $R^\alpha dR^\alpha = sds$, Eq. (3.21) can be written as

$$\int_z^{\infty} \frac{e^{-jk_t R^\alpha}}{4\pi R^\alpha} ds = \int_{r^\alpha}^{\infty} \frac{e^{-jk_t R^\alpha}}{4\pi \sqrt{R^\alpha - \rho^2/\nu^\alpha}} dR^\alpha = \int_{r^\alpha}^{\infty} \frac{e^{-jk_t R^\alpha}}{4\pi R^\alpha} \left[\sum_{n=0}^{\infty} C_n \left(\frac{\rho/\sqrt{\nu^\alpha}}{R^\alpha} \right)^{2n} \right] dR^\alpha. \tag{3.24}$$

where the lower limit is $r^\alpha = \sqrt{\rho^2/\nu^\alpha + z^2}$ and the coefficients C_n are binomial expansion coefficients. The above expansion is only valid inside the unit circle in the complex γ plane

$$|\gamma| = \left| \frac{\rho/\sqrt{\nu^\alpha}}{R^\alpha} \right| \leq 1, \tag{3.25}$$

implying the convergence condition

$$\left| \rho/\sqrt{\nu^\alpha} \right| \leq |R^\alpha|. \tag{3.26}$$

since $\angle \nu^\alpha \in (-\pi/2, \pi/2)$, we can derive $\angle 1/\sqrt{\nu^\alpha} \in (-\pi/4, \pi/4)$. The above condition Eq. (3.26) always hold true from Figure 3.1.

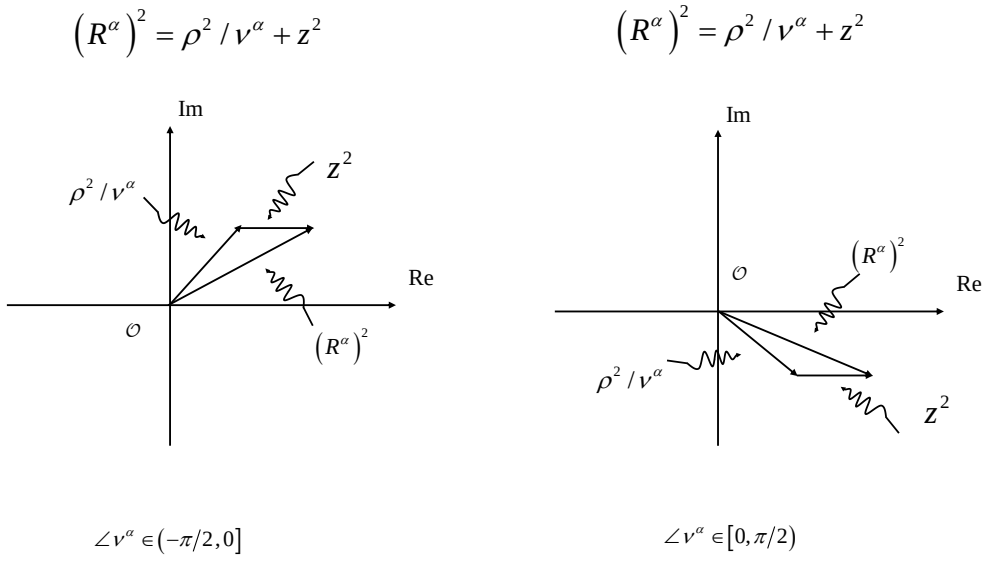

Figure 3.1. Graphical proof of binomial expansion convergence condition.

After the convergence check, we now can switch the order of integration and summation, yielding

$$G_z^\alpha = \sum_{n=0}^{\infty} C_n \left(\rho/\sqrt{\nu^\alpha}\right)^{2n} \frac{1}{4\pi} \int_{r^\alpha}^{\infty} \frac{e^{-jk_t R^\alpha}}{(R^\alpha)^{2n+1}} dR^\alpha. \tag{3.27}$$

If we denote $t = R^\alpha / r^\alpha, dR^\alpha = r^\alpha dt$, we have

$$G_z^\alpha = \frac{1}{4\pi} \sum_{n=0}^{\infty} C_n \left(\frac{\rho / \sqrt{\nu^p}}{r} \right)^{2n} E_{2n+1} \left(j k_t r \right), \tag{3.28}$$

where the complex exponential integrals are

$$E_n \left(z \right) = \int_1^\infty t^{-n} e^{-zt} r dt. \tag{3.29}$$

The recurrence relation for the exponential integrals

$$E_{n+1} \left(z \right) = \frac{1}{n} \left(e^{-z} - z E_{n+1} \left(z \right) \right), \quad n = 1, 2, 3, \ldots, \tag{3.30}$$

can be further used to simplify the calculation. For the limiting case $\rho = 0$, the only term appearing in Eq. (3.28) is the $n = 0$ term, and therefore,

$$G_z^\alpha \left(\rho = 0, z \right) = \frac{1}{4\pi} E_1 \left(j k_t z \right). \tag{3.31}$$

The method employs the binomial series expansion to evaluate the half-line source potential, thus its convergence rate depends on the convergence rate of the series expansion. As we learned before, the convergence radius of binomial expansion is $|\gamma| < 1$ and the smaller $|\gamma| = \left| \frac{\rho / \sqrt{\nu^\alpha}}{R^\alpha} \right|$ is, the faster the convergence we can achieve. This corresponds to the small observation angle θ physically in the spatial domain. However, for large observation angles θ, an alternative approach is desired.

3.2.2.2 Method 2: Numerical Integral

The second method is a pure numerical approach. We may write

$$G_z^\alpha \left(\rho, z \right) = \int_0^\infty \frac{e^{-j k_t R^\alpha}}{4\pi R^\alpha} ds - \int_0^z \frac{e^{-j k_t R^\alpha}}{4\pi R^\alpha} ds. \tag{3.32}$$

The first term on the right hand side is the half of the potential contribution from an infinite line source and is readily written in terms of zero-order Hankel function of the second kind corresponding to an outgoing wave [61],

$$\int_0^\infty \frac{e^{-jk_t R^\alpha}}{4\pi R^\alpha} ds = \frac{1}{8j} H_0^2 \left(k_t \frac{\rho}{\sqrt{\nu^\alpha}} \right). \tag{3.33}$$

Here we need to be careful about the branch cut of the Hankel function as the variable k_t extends into the complex domain. Since $\angle k_t / \sqrt{\nu^\alpha} \in (-\pi/2, 0]$, the above identity follows an analytic continuation extending off the real axis into the complex plane from isotropic medium to complex uniaxial anisotropic medium.

The remaining integral corresponds physically to a potential produced by a small segment of line source extending from $s = 0$ to $s = z$:

$$\Delta G_z^\alpha = \int_0^z \frac{e^{-jk_t R^\alpha}}{4\pi R^\alpha} ds. \tag{3.34}$$

The above integrand is a near-singular integrand and by introducing a transformation of integration variable

$$du = \frac{1}{R^\alpha} ds, \tag{3.35}$$

corresponding to the function

$$u = \sinh^{-1} \left(z\sqrt{\nu^\alpha}/\rho \right), \tag{3.36}$$

we can remove its near-singular behavior. Thus the integral in Eq. (3.34) becomes

$$\Delta G_z^\alpha = \frac{1}{4\pi} \int_0^{\sinh^{-1}\left(z\sqrt{\nu^\alpha}/\rho\right)} e^{-jk_t R^\alpha} du. \tag{3.37}$$

Again, the $\sinh^{-1}$ function is extended into complex plane and its branch cut should be careful treated. Because $\sinh^{-1}$ function contains a logarithm function, it has an infinite Riemann sheets and the right Riemann sheet should be chosen to get the correct result. Fortunately $\angle\sqrt{\nu^\alpha} \in (-\pi/4, \pi/4)$ is on the principal branch for most programming languages, when determining the upper bound of the integral by analytic continuation, no special treatment is required.

After the transformation, the integration path is mapped to a complex curve on the complex u plane. However, the integrand itself becomes an analytic function such that path deformation is allowed. A simple and natural choice is a straight line connecting the points from the lower to the upper limit.

3.3 Numerical Examples

As a first example, we repeat the same exercise for the second example in Chapter 2. Here we compare the integrand behaviors of I_1 and I_5 with and without asymptotic subtraction in Figure 3.2.

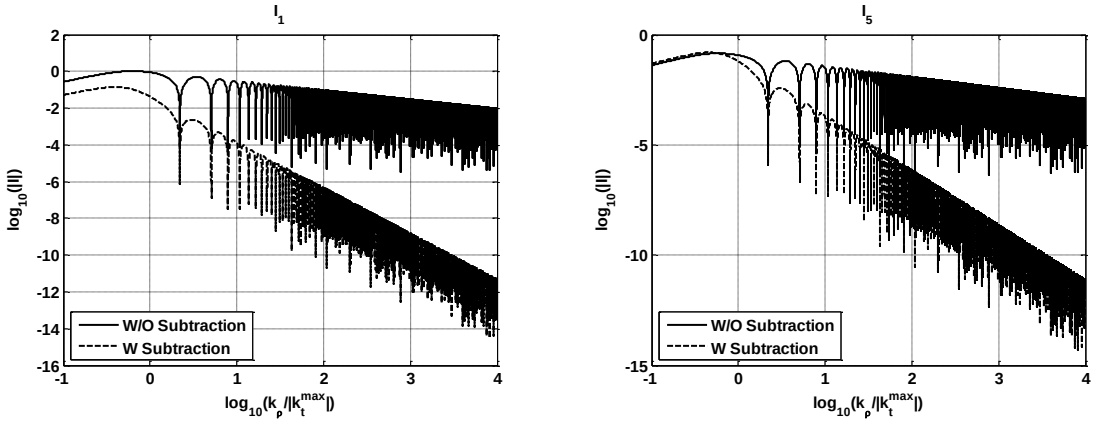

Figure 3.2. Comparison of the integrand spectrum for I_1 and I_5 with and without singularity extraction.

After that, we redo the same procedure for the third example in Chapter 2. The integrals are observed on three different observation lines and the results are

compared between with and without singularity extraction in Figure 3.3, Figure 3.4 and Figure 3.5. Good agreements are achieved on these three cases.

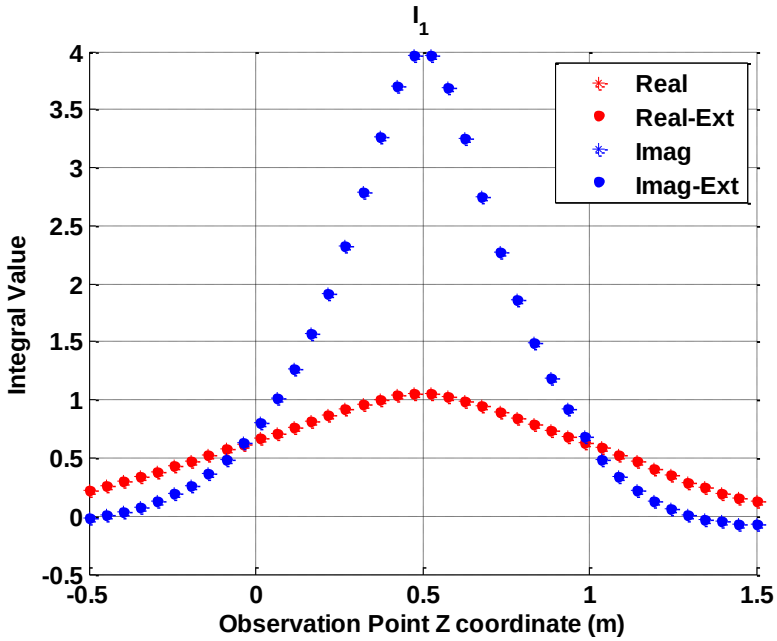

Figure 3.3. The integral I_1 for MP-LMGF on observation line $\rho > 0$, $\varsigma > 0$.

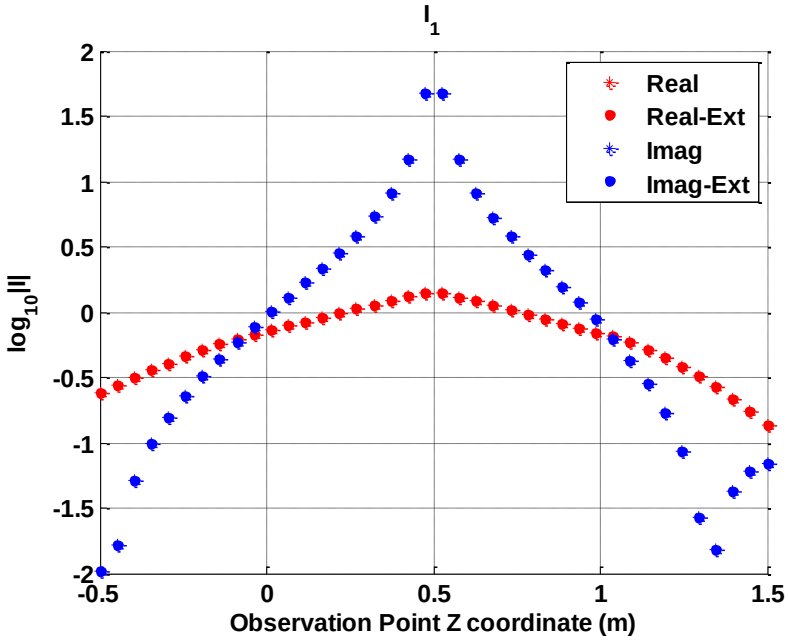

Figure 3.4. The integral I_1 for MP-LMGF on observation line $\rho = 0$, $\varsigma > 0$.

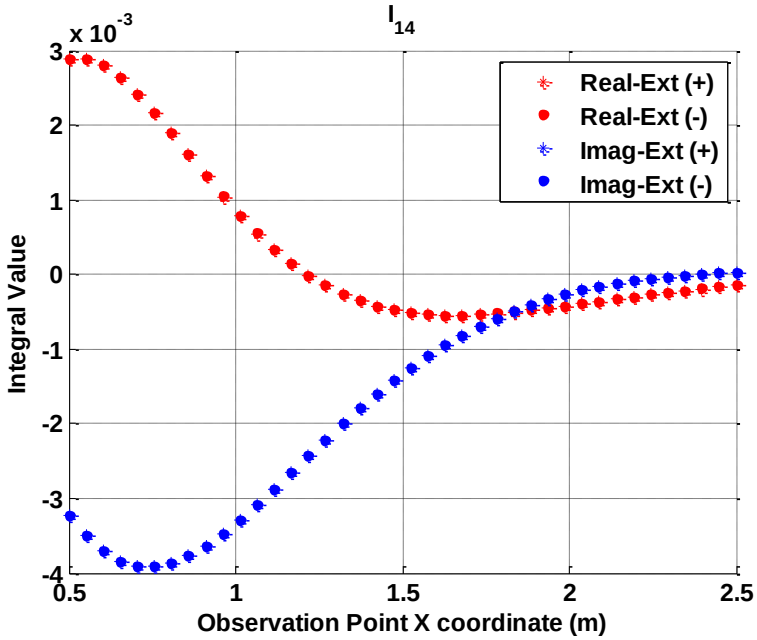

Figure 3.5. The integral I_{14} for MP-LMGF on observation line $\rho > 0$, $\varsigma = 0$. The plus "+" and minus "-" sign indicates approach to the observation line from above and below.

Chapter 4

Integral Equation Method

When we solve electromagnetic scattering problems in layered medium, full wave simulations may be performed. In general, there are three major methods for full-wave simulation, the finite-difference method [62], finite element method [63] and method of moments [64, 65]. The finite difference method and finite element method require one to discretize the entire interested region and to solve the electromagnetic field everywhere in space. Hence, the resulting number of unknowns is usually quite large. Sometimes if the scatterers have some fine structures, a single mesh scheme for the whole structure may lead to a large number of wasted unknowns. Furthermore, in order to truncate the infinite domain to a finite domain, a perfectly matched layer (PML) should be used to absorb the outgoing wave in order to impose the Sommerfeld radiation condition [66–68]. The discretization of the interested region will also introduce grid dispersion when the field is propagated from one point to another[69]. The grid dispersion causes inaccurate wave velocities in different directions and results in cumulative errors that become intolerable [70]. However, when we apply integral equation methods, the Green's function propagates the field from one point to another in a exact manner and no dispersion error is introduced. The integral equation approach with Green's function becomes particularly powerful in a complex medium, for example, considering scatterers near, penetrating or embedded in a stratified layered media. The LMGF takes into account multi-reflection and the interference of different spectra of waves in the layered medium. Using the surface integral equation method, the unknowns are only associated with the surface of the objects or scatterers instead of everywhere in the space of interest. Also, the formulation of integral equations follows from the strong physics of waves and field interactions. Instead of

performing pure numerical calculation as in finite difference or finite element method, the integral equation based method brings physical insight to the problems under investigation and allows one to distinguish the primary field and induced field easily. The main difficulties of the integral equation are (1) the singular integrals in the element matrix are difficult to calculate [71–73], and (2) the resulting dense system matrix requires $O(N^2)$ storage and more than $O(N^2)$ effort to solve. Fortunately, many advanced numerical methods are developed to handle all kinds of singular kernels and with the development of some fast integral solvers [74–80], the second limitation is much relieved. The discussion of these topics is beyond the scope of this dissertation and will be not discussed here. In this chapter, we will focus on the integral equation formulation.

4.1 Equivalence Principle

Let us consider an arbitrary shaped object embedded inside a layered medium. We denote the surface of the object as S, and the region outside and inside the object are V^+ and V^-, respectively. Let $(\mathbf{J}_i^+, \mathbf{M}_i^+)$ be the impressed electric and magnetic currents outside the scatter, and $(\mathbf{J}_i^-, \mathbf{M}_i^-)$ be the impressed source quantities inside. The fields due to the excitation of these current sources are denoted as $(\mathbf{E}^+, \mathbf{H}^+)$ outside and $(\mathbf{E}^-, \mathbf{H}^-)$ inside, respectively. In the background stratified medium, each layer is assumed to be a complex uniaxial anisotropic medium. The configuration is illustrated in Figure 4.1.

A) Exterior Equivalence

If we place equivalent surface currents

$$\mathbf{J}_s^+ = \hat{\mathbf{n}}^+ \times \mathbf{H}^+, \quad \mathbf{M}_s^+ = -\hat{\mathbf{n}}^+ \times \mathbf{E}^+, \tag{4.1}$$

on S, these equivalent currents $(\mathbf{J}_s^+, \mathbf{M}_s^+)$ plus the original impressed sources $(\mathbf{J}_i^+, \mathbf{M}_i^+)$ outside together produce the original fields $(\mathbf{E}^+, \mathbf{H}^+)$ outside and a null field $(\mathbf{0}^-, \mathbf{0}^-)$

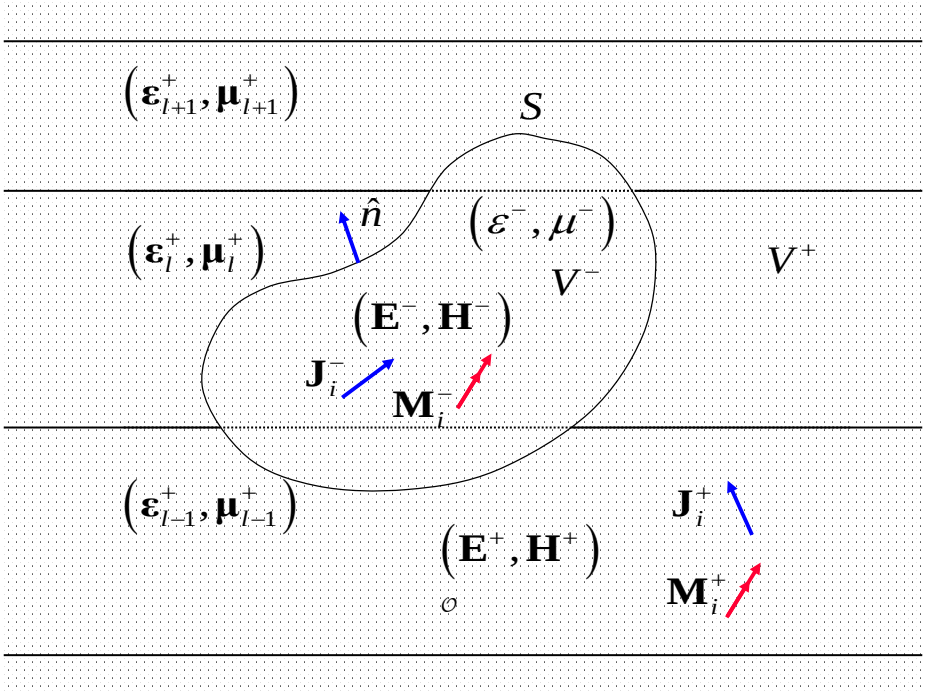

Figure 4.1. Scattering problems in lossy uniaxial anisotropic multi-layered medium.

inside[81].

B) Interior Equivalence

Similarly, if we place an equivalent surface currents

$$\mathbf{J}_s^{-} = \hat{\mathbf{n}}^{-} \times \mathbf{H}^{-}, \quad \mathbf{M}_s^{-} = -\hat{\mathbf{n}}^{-} \times \mathbf{E}^{-}, \tag{4.2}$$

on S, these equivalent currents $(\mathbf{J}_s^{-}, \mathbf{M}_s^{-})$ plus the original impressed sources $(\mathbf{J}_i^{-}, \mathbf{M}_i^{-})$ inside together produce the original fields $(\mathbf{E}^{-}, \mathbf{H}^{-})$ inside and a null field $(\mathbf{0}^{+}, \mathbf{0}^{+})$ outside.

Because the physical fields inside and outside the surface S are continuous, the introduced equivalent surface currents of the exterior and interior equivalences are just the negative of one other, satisfying

$$\mathbf{J}_s^{+} = -\mathbf{J}_s^{-}, \quad \mathbf{M}_s^{+} = -\mathbf{M}_s^{-}. \tag{4.3}$$

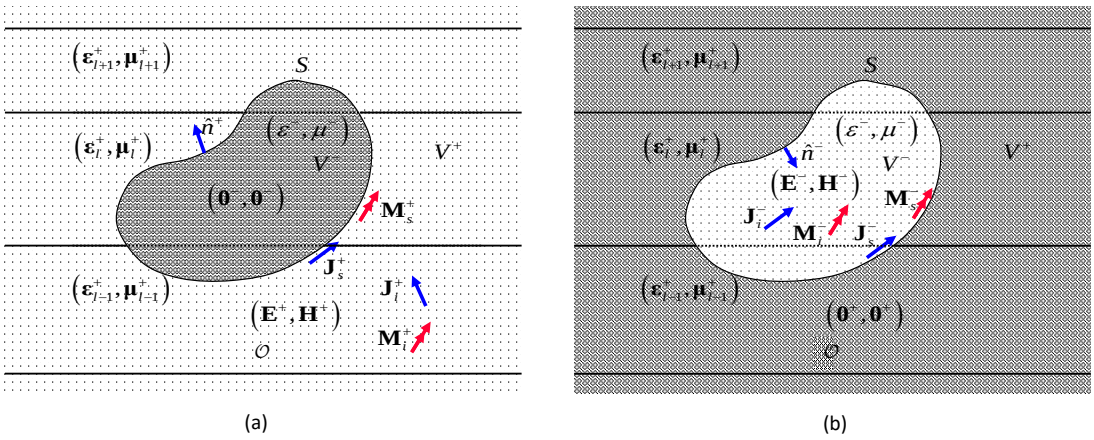

Figure 4.2. Equivalent currents for (left) exterior region and (right) interior region.

If we enforce the continuity condition of the physical electric and magnetic field along the surface S, we end up with the following two equations :

$$\begin{cases} \lim\limits_{r \downarrow S} \mathbf{E}\left(\mathbf{J}_s^+, \mathbf{M}_s^+\right) + \mathbf{E}\left(\mathbf{J}_i^+, \mathbf{M}_i^+\right) = \lim\limits_{r \uparrow S} \mathbf{E}\left(\mathbf{J}_s^-, \mathbf{M}_s^-\right) + \mathbf{E}\left(\mathbf{J}_i^-, \mathbf{M}_i^-\right) \\ \lim\limits_{r \downarrow S} \mathbf{H}\left(\mathbf{J}_s^+, \mathbf{M}_s^+\right) + \mathbf{H}\left(\mathbf{J}_i^+, \mathbf{M}_i^+\right) = \lim\limits_{r \uparrow S} \mathbf{H}\left(\mathbf{J}_s^-, \mathbf{M}_s^-\right) + \mathbf{H}\left(\mathbf{J}_i^-, \mathbf{M}_i^-\right) \end{cases}, \tag{4.4}$$

where the up arrow $\uparrow$ and down arrow $\downarrow$ denote S is approached from the interior or exterior respectively. Together with equations Eq. (4.3), we can solve the unknown equivalent currents. This formulation is often referred as the famous PMCHWT (Poggio, Miller, Chang, Harrington, Wu, Tsai) [82] formulation for scattering problems of homogeneous dielectric bodies.

If the above object is a perfect electric conductor (PEC) with no interior sources, the only unknown current type is the electric current because

$$\mathbf{M}_s^+ = -\hat{\mathbf{n}}^+ \times \mathbf{E}^+ = \mathbf{0}. \tag{4.5}$$

Enforcing the boundary condition of electric current or magnetic fields, Eq. (4.4)

reduces to

$$\lim_{\underline{r}\uparrow S} \mathbf{E}\left(\mathbf{J}_s^+, \mathbf{0}_s^+\right) + \mathbf{E}\left(\mathbf{J}_i^+, \mathbf{M}_i^+\right) = \mathbf{0}, \quad \text{or} \quad \lim_{\underline{r}\downarrow S} \mathbf{E}\left(\mathbf{J}_s^+, \mathbf{0}_s^+\right) + \mathbf{E}\left(\mathbf{J}_i^+, \mathbf{M}_i^+\right) = \mathbf{0}, \quad (4.6)$$

and

$$\lim_{\underline{r}\uparrow S} \mathbf{H}\left(\mathbf{J}_s^+, \mathbf{0}_s^+\right) + \mathbf{H}\left(\mathbf{J}_i^+, \mathbf{M}_i^+\right) = \mathbf{0}, \quad \text{or} \quad \lim_{\underline{r}\downarrow S} \mathbf{H}\left(\mathbf{J}_s^+, \mathbf{0}_s^+\right) + \mathbf{H}\left(\mathbf{J}_i^+, \mathbf{M}_i^+\right) = \mathbf{H}^+. \quad (4.7)$$

One thing that should be pointed out is that the two different forms of the equation from the internal surface and the external surface above are equivalent. The jump discontinuity of the magnetic field in Eq. (4.7) comes from the electric source current. Eq. (4.6) and Eq. (4.7) are called Electric Field Integral Equation (EFIE) and Magnetic Field Integral Equation (MFIE), respectively. The above MFIE Eq. (4.7) often results in a poorly-tested scheme [83], Alternatively, the rotated version of Eq. (4.7) shown in Eq. (4.8) is more popular:

$$\hat{\mathbf{n}}^+ \times \lim_{\underline{r}\downarrow S} \mathbf{H}\left(\mathbf{J}_s^+, \mathbf{0}_s^+\right) + \hat{\mathbf{n}}^+ \times \mathbf{H}\left(\mathbf{J}_i^+, \mathbf{M}_i^+\right) = \hat{\mathbf{n}}^+ \times \mathbf{H}^+. \quad (4.8)$$

Sometimes, a linear combination of Eqs. Equation 4.6 and Equation 4.8 is used to remove the internal resonance of a numerical solution. Their physical meaning is discussed in [65], [70].

4.2 Discretization Scheme

In order to solve the scattering problems using a computer, we need to transform the above equations into matrix form using the subspace projection method. We shall use the div-conforming RWG basis function [84] to expand the unknown currents and

test Eq. (4.4) in a Galerkin sense. The resulting matrix equations are

$$\begin{bmatrix} Z_{mn}^{+} + Z_{mn}^{-} & -\alpha_{mn}^{+} - \alpha_{mn}^{-} \\ \beta_{mn}^{+} + \beta_{mn}^{-} & Y_{mn}^{+} + Y_{mn}^{-} \end{bmatrix} \begin{bmatrix} I_n \\ V_n \end{bmatrix} = \begin{bmatrix} V_m^i \\ I_m^i \end{bmatrix}, \tag{4.9}$$

where the impedance matrix is

$$\begin{aligned} [Z_{mn}] = j\omega\mu_0 < \mathbf{\Lambda}_m; \underline{\underline{\mathcal{G}}}^A; \mathbf{\Lambda}_n > & + \frac{1}{j\omega\varepsilon_0} < \nabla \cdot \mathbf{\Lambda}_m; K^{\Phi}, \nabla \cdot \mathbf{\Lambda}_n > \\ & + \frac{1}{j\omega\varepsilon_0} < \nabla \cdot \mathbf{\Lambda}_m, P_z, \mathbf{\Lambda}_n \cdot \hat{\mathbf{z}} >, \end{aligned} \tag{4.10}$$

and the admittance matrix is

$$\begin{aligned} [Y_{mn}] = j\omega\varepsilon_0 < \mathbf{\Lambda}_m; \underline{\underline{\mathcal{G}}}^F; \mathbf{\Lambda}_n > & + \frac{1}{j\omega\mu_0} < \nabla \cdot \mathbf{\Lambda}_m; K^{\Psi}, \nabla \cdot \mathbf{\Lambda}_n > \\ & + \frac{1}{j\omega\mu_0} < \nabla \cdot \mathbf{\Lambda}_m; Q_z, \mathbf{\Lambda}_n \cdot \hat{\mathbf{z}} > . \end{aligned} \tag{4.11}$$

The α matrix and β matrix are

$$[\alpha_{mn}] = - < \mathbf{\Lambda}_m; \nabla \times \underline{\underline{\mathcal{G}}}^F; \mathbf{\Lambda}_n >; \quad [\beta_{mn}] = - < \mathbf{\Lambda}_m; \nabla \times \underline{\underline{\mathcal{G}}}^A; \mathbf{\Lambda}_n > . \tag{4.12}$$

The right hand side (RHS) system vectors are

$$\left[V_m^i\right] = < \mathbf{\Lambda}_m; \mathbf{E}_i^+ - \mathbf{E}_i^- >; \left[I_m^i\right] = < \mathbf{\Lambda}_m; \mathbf{H}_i^+ - \mathbf{H}_i^- > . \tag{4.13}$$

For the background layered medium, the Green's function kernels are those appearing in Chapter 3, while for the inner homogeneous medium, the dyadic Green's function kernels can be expressed as

$$\underline{\underline{\mathcal{G}}}^A = \underline{\underline{\mathcal{G}}}^F = G\underline{\underline{\mathcal{I}}}, \tag{4.14}$$

and the scalar potential kernels can be written as

$$K^{\Phi} = K^{\Psi} = G, \qquad P_z = Q_z = 0. \tag{4.15}$$

with $G = e^{-jkR}/4\pi R$.

Similarly, the discretization of the EFIE in Eq. (4.6) results in the matrix equation below

$$[Z_{mn}]\,[I_n] = \left[V_m^i\right], \tag{4.16}$$

with $[Z_{mn}]$ being the same as Eq. (4.10) and the system vector $[V_m^i]$ being

$$\left[V_m^i\right] = < \mathbf{\Lambda}_m; \mathbf{E}_i^+ > . \tag{4.17}$$

The discretization of the MFIE in Eq. (4.8) results in the matrix equation below:

$$[\beta_{mn}]\,[I_n] = \left[I_m^i\right], \tag{4.18}$$

with $[\beta_{mn}]$ being

$$[\beta_{mn}] = \frac{1}{2} < \mathbf{\Lambda}_m; \mathbf{\Lambda}_n > - < \mathbf{\Lambda}_m; \hat{\mathbf{n}} \times \nabla \times \underline{\underline{\mathcal{G}}}^A; \mathbf{\Lambda}_n > \tag{4.19}$$

and the system vector $[I_m^i]$ being

$$\left[I_m^i\right] = < \mathbf{\Lambda}_m; \hat{\mathbf{n}} \times \mathbf{H}_i^+ > . \tag{4.20}$$

The discretization of the CFIE [85] can be expressed as

$$\left[\frac{1}{\eta_0} Z_{mn} + \alpha \beta_{mn}\right][I_n] = \left[\frac{1}{\eta_0} V_m^i + \alpha I_m^i\right], \alpha \in (0, 1]\,. \tag{4.21}$$

4.3 Solution of Matrix Equation

The matrix equation can be solved using two types of methods: direct methods and iterative methods. Commonly used direct solvers include Gaussian elimination, the LU decomposition, and frontal and multifrontal methods. The main advantage of the direct solvers is that it can produce an accurate solution in a fixed computational cost, hence is very efficient for small problems. The computational complexity of the direct solver is $O(N^3)$, and with the number of unknowns increases, the computational time increases dramatically. Alternative, matrix with a large number of unknowns usually employ iterative solvers to obtain the solution, since the complexity is on the order of $O(N^2)$. Commonly used iterative solvers include the conjugate gradient method(CG), biconjugate gradient method (BiCG), biconjugate gradient stabilized (BiCGSTAB) and generalized minial residual (GMRES), etc. Among various iterative methods, the conjugate gradient iterative method (CG), and their extensions received increasing interests. For ill-conditioned matrix, the number of iterations can be greatly reduced using preconditioning techniques, such as diagonal, block diagonal, near-neighbor and Calderón preconditioning techniques.

4.4 Numerical Examples

As a first example, a PEC object is embedded inside a three layered medium. It is excited by a electric dipole with polarization of ($\theta = 45°, \phi = 0°$,). The configurations and all the parameters are shown in Figure 4.3. An observation line along ($-4 \leq x \leq 4, y = 0, z = -0.9$) m is chosen to observe the field distribution. Both the EFIE and MFIE are used to calculate the induced current and the field distribution. Results for the x and z components of the electric field are shown in Figure 4.4 and Figure 4.5.

As a second example, we change the object to be homogeneous dielectric with constants $\varepsilon_r = 4$ and $\mu_r = 1$. The second layer is also changed to an isotropic layer

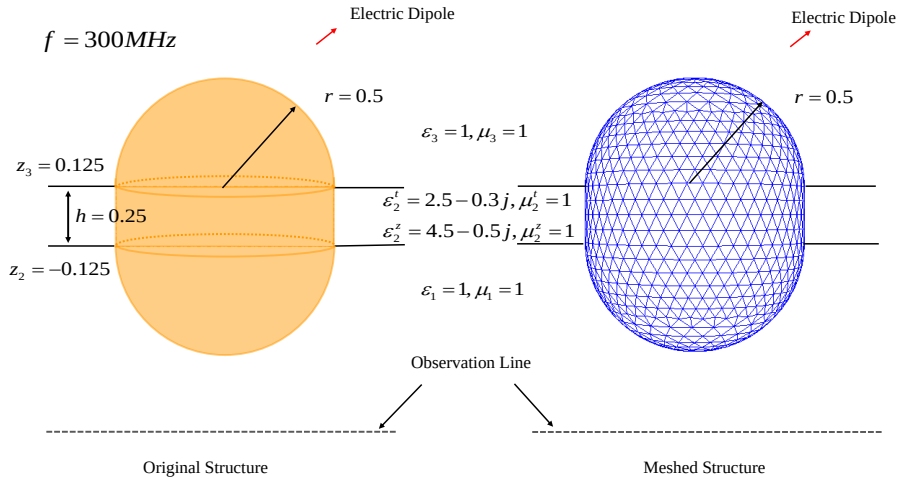

Figure 4.3. A PEC object embedded inside a three-layered medium with (left) original and (right) meshed structure.

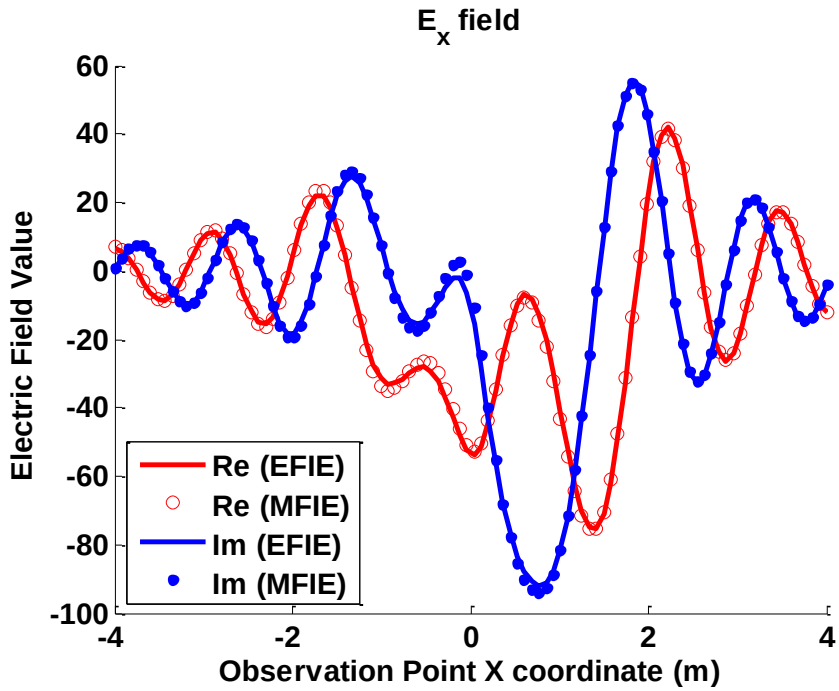

Figure 4.4. The x component of the electric field calculated using EFIE and MFIE formulation.

with $\varepsilon_2 = 2.5 - 0.3j$ and $\mu_2 = 1$ in order to compare with the results from an existing reference [59]. Again for the x and z components of the electric field are shown in Figures 4.6 and 4.7.

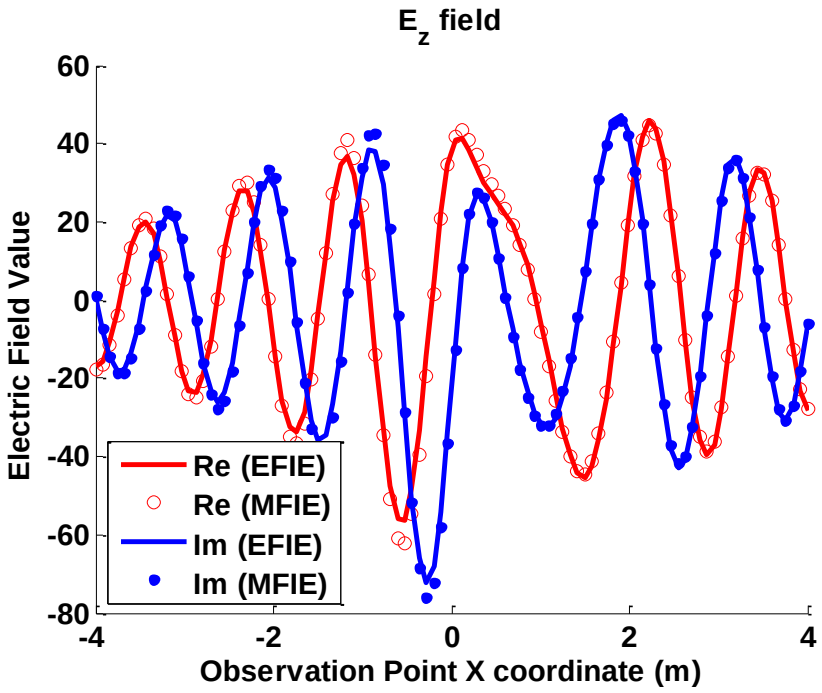

Figure 4.5. The z component of the electric field calculated using EFIE and MFIE formulation.

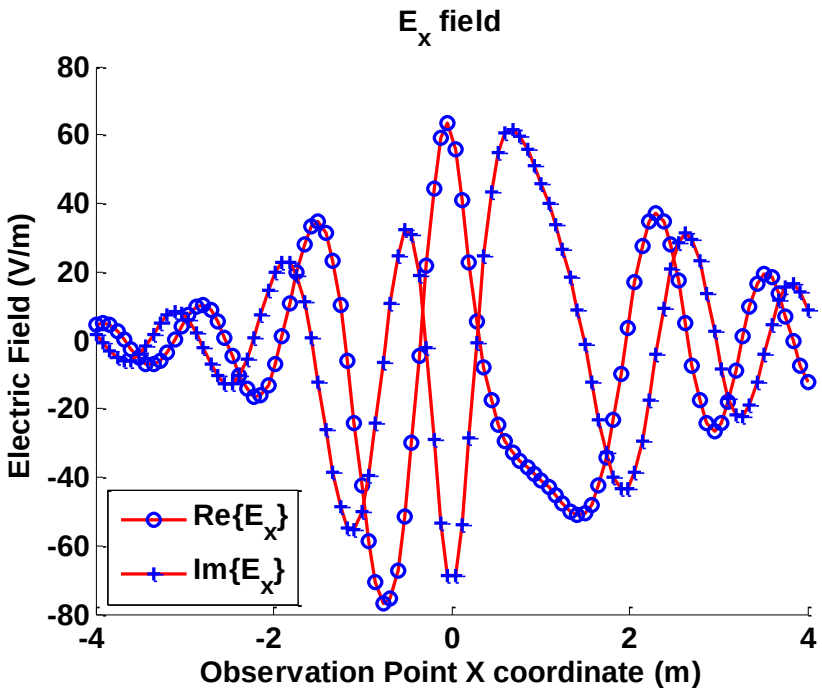

Figure 4.6. The x component of the electric field calculated using PMCHWT formulation.

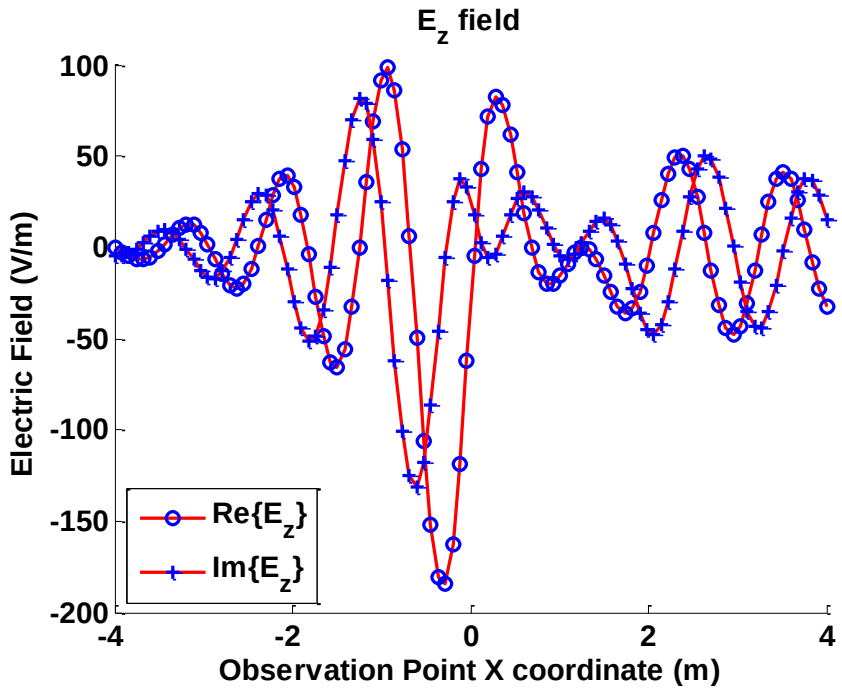

Figure 4.7. The z component of the electric field calculated using PMCHWT formulation.

Chapter 5

Second Level Singularity Extraction

In the previous chapters, we discussed various techniques to accelerate the computation of Sommerfeld integrals and applied them to several scattering problems. Typically, when we employ integral equations to solve scattering problems, hundreds of millions times of LMGF computation is required during the filling of system matrix. In order to further accelerate the matrix filling process, one attractive yet popular remedy is to precompute these integrals on a grid of points in the solution domain. Then the integrals can be computed using table look-up and interpolation techniques. For example, Atkins and Chew [39] proposed a scheme to reduce the storage of five SIs to only two basic SIs and interpolate their values and their derivatives for the computation of LMGF. Francavilla [38] reported a simplex interpolation scheme can further accelerate the matrix filling while maintaining the same accuracy. Depending on different problems, the interpolation can be performed in one dimension(1-D), two dimensions(2-D) and three dimensions(3-D). For arbitrary shaped objects that are embedded in different layers, 3-D interpolation in $\rho - \rho'$, z and z' is required. An example of the sampling of the tabulation grid in three dimensions can be seen in Figure B.2.

5.1 Motivation

In order to increase the interpolation accuracy, the singularity extraction technique introduced before is used to regularize the spectral integral. In general, the spatial curl-type Greens function that appear in the MFIE, PMCHWT and hybrid FEM formulations is more singular than the other mixed-potential LMGFs. Using one-level of singularity subtraction, the remaining spatial integrals still contain a logarithm

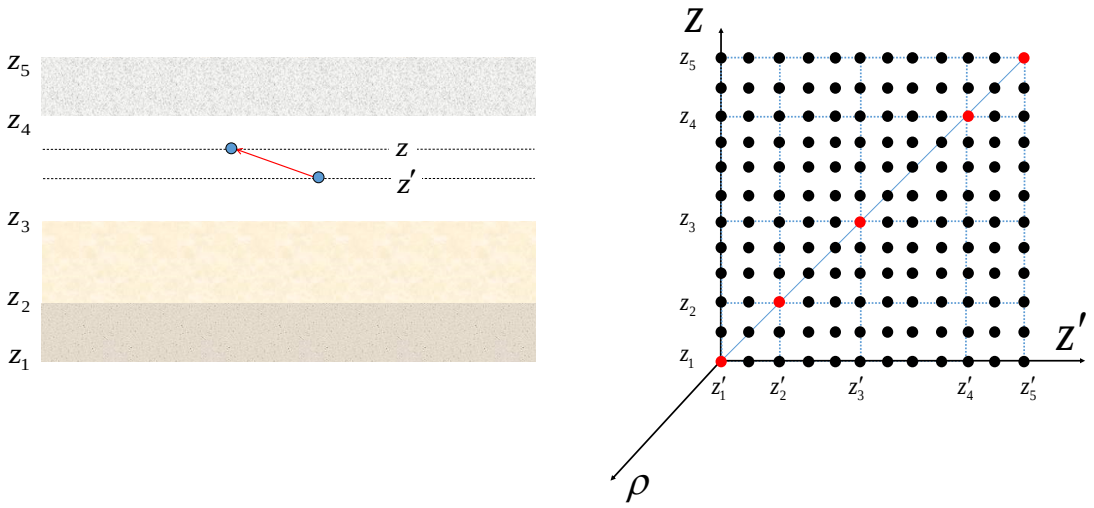

Figure 5.1. Example of a four layered medium and the sampling of three dimensional tabulation grid in $\rho = 0$ plane.

singularity arising from the quasi-static image source, which causes the interpolation scheme to lose accuracy. Thus, a higher-order asymptotic subtraction is needed in order to remove all unbounded behavior.

5.2 Second Level Asymptotic Forms

5.2.1 Second Level Asymptotic Forms of Reflection Coefficient

Consider a two layered medium, the reflection coefficient looking down (left) is (α = TE or TM)

$$\overleftarrow{\Gamma}_{21}^{\alpha} = \frac{Z_1^{\alpha} - Z_2^{\alpha}}{Z_1^{\alpha} + Z_2^{\alpha}}. \tag{5.1}$$

The two-levels of asymptotic forms can be obtained using a Taylor series expansion resulting in the form

$$\overleftarrow{\Gamma}^{\alpha,\infty}(k_\rho) = \overleftarrow{\Gamma}^{\alpha,1,\infty} + \frac{1}{k_\rho^2}\overleftarrow{\Gamma}^{\alpha,2,\infty} + \mathrm{O}\left(k_\rho^{-4}\right), \tag{5.2}$$

where $\Gamma^{\alpha,1,\infty}$ and $\Gamma^{\alpha,2,\infty}$ are denoted as first-level and second-level of asymptotic

reflection coefficient respectively.

A) TM Mode

For the TM mode, the reflection coefficient can be expressed as

$$\overleftarrow{\Gamma}^{e}_{21} = \frac{Z^e_1 - Z^e_2}{Z^e_1 + Z^e_2} = \frac{\left(\frac{k^e_z}{\omega\varepsilon_0\varepsilon_t}\right)_1 - \left(\frac{k^e_z}{\omega\varepsilon_0\varepsilon_t}\right)_2}{\left(\frac{k^e_z}{\omega\varepsilon_0\varepsilon_t}\right)_1 + \left(\frac{k^e_z}{\omega\varepsilon_0\varepsilon_t}\right)_2}. \tag{5.3}$$

Since we have

$$k^\alpha_z = \sqrt{k^2_t - v^\alpha k^2_\rho} = -j\sqrt{v^\alpha}k_\rho\sqrt{1 - \frac{\mu_t\varepsilon_t k^2_0}{v^\alpha k^2_\rho}}, \tag{5.4}$$

if we define $x = \frac{k^2_0}{k^2_\rho}$, and

$$\mathrm{a}^\alpha = \begin{cases} \sqrt{\varepsilon_t\varepsilon_z}, \alpha = e \\ \sqrt{u_t\mu_z}, \alpha = h \end{cases}, \quad b^\alpha = \frac{\mu_t\varepsilon_t}{v^\alpha} = \begin{cases} \mu_t\varepsilon_z, \alpha = e \\ \varepsilon_t\mu_z, \alpha = h \end{cases}, \tag{5.5}$$

by using the binomial series

$$\sqrt{1-t} = 1 - \frac{1}{2}t - \frac{1}{8}t^2 - \cdots, \tag{5.6}$$

we may obtain the expansion of k_z in term of k_ρ as

$$k^\alpha_z \approx -j\sqrt{v^\alpha}k_\rho\left(1 - \frac{1}{2}b^\alpha x\right). \tag{5.7}$$

Substituting the expression Eq. (5.7) to Eq. (5.3), we have

$$\overleftarrow{\Gamma}^{e,\infty}_{21} = \frac{A^e - B^e x}{C^e - D^e x}, \tag{5.8}$$

with the coefficients being

$$\begin{aligned} A^e &= a_2^e - a_1^e, \quad B^e = a_2^e b_1^e/2 - a_1^e b_2^e/2, \\ C^e &= a_2^e + a_1^e, \quad D^e = a_2^e b_1^e/2 + a_1^e b_2^e/2. \end{aligned} \tag{5.9}$$

The reflection coefficient Eq. (5.8) can be further expanded into the formula below:

$$\overleftarrow{\Gamma}_1^{e,\infty} = \frac{A^e - B^e x}{C^e - D^e x} = \frac{A^e - B^e x}{C^e} \frac{1}{1 - D^e/C^e x}. \tag{5.10}$$

Using geometric series formula for $|t| < 1$

$$\frac{1}{1-t} = 1 + t + t^2 + \cdots, \tag{5.11}$$

we obtain the asymptotic reflection coefficient in expression Eq. (5.2) as

$$\overleftarrow{\Gamma}^{e,1,\infty} = \frac{A^e}{C^e}, \overleftarrow{\Gamma}^{e,2,\infty} = \frac{A^e D^e - B^e C^e}{(C^e)^2} k_0^2. \tag{5.12}$$

B) TE Mode

The same exercise is repeated to obtain the second level asymptotic form of the reflection coefficient for TE case. The reflection coefficient for TE case is

$$\overleftarrow{\Gamma}_2^h = \frac{Z_1^h - Z_2^h}{Z_1^h + Z_2^h} = \frac{\left(\frac{\omega\mu_0\mu_t}{k_z^h}\right)_1 - \left(\frac{\omega\mu_0\mu_t}{k_z^h}\right)_2}{\left(\frac{\omega\mu_0\mu_t}{k_z^h}\right)_1 + \left(\frac{\omega\mu_0\mu_t}{k_z^h}\right)_2}, \tag{5.13}$$

and without detailed derivation its corresponding two level asymptotic reflection coefficients are given as

$$\overleftarrow{\Gamma}^{h,1,\infty} = \frac{A^h}{C^h}, \overleftarrow{\Gamma}^{h,2,\infty} = \frac{A^h D^h - B^h C^h}{(C^h)^2} k_0^2, \tag{5.14}$$

with the coefficient constant A, B, C, D being

$$
\begin{aligned}
A^h &= a^h_{l-1} - a^h_l, \quad B^h = a^h_{l-1} b^h_l/2 - a^h_l b^h_{l-1}/2, \\
C^h &= a^h_{l-1} + a^h_l, \quad D^h = a^h_{l-1} b^h_l/2 + a^h_l b^h_{l-1}/2.
\end{aligned} \tag{5.15}
$$

One thing worthy to mention is the above expansion can be performed in terms of k_z. Due to the different forms of independent Hankel transforms introduced in Chapter 3 and the available closed-form Sommerfeld and related identities, both expansion forms in k_ρ and k_z are useful. However, one needs to be careful that k_ρ is asymptotically equivalent to $jk_z^\alpha/\sqrt{v_l^\alpha}$ for uniaxial anisotropic medium. The latter expression should be carried together during the expansion. As a result, their first-level and second-level of asymptotic reflection coefficients are the same as equations 5.12 and 5.14.

5.2.2 Second Level Asymptotic Forms of Transmission Line Green's Function

A) $m = n$

The asymptotic form of the transmission line Green's functions appearing in the spectral LMGFs have three components in general as we discussed in chapter 2, corresponding to the direct radiation and reflection from lower and upper boundaries. Taking I_i as an example, when the observation and source points are in the same layer, its asymptotic form is

$$
I_i^{\alpha,\infty} = \frac{1}{2}\left[\pm e^{-jk_{z\ell}\varsigma_1} + \overleftarrow{\Gamma}_\ell^{\alpha,\infty} e^{-jk_{z\ell}\varsigma_2} - \overrightarrow{\Gamma}_\ell^{\alpha,\infty} e^{-jk_{z\ell}\varsigma_3}\right]. \tag{5.16}
$$

Here the "+" and "-" sign depends on if $z > z'$ or $z < z'$ and $\varsigma_1 = |z - z'|$, $\varsigma_2 = |z + z' - 2z_m|$ and $\varsigma_3 = |2z_{m+1} - z - z'|$ correspond to the traveling distance of the direct wave, reflected wave from the lower boundary and reflected wave from the upper boundary respectively.

The corresponding two-level asymptotic forms can be further expressed as

$$I_{\mathrm{i}}^{\alpha,\infty} = i_{\mathrm{i}}^{\alpha,1,\infty} + \frac{1}{k_\rho^2} i_{\mathrm{i}}^{\alpha,2,\infty} \tag{5.17}$$

with $i_{\mathrm{i}}^{\alpha,1,\infty}$ and $i_{\mathrm{i}}^{\alpha,2,\infty}$ being the first-level and second-level asymptotic coefficients of I_{i}^{α} respectively, each having the form

$$i_{\mathrm{i}}^{\alpha,1,\infty} = \frac{1}{2}\left[\pm e^{-jk_{z\ell}\varsigma_1} + \overleftarrow{\Gamma}_{\ell}^{\alpha,1,\infty} e^{-jk_{z\ell}\varsigma_2} - \overrightarrow{\Gamma}_{\ell}^{\alpha,1,\infty} e^{-jk_{z\ell}\varsigma_3}\right] \tag{5.18}$$

and

$$i_{\mathrm{i}}^{\alpha,2,\infty} = \frac{1}{2}\left[\overleftarrow{\Gamma}_{\ell}^{\alpha,2,\infty} e^{-jk_{z\ell}\varsigma_2} - \overrightarrow{\Gamma}_{\ell}^{\alpha,2,\infty} e^{-jk_{z\ell}\varsigma_3}\right]. \tag{5.19}$$

A) $m = n \pm 1$

When the observation and source points are in adjacent layers, its asymptotic form contains only the transmitted part from the source point:

$$I_{\mathrm{i}}^{\alpha,\infty} = \frac{1}{2}\left[\pm e^{-jk_{z\ell}|z-z'|}\left(1 - \overrightarrow{\overleftarrow{\Gamma}}_{\ell}^{\alpha,\infty}\right)\right], \quad m = n \pm 1. \tag{5.20}$$

In this case, its first-level asymptotic coefficient is

$$i_{\mathrm{i}}^{\alpha,1,\infty} = \frac{1}{2}\left[\pm e^{-jk_{z\ell}|z-z'|}\left(1 - \overrightarrow{\overleftarrow{\Gamma}}_{\ell}^{\alpha,1,\infty}\right)\right], \quad m = n \pm 1, \tag{5.21}$$

and its second-level asymptotic coefficient is

$$i_{\mathrm{i}}^{\alpha,2,\infty} = \frac{1}{2}\left[\pm e^{-jk_{z\ell}|z-z'|}\left(-\overrightarrow{\overleftarrow{\Gamma}}_{\ell}^{\alpha,2,\infty}\right)\right], \quad m = n \pm 1. \tag{5.22}$$

Due to the context, the other components of the transmission line Green's functions such as V_{v}, V_{i} and I_{v} will be listed in the Appendix B for reference.

5.3 Curl-Type Layered Medium Green's Functions

It is seen from chapter 3 that six independent Hankel transforms, which are expressed as generalized Sommerfeld Integrals (SIs), are used to form the curl-type LMGF in the spatial domain. These integrals are

$$I_3 = S_0\left\{I_i^h + I_i^e\right\}, \quad I_4 = S_0\left\{V_v^e + V_v^h\right\}, \tag{5.23}$$

$$I_{11} = S_1\left\{k_\rho V_i^h\right\}, \quad I_{12} = S_1\left\{k_\rho I_v^e\right\}, \tag{5.24}$$

$$I_{13} = S_2\left\{I_i^e - I_i^h\right\}, \quad I_{14} = S_2\left\{V_v^h - V_v^e\right\}. \tag{5.25}$$

Using two-levels of singularity subtractions, the integrals are calculated in the following manner

$$I = I^{L1} + I^{L2} + I^{Res}. \tag{5.26}$$

Here the integrals I^{L1} and I^{L2} are denoted as first-level and second-level of singular components, respectively, and are calculated using closed-form or easily-calculated identities. The residual integral I^{Res} does not have a closed form in general. However, because the remaining integrand I^{Res} after a two-levels of asymptotic subtraction decays very rapidly in the spectral domain, fast convergence can be reached using the weighted average method.

To be more specific, take I_3 as an example, its first-level of singularity term is denoted as

$$I_3^{L1} = S_0\left\{\frac{1}{2}; \pm 1, \overleftarrow{\Gamma}^{h,1,\infty}, -\overrightarrow{\Gamma}^{h,1,\infty}\right\} + S_0\left\{\frac{1}{2}; \pm 1, \overleftarrow{\Gamma}^{e,1,\infty}, -\overrightarrow{\Gamma}^{e,1,\infty}\right\}, \tag{5.27}$$

its second-level of singularity term is denoted as

$$I_3^{L2} = S_0\left\{\frac{v^h}{2(jk_z^h)^2}; 0, \overleftarrow{\Gamma}^{h,2,\infty}, -\overrightarrow{\Gamma}^{h,2,\infty}\right\} + S_0\left\{\frac{v^e}{2(jk_z^e)^2}; 0, \overleftarrow{\Gamma}^{e,2,\infty}, -\overrightarrow{\Gamma}^{e,2,\infty}\right\}, \tag{5.28}$$

and its remaining integral is

$$I_3^{\mathrm{Res}} = S_0 \left\{ \left(I_i^h - I_i^{h,1,\infty} - I_i^{h,2,\infty} \right) + \left(I_i^e - I_i^{e,1,\infty} - I_i^{e,2,\infty} \right) \right\}. \tag{5.29}$$

After we perform all the asymptotic subtractions, it is found that all the second-level forms behave in the following fashion :

$$S_0 \left\{ \frac{e^{-jk_z^\alpha |\varsigma|}}{2(jk_z^\alpha)^2} \right\}, S_1 \left\{ \frac{e^{-jk_z^\alpha |\varsigma|}}{2jk_z^\alpha k_\rho} \right\}, S_2 \left\{ \frac{e^{-jk_z^\alpha |\varsigma|}}{2(jk_z^\alpha)^2} \right\}. \tag{5.30}$$

The evaluation of these integrals will be introduced in the following section.

5.3.1 Closed-Form or Easily-Computed Identities

As discussed in the previous section, a key feature of the singular extraction is the the existence of corresponding closed-form or easily-calculated identities representing the Hankel transforms of asymptotic quantities. The SRIs for the evaluation of first-level asymptotic forms can be found in Chapter 2 and Chapter 3. For the evaluation of the second-level asymptotic forms, the corresponding SRIs are introduced.

The first identity, also called half-line source potential is introduced previously in Chapter 3,

$$I_M = S_0 \left\{ \frac{e^{-jk_z^\alpha |\varsigma|}}{2(jk_z^\alpha)^2} \right\} = \frac{1}{\nu^\alpha} \int_{|\varsigma|}^{\infty} \frac{e^{-jk_t R^\alpha}}{4\pi R^\alpha} ds. \tag{5.31}$$

It contains a logarithmic singularity embedded when the observation point approaches to the source point. The unbounded logarithmic singularity exists in the second-level asymptotic forms due to the reflection from boundaries. If only one-level singularity extraction is performed, this unbounded singularity not only makes the integral difficult to converge near the source point, but also its singular behavior reduces the interpolation accuracy of LMGF near the source point.

The rest of the identities are listed below

$$I_O = S_1 \left\{ \frac{e^{-jk_z^\alpha |\varsigma|}}{2jk_z^\alpha k_\rho} \right\} = \frac{e^{-jk_t|\varsigma|} - e^{-jk_t R^\alpha}}{4\pi jk_t\rho}, \tag{5.32}$$

$$I_P = S_1 \left\{ \frac{e^{-jk_z^\alpha |\varsigma|}}{2(jk_z^\alpha)^2 k_\rho} \right\} = \frac{1}{4\pi jk_t\rho} \left(\frac{e^{-jk_t|\varsigma|}}{jk_t} - \int_{|\varsigma|}^{\infty} e^{-jk_t R^\alpha} dz \right), \tag{5.33}$$

$$I_Q = S_2 \left\{ \frac{e^{-jk_z^\alpha |\varsigma|}}{2(jk_z^\alpha)^2} \right\} = \frac{2}{\rho} I_P - I_M, \tag{5.34}$$

They are numbered alphabetically as a continuation of SIRs in Chapter 3. The Hankel transform P above does not have a closed form. However, its right hand side can be viewed as the derivative of the HLSP with respect to the transverse wavenumber k_t of the uniaxial medium with an anisotropy ratio.

5.3.2 Derivative of Half-Line Source Potential(HLSP)

The derivative of the HLSP is defined as

$$A_z = \int_z^{\infty} e^{-jk_t R^\alpha} ds. \tag{5.35}$$

Again, we can expand the binomial expansion method and numerical integration method to evaluate this integral easily.

A) Binomial Expansion Method

Using the binomial expansion method, the integral can be computed as the power series below:

$$A_z^\alpha(\rho, z) = \sum_{n=0}^{\infty} C_n r \left(\frac{\rho/\sqrt{\nu^p}}{r} \right)^{2n} E_{2n}(jk_t r). \tag{5.36}$$

B) Numerical Integration Method

Using the numerical integration method, the integral can be broken into two parts, from 0 to z and from 0 to ∞,

$$A_z^\alpha(\rho,z)=\int_0^\infty e^{-jk_tR^\alpha}ds-\int_0^z e^{-jk_tR^\alpha}ds. \tag{5.37}$$

The integral from 0 to ∞ can be evaluated in closed form, as it is viewed as the derivative of the zero-order Hankel function with respect to k_t,

$$\int_0^\infty e^{-jk_tR^\alpha}ds=j\frac{d}{dk_t}\int_0^\infty\frac{e^{-jk_tR^\alpha}}{R^\alpha}ds=\frac{\pi}{2}\frac{d}{dk_t}H_0^2\left(k_t\frac{\rho}{\sqrt{\nu^\alpha}}\right). \tag{5.38}$$

The derivative of the zero-order Hankel function is a first-order Hankel function [61],

$$\frac{d}{dk_t}H_0^2\left(k_t\frac{\rho}{\sqrt{\nu^\alpha}}\right)=\frac{\rho}{\sqrt{\nu^\alpha}}H_1^2\left(k_t\frac{\rho}{\sqrt{\nu^\alpha}}\right). \tag{5.39}$$

The latter integral from 0 to z needs be computed numerically based on the oscillation of the integrand

$$\Delta A_z^\alpha=\int_0^z e^{-jk_tR^\alpha}ds. \tag{5.40}$$

After the computation of two parts separately, we may obtain the final expression as

$$A_z^\alpha(\rho,z)=-\frac{\pi\rho}{2\sqrt{\nu^p}}H_1^2\left(k_t\frac{\rho}{\sqrt{\nu^\alpha}}\right)-\Delta A_z^\alpha. \tag{5.41}$$

5.4 Numerical Examples

This section presents examples that demonstrate the properties of the two-level asymptotic subtraction method.

We use the same configuration for the second example in chapter 2. The integrand in the spectral domain of I_3 and I_4 is plotted in Figure 5.2.

Each level of asymptotic subtraction results in a spectral integrand that decays faster by a factor of k_ρ^2. Tables 5.1 and 5.2 list the decaying order of all the integrals

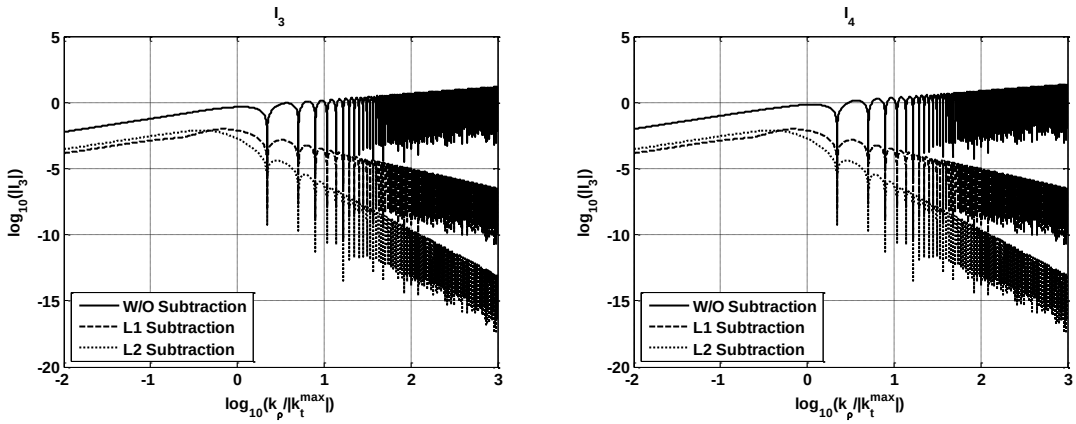

Figure 5.2. Example of integrand decaying behavior for I_3 (left) and I_4 (right) by using two-levels of asymptotic subtraction.

respect to k_ρ for the algebraically decaying case.

Table 5.1. Decay order of Integrals $I_1 - I_7$ using two levels singularity extraction

Integral	I_1	I_2	I_3	I_4	I_5	I_6	I_7
W/O	0.5	0.5	-0.5	-0.5	0.5	1.5	0.5
L1	2.5	2.5	1.5	1.5	2.5	3.5	2.5
L2	4.5	4.5	3.5	3.5	4.5	5.5	4.5

Table 5.2. Decay order of Integrals $I_8 - I_{14}$ using two levels singularity extraction

Integral	I_8	I_9	I_{10}	I_{11}	I_{12}	I_{13}	I_{14}
W/O	1.5	0.5	0.5	-0.5	-0.5	-0.5	-0.5
L1	3.5	2.5	2.5	1.5	1.5	1.5	1.5
L2	5.5	4.5	4.5	3.5	3.5	3.5	3.5

The second-level asymptotic subtraction not only gives a faster decaying integrand but it also removes the logarithmic singularity of the integral in the spatial domain. The remaining spectral integrals are then calculable at every point (they remain bounded) and are sufficiently smooth to permit efficient and accurate interpolation in the spatial domain. Figures 5.3 - 5.6 plot the remaining integral using one-level

and two-level singularity extraction for I_3, I_4, I_{12} and I_{14}. The observation point is on the interface of two adjacent layers. For I_3 and I_4, the remaining logarithmic singularity after one-level singularity extraction (on the left) is removed (on the right). The remaining integral (on the right) is bounded and smooth enough for accurate interpolation. for I_{12} and I_{14}, even though the integral is bounded after one-level singularity extraction, by using second-level singularity extraction the remaining integral is even smoother for more accurate interpolation. Because the integrals I_{11} and I_{13} are dual to I_{12} and I_{14}, they are not shown here due to the limited context.

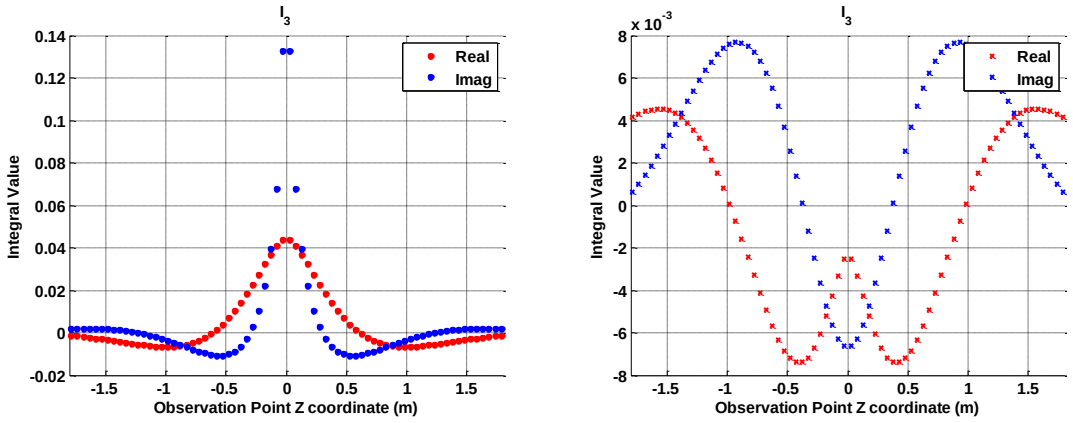

Figure 5.3. The remaining integral I_3 along the observation line using one-level (left) and using two-level (right) singularity extraction.

The last example, we test the efficiency of the two level singularity extraction. As discussed previously, the most difficult case for convergence is when the source and observation points both sit on the interface of layers. In this case, the integrand only decays algebraically. Moreover, some integrals, i.e. integrals associated with curl-type operators, diverge mathematically and can only be interpreted in a limiting sense. We test our code by putting the observation point at a distance of $\rho = 0, 10^{-3} \times \lambda_0, 10^{-2} \times \lambda_0, 10^{-1} \times \lambda_0, \lambda_0$ away from the source point on the interface as shown in Figure 5.8. The integral I_1 and I_3 are selected for study because they

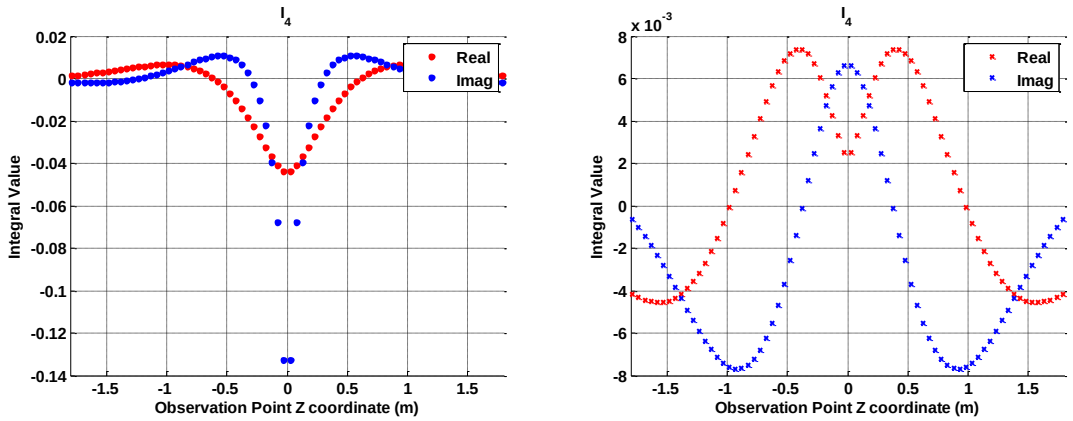

Figure 5.4. The remaining integral I_4 along the observation line using one-level (left) and using two-level (right) singularity extraction.

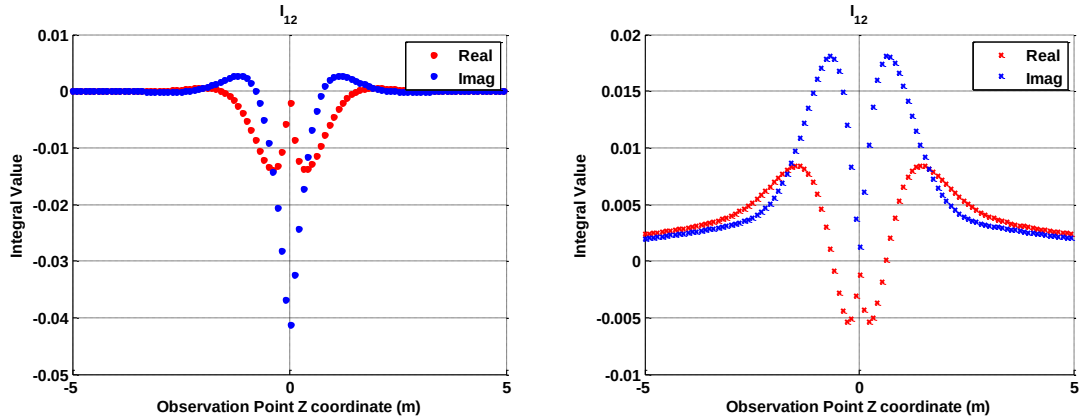

Figure 5.5. The remaining integral I_{12} along the observation line using one-level (left) and using two-level (right) singularity extraction.

represent different decaying orders. For each integral, we use one-level and two-level singularity extraction and compare the CPU time. The CPU time is the average CPU time found by repeating the calculation 1000 times. Tables 5.3 and 5.4 list the CPU time for various configurations when the convergence criteria is set to 10^{-6} and 10^{-8} respectively.

For integral I_1, the two-level singularity extraction case cost some extra time

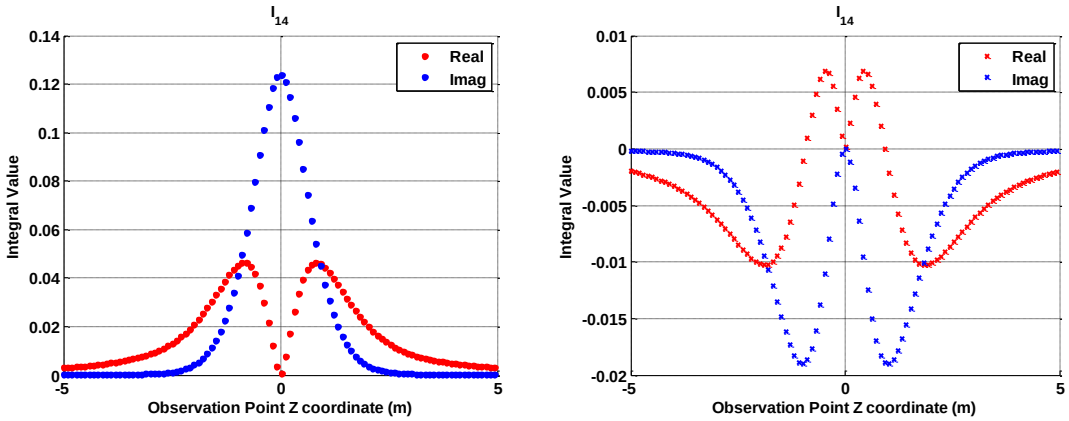

Figure 5.6. The remaining integral I_{14} along the observation line using one-level (left) and using two-level (right) singularity extraction.

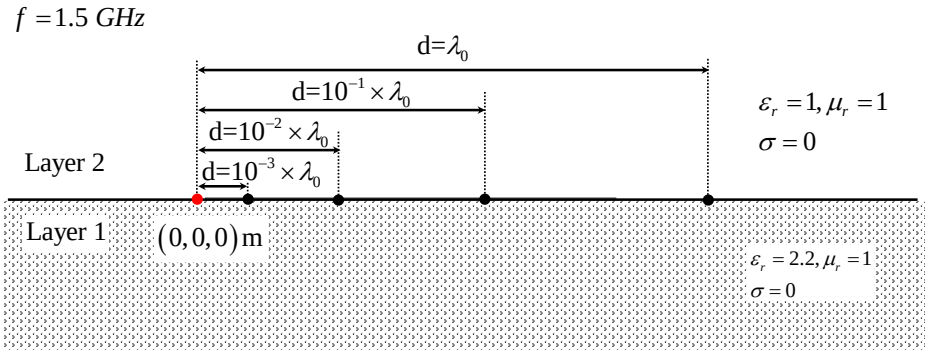

Figure 5.7. The configuration for CPU time test of integrals performing one-level and two-level singularity extractions.

compared to one-level singularity extraction case due to performing of the second-level asymptotic subtraction. When the observation point is less than a wavelength, no significant improvement of CPU time is observed because of the use of the weighted average method. For distance $\rho > \lambda$, the two-level singularity extraction can accelerate

Table 5.3. CPU time (Unit : ms) for I_1 and I_3 at different horizontal distances on the interface by using L1 and L2 extraction(Convergence $\varepsilon = 10^{-6}$).

Integral	Level	$\rho = 0$	$\rho = 10^{-3}\lambda_0$	$\rho = 10^{-2}\lambda_0$	$\rho = 10^{-1}\lambda_0$	$\rho = \lambda_0$
I_1	L1	0.266	0.703	0.531	0.468	5.094
I_1	L2	0.437	1.312	0.625	0.547	2.203
I_3	L1	N/C[1]	0.984	0.797	0.766	0.750
I_3	L2	0.406	1.281	0.500	0.391	0.781

[1] "N/C" is denoted as "Not Convergent".

Table 5.4. CPU time (Unit : ms) for I_1 and I_3 at different horizontal distances on the interface by using L1 and L2 extraction(Convergence $\varepsilon = 10^{-8}$).

Integral	Level	$\rho = 0$	$\rho = 10^{-3}\lambda_0$	$\rho = 10^{-2}\lambda_0$	$\rho = 10^{-1}\lambda_0$	$\rho = \lambda_0$
I_1	L1	0.438	1.781	0.984	1.266	12.469
I_1	L2	0.672	2.328	1.188	1.000	6.031
I_3	L1	N/C[1]	2.094	1.641	2.250	29.766
I_3	L2	0.672	2.359	1.125	1.375	7.140

[1] "N/C" is denoted as "Not Convergent".

the convergence one time faster compared to one-level of singularity extraction case.

For integral I_3, when $\rho = 0$, the convergence is never achieved when only the one-level singularity extraction is used. When ρ is around $10^{-3} \times \lambda$, again a little extra time cost due to the second-level asymptotic subtraction is observed. when $\rho > 10^{-2} \times \lambda$, the two-levels of singularity extraction reach convergence faster for both convergence criteria ($\varepsilon = 10^{-6}$ and $\varepsilon = 10^{-8}$).

When the distance between source and observation point gets larger and larger, the CPU time will increase. This is because the integrand oscillates faster and faster, and denser and denser sampling points in spectral domain are needed in order to capture the oscillating behavior of the integrand to achieve convergence. In this case, other methods such as the famous steepest descent path method which is suitable for

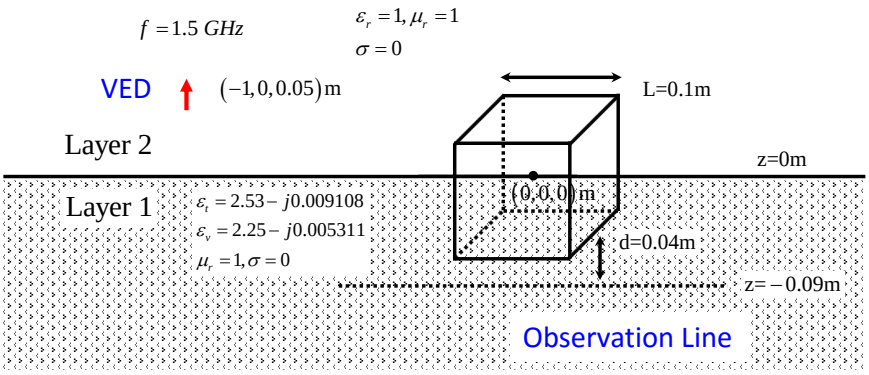

Figure 5.8. The configuration setting of cpu time test for integrals performing one-level and two-levels singularity extractions.

far field interactions may also be used to accelerate the convergence.

Table 5.5. CPU time (Unit : second) of different steps in MFIE formulation (overall convergence $\varepsilon = 10^{-6}$).

Pts/λ_1	SIs	Interp	Grn's Fn	Inner Product	Solution	Total
20	39.08	13.05	52.13	199.07	20.30	271.50
40	261.37	14.13	275.50	205.25	20.50	501.25
80	1679.61	17.50	1697.11	202.14	20.69	1919.94

Table 5.6. Speed-up factors for Green's function evaluation and matrix filling

Pts/λ_1	Grn's Fn Speed-up	Matrix fill Speed-up
20	347.78	73.0
40	65.80	38.2
80	10.68	9.66

As a last example, we consider a half-space problem that a rectangular perfect electric conductor penetrating into soil sand. Tha layer above is air ($\epsilon_r = 1.0, \mu_r = 1.0$, $\sigma = 0$ S/m) and the layer below is anisotropic soil ($\epsilon_{rt} = 2.53 - j0.009108, \epsilon_{rv} = 2.25 - j0.005311, \mu_r = 1.0$, $\sigma = 0$ S/m). The length of the cube is 0.1 m and its centroid is located in the origin. The cubic is excited by a vertical electric dipole

located in $(-1.0, 0.0, 0.5)$ m as illustrated in Figure 7.16. The operating frequency is 1.5 GHz. The number of triangles is 1508 and total number of unknowns is 2262. In order to demonstrate the efficiency of this method, we list the CPU time of different steps on a intel(R) Core i7-4090 platform desktop in Table 5.5. The first column list the interpolation density per wavelength. The second column gives the CPU time to evaluate the Sommerfeld integrals. The third column lists the CPU time cost on performing interpolation. The fourth column gives the time consumed in computing Green's function and the fifth column is time cost for element matrix evaluation and matrix assembling. The sixth column lists the time for solving matrix equations and the last one gives the total time. The speed-up factor for evaluation of Green's function and the matrix filling is also listed in Table 5.6.

Chapter 6

Singularity of Curl-Type Operators

6.1 Motivation

The singular behavior of the Green's functions plays an very important role in the formulation of integral equations. For example, in free space, the magnetic field integral equation (MFIE), is a second-kind Fredholm integral equation as

$$\frac{\mathbf{J^s}}{2} - \hat{n} \times \int\limits_{p.v} \nabla \times \underline{\underline{\mathcal{G}}}(\mathbf{r}, \mathbf{r}') \cdot \mathbf{J^s} ds' = \hat{n} \times \mathbf{H}^i_{\tan}, \underline{r} \uparrow S. \tag{6.1}$$

The $\frac{1}{2}\mathbf{J^s}$ contribution pulled out from the integral is due to the jump discontinuity of the curl-type operator for free space. After the singularity extraction, the rest of the integral is interpreted in a Cauchy principal value sense.

In Chapter 5, we studied two-level asymptotic subtraction for curl-type operators in spectral domain. Their closed-form expression in spatial domain reveals all the singularity in spatial domain. We will see in this chapter that the singularity of curl-type Green's function for layered medium behaves quite differently from that for free space. As a result, the magnetic field integral equation formulation should be modified correspondingly [45].

6.2 Singularity Analysis of Curl-Type Operator

In layered medium, the singularity contribution not only comes from the source directly, but also from the image source. In fact, the singular behavior of contributions from image sources is rather richer than direct radiation from source in homogeneous medium.

Consider a two layered medium illustrated in Figure 6.1 with its side view as

Figure 6.2,

Figure 6.1. Side view of a RWG current patch on the interface of a two layered medium.

The curl-type operator associated with electric current is expressed as

$$\nabla \times \underline{\underline{\mathcal{G}}}^{A}(\mathbf{r},\mathbf{r}') = \begin{bmatrix} -\frac{1}{2}\sin 2\gamma I_{13} & \frac{1}{2}\left(I_3 + \cos 2\gamma I_{13}\right) & -\frac{1}{j\omega\varepsilon_0\varepsilon_z'}\sin\gamma I_{12} \\ \frac{1}{2}\left(-I_3 + \cos 2\gamma I_{13}\right) & \frac{1}{2}\sin 2\gamma I_{13} & \frac{1}{j\omega\varepsilon_0\varepsilon_z'}\cos\gamma I_{12} \\ \frac{\sin\gamma}{j\omega\mu_0\mu_z} I_{11} & -\frac{\cos\gamma}{j\omega\mu_0\mu_z} I_{11} & 0 \end{bmatrix}. \quad (6.2)$$

Since the current of the patch flows on the surface of the interface and we are interested in the transverse component of the magnetic field, our study will concentrate on the transverse components, namely $\hat{\mathbf{x}}\hat{\mathbf{x}}, \hat{\mathbf{x}}\hat{\mathbf{y}}, \hat{\mathbf{y}}\hat{\mathbf{x}}, \hat{\mathbf{y}}\hat{\mathbf{y}}$ components of the curl-type operator. They are expressed as the combination of two independent integrals I_3 and $I_{13}\cos 2\gamma$ or $I_{13}\sin 2\gamma$.

A) I_3

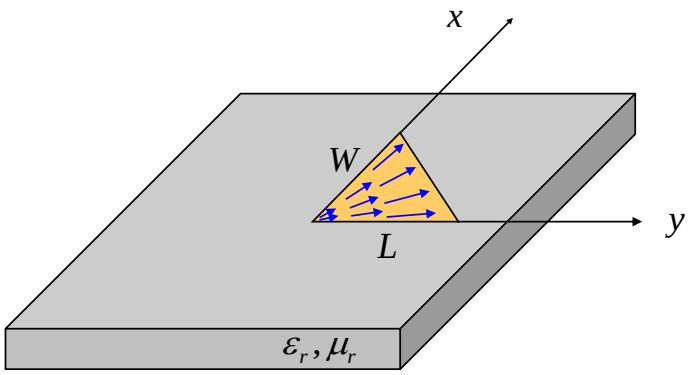

Figure 6.2. Rotated view of a RWG current patch on the interface of a two layered medium.

The first-level singular form of I_3 is denoted as

$$I_3^{L1} = S_0 \left\{ \frac{1}{2}; \pm 1, \overleftarrow{\Gamma}^{h,1,\infty}, -\overrightarrow{\Gamma}^{h,1,\infty} \right\} + S_0 \left\{ \frac{1}{2}; \pm 1, \overleftarrow{\Gamma}^{e,1,\infty}, -\overrightarrow{\Gamma}^{e,1,\infty} \right\}, \tag{6.3}$$

and its closed form can be obtained via identity B:

$$I_B = S_0 \left\{ \frac{e^{-jk_z^\alpha |\varsigma|}}{2} \right\} = \frac{1}{\nu^\alpha} |\varsigma| \left(1 + jk_t R^\alpha\right) G^\alpha. \tag{6.4}$$

The identity B is the off-diagonal term of the curl-type operator for homogeneous media which produces a delta singularity only, hence the first-level singularity of curl-type operator for layered medium only produce a localized delta singularity similar to its counterpart in free space, but with a different coefficient due to reflection.

Its corresponding P.V. integral vanishes on the interface plane as well,

$$I_3^{L1} = \left(\operatorname{sgn}|z - z'| + \frac{\overleftarrow{\Gamma}^{h,1,\infty} + \overleftarrow{\Gamma}^{e,1,\infty}}{2} \right) \delta(\rho - \rho'). \tag{6.5}$$

The second-level singular form of I_3 is denoted as

$$I_3^{L2} = S_0 \left\{ \frac{v^h}{2(jk_z^h)^2}; 0, \overleftarrow{\Gamma}^{h,2,\infty}, -\overrightarrow{\Gamma}^{h,2,\infty} \right\} + S_0 \left\{ \frac{v^e}{2(jk_z^e)^2}; 0, \overleftarrow{\Gamma}^{e,2,\infty}, -\overrightarrow{\Gamma}^{e,2,\infty} \right\} \tag{6.6}$$

and its closed form can be obtained via the identity M

$$I_M = S_0 \left\{ \frac{e^{-jk_z^\alpha|\varsigma|}}{2(jk_z^\alpha)^2} \right\} = \frac{1}{\nu^\alpha} \int_{|\varsigma|}^{\infty} \frac{e^{-jk_t R^\alpha}}{4\pi R^\alpha} ds. \tag{6.7}$$

This term becomes singular when the source and observation points both sit on the same interface and the observation point approaches the source point. In this case, we have $|\varsigma| = 0$, and the half line source potential becomes a half of the Hankel function as

$$G_z^\alpha(\rho, 0) = \frac{1}{8j} H_0^2 \left(k_t \rho / \sqrt{\nu^\alpha} \right). \tag{6.8}$$

Thus it is clear that the second-level singular form of I_3 contributes a logarithmic singularity with the coefficient of the second-level asymptotic reflection coefficient

$$I_3^{L2} = \sum_{\alpha=e,h} \overleftarrow{\Gamma}^{\alpha,2,\infty} \frac{1}{\nu^\alpha} \frac{1}{8j} H_0^2 \left(k_t \rho / \sqrt{\nu^\alpha} \right). \tag{6.9}$$

B) $I_{13} \cos 2\gamma$ or $I_{13} \sin 2\gamma$

The integral I_{13} only contains a one-level singularity, and its second-level "singular" contribution is bounded. So we focus on its first-level singularity here. Let us express I_{13} as

$$I_{13} = I_{13}^{L1} + I_{13}^{\text{Res}}, \tag{6.10}$$

with I_{13}^{Res} and I_{13}^{L1} being

$$I_{13}^{\mathrm{Res}} = S_2\left\{\left(I_i^e - I_i^{e,1,\infty}\right) - \left(I_i^h - I_i^{h,1,\infty}\right)\right\}, \tag{6.11}$$

and

$$I_{13}^{L1} = S_2\left\{\frac{1}{2}; \pm 1, \overleftarrow{\Gamma}^{e,1,\infty}, -\overrightarrow{\Gamma}^{e,1,\infty}\right\} - S_2\left\{\frac{1}{2}; \pm 1, \overleftarrow{\Gamma}^{h,1,\infty}, -\overrightarrow{\Gamma}^{h,1,\infty}\right\}. \tag{6.12}$$

The first-level singularity can be obtained via the identity

$$I_L = S_2\left\{\frac{e^{-jk_z^\alpha|\varsigma|}}{2}\right\} = \frac{2}{\rho}I_E - I_B \tag{6.13}$$

with identity B being Eq. (6.4) and identity E being

$$I_E = S_1\left\{\frac{e^{-jk_z^\alpha|\varsigma|}}{2k_\rho}\right\} = \frac{R^\alpha e^{-jk_t|\varsigma|} - |\varsigma|\, e^{-jk_t R^\alpha}}{4\pi\rho R^\alpha}. \tag{6.14}$$

When I_{13} multiplies with $\sin 2\gamma$ or $\cos 2\gamma$, identity B doesn't produce a localized singularity or any principle value contribution. However, when $|\varsigma| = 0$, identity E produce a hyper singular behavior so that the first-level singularity of $I_{13}\sin 2\gamma$ and $I_{13}\cos 2\gamma$ is

$$\left(I_{13}\left\{\begin{array}{c}\cos 2\gamma\\ \\ \sin 2\gamma\end{array}\right\}\right)^{L1} = \left(\overleftarrow{\Gamma}^{e,1,\infty} - \overleftarrow{\Gamma}^{h,1,\infty}\right)\frac{1}{2\pi\rho^2}\left\{\begin{array}{c}\cos 2\gamma\\ \\ \sin 2\gamma\end{array}\right\}. \tag{6.15}$$

6.3 Handling Various Singular Integrals

Assume we have a RWG current patch sitting on the surface of two layers, the transverse magnetic field is expressed by

$$\begin{bmatrix} H_x \\ H_y \end{bmatrix} = \begin{bmatrix} (\nabla \times G)_{xx} & (\nabla \times G)_{xy} \\ (\nabla \times G)_{yx} & (\nabla \times G)_{yy} \end{bmatrix} \cdot \begin{bmatrix} J_x \\ J_y \end{bmatrix}. \tag{6.16}$$

Taking H_x as an example, we can expand it as

$$H_x = \frac{1}{2} \int_s -I_{13} \sin 2\gamma \, J_{sx}(x', y') + (I_3 + I_{13} \cos 2\gamma) \, J_{sy}(x', y') ds'. \tag{6.17}$$

The non-singular part of the above integral can be evaluated easily using standard Gauss−Legendre (GL) quadrature. It's the singular part of the integral that needs advanced numerical quadrature rules. By skipping the long coefficients explicitly in front of the individual integrals I_3 and I_{13} , the singular part of the above integral H_x is found to be described by three singular integrals listed below.

$$I^1 = \int_s \delta(\rho - \rho') \, J_{sy}(x', y') ds', \tag{6.18}$$

$$I^2 = \int_s H_0^2 \left(k_t \frac{\rho}{\sqrt{\nu^\alpha}} \right) \, J_{sy}(x', y') ds', \tag{6.19}$$

and

$$I^3 = \int_s \frac{1}{2\pi\rho^2} \begin{cases} \cos 2\gamma \, J_{sy}(x', y') \\ \sin 2\gamma \, J_{sx}(x', y') \end{cases} ds'. \tag{6.20}$$

The singular kernels for the above integrals I^1 ,I^2 and I^3 are $\delta(\rho - \rho')$, $\ln\rho$, $\frac{1}{\rho^2}\cos 2\gamma$ or $\frac{1}{\rho^2}\sin 2\gamma$ which are also called as delta function kernel, logarithmic singular kernel and hyper-singular kernel in source integration, respectively.

The so-called "singularity subtraction" schemes are usually employed to evaluate (near) singular integrals in the evaluation of reaction integrals. By using the singularity subtraction scheme, the terms having the same asymptotic behavior as the integrand at unbounded singularities are subtracted from the integrand and integrated analytically,

while the remained bounded difference integrand can be handled numerically by standard GL quadrature.

Recent literature has focused on the "singularity cancellation" scheme to evaluate the source singular integral. The singularity cancellation relies on the transformation Jacobian to cancel the singular kernel. The resulting integrand then becomes a smooth function easily to integrate numerically. Various transformations, like the "Extended Duffy", "Arcsinh", "Radial" and "Radial-Angular" transformation [86] were developed to handle $1/R$ singularities, while the "disc-triangle sub-domain division" integration scheme [87] and "AD-R1-L-AS" transformation [88] are developed to handle the $1/R^2$ singularity.

In our work, different schemes and transformations are proposed for the accurate evaluation of singular integrals in curl-type operators for layered media. They are described in the following sections in details.

6.3.1 Handling Delta Singularity

Handling the delta singularity is very simple because the delta function samples the current at the observation point:

$$I^1 = J_{sy}(\rho). \tag{6.21}$$

6.3.2 Handling Logarithm Singularity

Consider an observation point on the plane of the source triangle S'. Due to the integrand blowing up at the observation point, the source triangle S' is split into three subtriangles about the observation point

The integral can be written as the sum of three integrals, one for each subtriangular domain,

$$I(x,y) = \sum_{i=1}^{3} I_{st}^{i}(x,y), \tag{6.22}$$

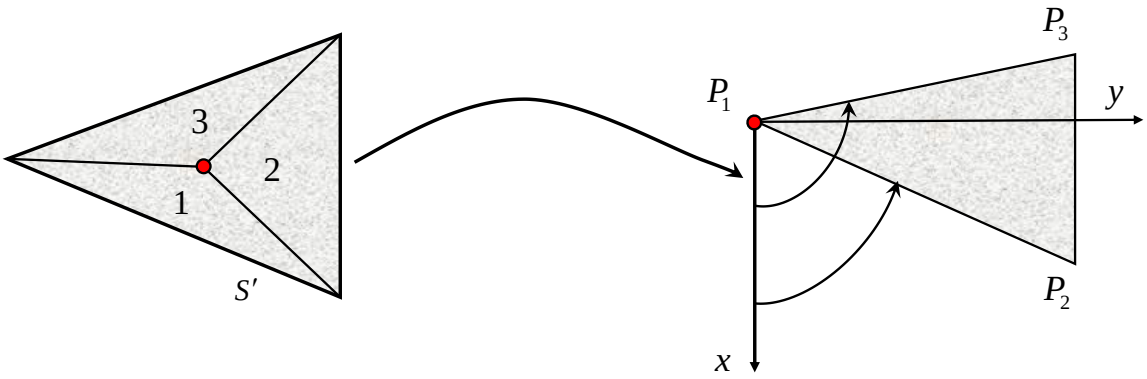

Figure 6.3. Illustration of handling logarithm singularity, the source triangle is divided into three sub-triangle. The red dot is the observation point.

where I_{st}^{i} is the integral on each subtriangular. If we define $f(\rho) = H_0^2\left(k_t\rho/\sqrt{\nu^{\alpha}}\right)$, the integral on each subtriangle becomes

$$I_{st}^{i}(x,y) = \int_{s} f(\rho)\ J_{sy}(\mathbf{r}')ds' = \int_{0}^{h}\int_{x'_L(y)}^{x'_U(y)} f(\rho)\ J_{sy}(\mathbf{r}')\,\rho dx'dy'. \tag{6.23}$$

Applying the transformation to the integral Eq. (6.23)

$$\varphi = \tan^{-1}\frac{y'}{x'}, \tag{6.24}$$

we obtain

$$I_{st}^{i}(x,y) = \int_{\varphi_L}^{\varphi_U}\int_{0}^{\frac{h}{\sin\varphi}} f(\rho)\ J_{sy}(\mathbf{r}')\,\rho d\varphi d\rho. \tag{6.25}$$

Clearly, the logarithmic singularity is canceled at the origin. if we normalize the inner

integral to the unit interval via the transformation

$$\rho = \eta \frac{h}{\sin \varphi}, \tag{6.26}$$

the integral Eq. (6.25) becomes

$$I_{st}^{i}(x,y) = \int_{\varphi_L}^{\varphi_U} \frac{h}{\sin \varphi} \int_{0}^{1} f(\rho)\ J_{sy}(\mathbf{r}')\, \rho d\varphi d\eta. \tag{6.27}$$

Now the triangular domain is transformed into a rectangular domain as shown in Figure 6.4. The integral now can be numerically evaluated using a standard Gauss-Legendre integration scheme for transverse variables. For the radial integral, a "MRW" integration scheme [89–92] which was designed to handle logarithm singularity efficiently can be used. After transformation of the sampling points back to the global coordinates, the integral can be evaluated in a standard GL quadrature rule fashion as

$$I_{st}^{i}(x,y) = \sum_{k} W_k f(\rho)\ J_{sy}(\mathbf{r}'), \tag{6.28}$$

where

$$W_k = w_i w_j \frac{h}{\sin \varphi_i} f(\rho_{ij})\ J_{sy}(\mathbf{r}'_{ij})\, \rho_{ij}, \tag{6.29}$$

and we assume a double-to-single index correspondence $i, j \leftrightarrow k$ with w_i and w_j being the i-th and j-th GL weights respectively.

6.3.3 Handling Hyper-Singularity

The efficient handling of the hyper singular integral in Eq. (6.15) is a very difficult and challenging task. Extensive research has been conducted to evaluate the vector integrals involving hyper-singular and near-hyper-singular kernels [88], [93–95]. In order to accurately cancel the hyper singular kernel, we propose a two step approach similar to [87]. The source triangular patch is divided into four parts: one disc region

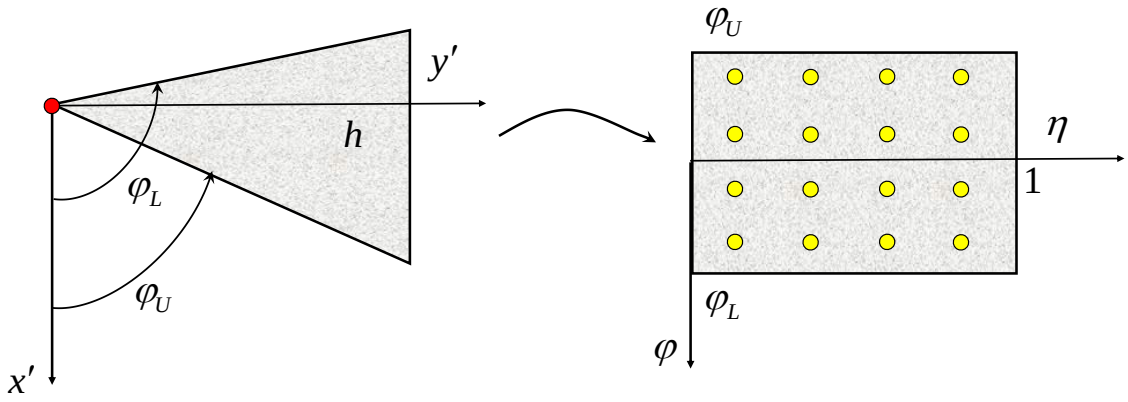

Figure 6.4. The subtriangle is transformed to a rectangular domain. the so-called "MRW" and standard GL integration scheme are used to perform the integration in the radial and transverse direction.

and three subtriangular domain and the integral Eq. (6.15) is written as the sum of four integrals,

$$I(x,y) = I_{disc}(x,y) + \sum_{i=1}^{3} I_{st}^{i}(x,y), \tag{6.30}$$

where I_{disc} is the integral over the circular disc domain, and the I_{st}^{i} is the integral on each subtriangle [87], [96]. We will see that I_{disc} integrates to zero if we use RWG basis functions to represent the source current. For subtriangular integral, we develop a transformation to exactly cancel the singular part of the kernel and the integration domain is mapped to a rectangular domain similar to handling the logarithmic singularity as discussed in the previous section.

A) Circular Disc Integration

Figure 6.6 shows the integration domain of $I_{annulus}$ and the corresponding local coordinates, where a is the radius of the circular disc and γ is the angle of observation point to source point respecting to x-axis on the transverse plane.

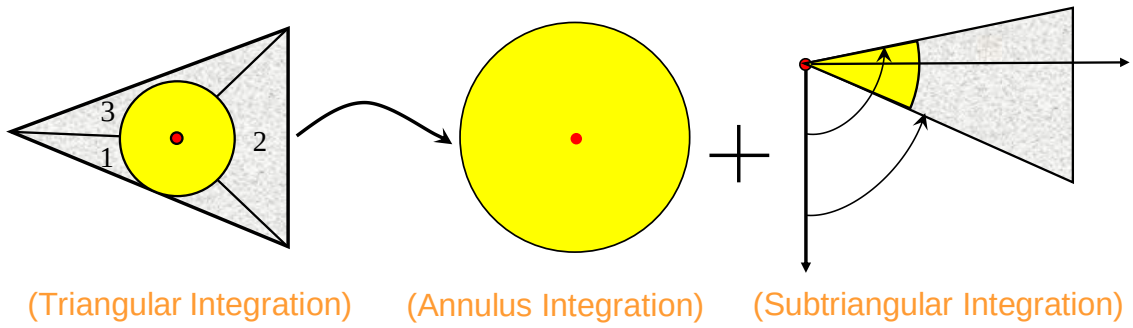

Figure 6.5. Illustration of procedures for handling hyper singular integral. The triangular domain is divided into a disc region and three sub-triangular regions.

$$I_{annulus} = \int_{S_a} \frac{1}{2\pi\rho^2} \cos 2\gamma J_{sy}\left(\mathbf{r}'\right) ds'. \tag{6.31}$$

Firstly we use the radial transformation to perform the integration in polar coordinates, and one-order of the singularity is reduced by the radial transform Jacobian $J = \rho$,

$$I_{annulus} = \frac{1}{2\pi} \int_0^{2\pi} \int_\delta^a \frac{1}{\rho} \cos 2\gamma J_{sy}\left(\mathbf{r}'\right) d\rho d\gamma. \tag{6.32}$$

Then we apply the transformation in the following

$$du = \frac{1}{\rho} d\rho, \tag{6.33}$$

and switch the order of integration so that

$$I_{annulus} = \frac{1}{4\pi} \int_0^{2\pi} \int_{-\infty}^{\ln a} \cos 2\gamma J_{sy}\left(\mathbf{r}'\right) du d\gamma = \frac{1}{4\pi} \int_{-\infty}^{\ln a} \int_0^{2\pi} \cos 2\gamma J_{sy}\left(\mathbf{r}'\right) du d\gamma. \tag{6.34}$$

Suppose the current is represented by an RWG basis function associated with vertex i on a planar triangular patch, which can be expressed in a Fourier expansion about $r' = r$,

$$J_{sy}(\mathbf{r}') = [\Lambda_i^e(\mathbf{r}')]_y = \left[\frac{\mathbf{r}' - \mathbf{r}_i}{h_i}\right]_y = \left[\frac{(\mathbf{r} - \mathbf{r}_i) - (\mathbf{r} - \mathbf{r}')}{h_i}\right]_y = \frac{(y - y_i)}{h_i} - \rho \sin\gamma. \quad (6.35)$$

Substituting the current into the above integral in Eq. (6.34), we can see the inner integral vanishes by the orthogonality of Fourier series.

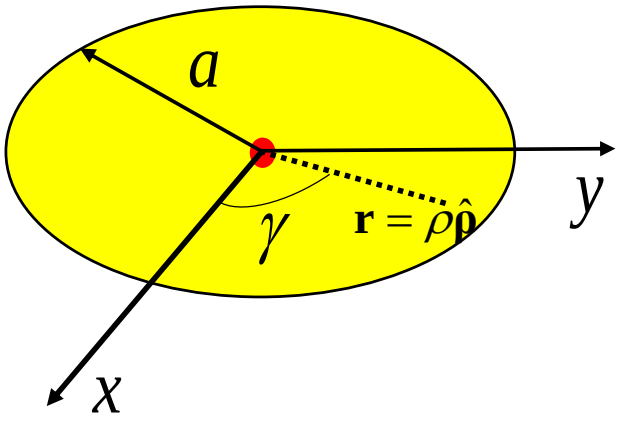

Figure 6.6. The integration domain of $I_{annulus}$ and the corresponding local coordinates, where a is the radius of the circular disc and γ is the angle of observation point to source point with respect to the x-axis on the transverse plane.

B) Subtriangle Integration

Figure 6.7 shows the integrand domain of I_{st} and the corresponding local coordinates. The y'-axis in local coordinate system (x', y') is defined in the direction of the height vector of subtriangle 1. The angular variable γ is defined in global coordinates. The subtriangle integration is expressed as

$$I_{st} = \int_{S'} \frac{1}{2\pi\rho^2} \cos 2\gamma J_{sy}(\mathbf{r}')\, dS' \quad (6.36)$$

Again if we perform the integral in polar coordinates

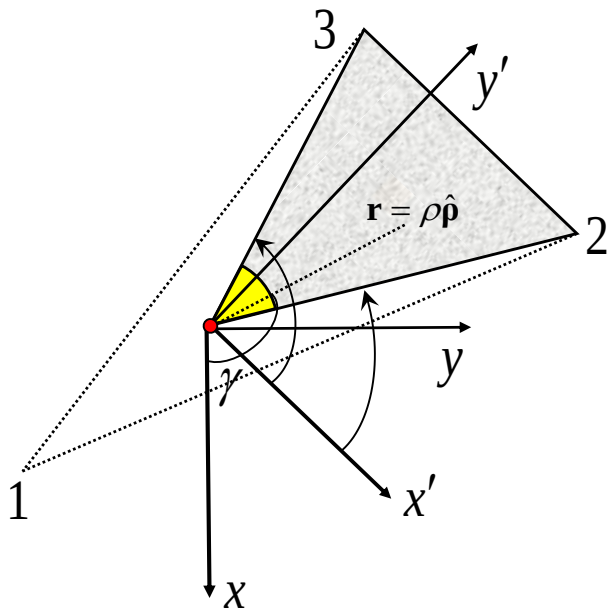

Figure 6.7. Illustration of sub-triangle integration domain and coordinates. The y'-axis in local coordinates (x', y') is defined in the direction of the height vector of subtriangle 1.

$$I_{st} = \frac{1}{2\pi} \int_{\varphi_U}^{\varphi_L} \int_{a}^{\frac{h}{\sin\varphi}} \frac{1}{\rho} \cos 2\gamma J_{sy}(\mathbf{r}') d\rho d\varphi, \tag{6.37}$$

and define

$$v = \frac{h}{\rho}, \tag{6.38}$$

the integral I_{st} becomes

$$I_{st} = \frac{1}{2\pi} \int_{\varphi_U}^{\varphi_L} \int_{\sin\varphi}^{\frac{h}{a}} \frac{\rho}{h} \cos 2\gamma J_{sy}(\mathbf{r}') dv d\varphi. \tag{6.39}$$

By further normalization of the inner integral to unit interval through the transformation

$$v = (1-\eta)\sin\varphi + \eta\frac{h}{a}, \tag{6.40}$$

the integration domain will become a rectangular domain as shown in Figure 6.4

$$I_{st} = \frac{1}{2\pi}\int_{\varphi_U}^{\varphi_L}\left(\frac{h}{a} - \sin\varphi\right)\int_0^1 \frac{\rho}{h}\cos 2\gamma J_{sy}\left(\mathbf{r}'\right)d\eta d\varphi. \tag{6.41}$$

Now standard Gauss-Legendre quadrature scheme can be used in the transverse and radial variables to accurately perform the integration. After transformation of the sampling points back to global coordinates, the integral can be evaluated as

$$I_{st}^{i}\left(x,y\right) \cong \sum_k W_k \frac{1}{2\pi\rho_k^2}\cos 2\gamma_k J_{sy}\left(\mathbf{r}'_k\right), \tag{6.42}$$

where

$$W_k = w_i w_j \frac{h}{\sin\varphi_i} f\left(\rho_{ij}\right)\ J_{sy}\left(\mathbf{r}'_{ij}\right)\rho_{ij}, \tag{6.43}$$

and we assume a double-to-single index correspondence $i,j \leftrightarrow k$ with w_i and w_j being the i-th and j-th Gauss-Legendre weights respectively.

6.4 Numerical Examples

As a numerical example, we consider a rectangular current patch on top of an interface. The top layer is air region ($\varepsilon_r = 1, \mu_r = 1, \sigma = 0$) and the bottom layer is a substrate with parameters ($\varepsilon_r = 4, \mu_r = 2, \sigma = 0$). The current flows in the y direction and its distribution is

$$J_{sy}\left(x,y\right) = \frac{1}{L}\cos\left(\frac{\pi y}{W}\right). \tag{6.44}$$

Both the length and width of the patch are 1 meter and the system is operating at 150 MHz. We take an observation loop with radius $a = 0.45$ and calculate the x-component of the magnetic field. Figure 6.9 shows the real part of H_x and Figure 6.10 shows the imaginary part. The red dotted line in both figures is the field computed using a quadrature integration rule and the black solid line is the field component calculated using the spectral-domain immittance (SDI) method [49]. The blue dotted line is the contribution from the delta function. Unlike free space, the magnetic field right on the surface contains the contribution from its image sources due to the reflection from boundary. Since the current is a real function, the delta function singularity only contributes to the real part of the magnetic field and its contribution to the imaginary part is zero as shown in Figure 6.10.

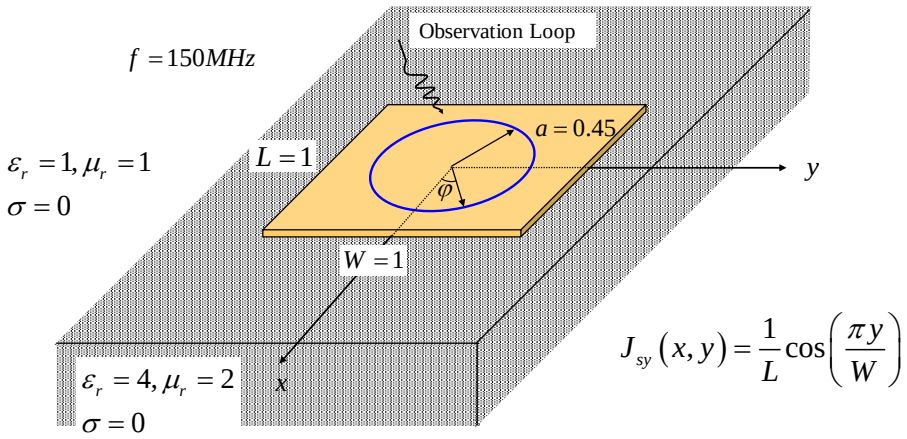

Figure 6.8. The configuration for numerical computation of H_x component due to the y-directed current patch (L = 1m, W = 1m) on the interface between two layers. The H field distribution along circle of radius of 0.45 m is sampled to compare with results obtained via SDI method

Using the SDI method, the magnetic field is related to the current through spatial

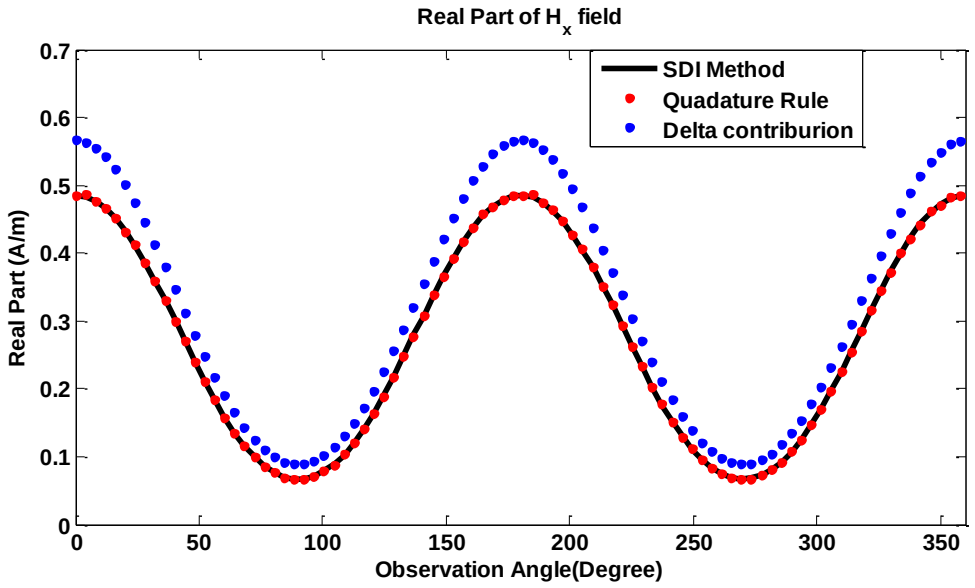

Figure 6.9. Comparison of real part of H_x component between convolution method and SDI method. The blue dot is the contribution from the delta function.

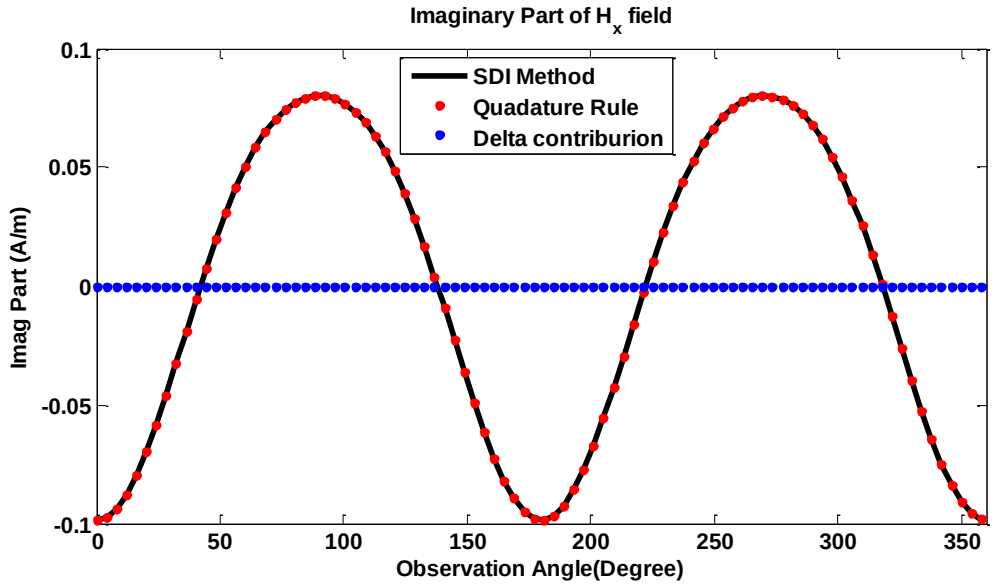

Figure 6.10. Comparison of imaginary part of H_x component between convolution method and SDI method. The blue dot is the contribution from the delta function.

Green's function as

$$\mathbf{H}(x,y,z) = \int_{-\infty}^{\infty}\int_{-\infty}^{\infty} \underline{\underline{\mathcal{G}}}^{HJ}(x-x', y-y', z, z')\ \mathbf{J}_s(x', y', z')\, dx'dy', \tag{6.45}$$

or in shorthand notation as the spatial convolution

$$\mathbf{H} = \underline{\underline{\mathcal{G}}} * \mathbf{J}_s. \tag{6.46}$$

Taking the 2D Fourier transform of both sides, the magnetic field is the multiplication of the Green's function by the current distribution in the spectral domain,

$$\tilde{\mathbf{H}} = \underline{\underline{\tilde{\mathcal{G}}}} \cdot \tilde{\mathbf{J}}_s. \tag{6.47}$$

When the current is in the y direction and the x component of magnetic field is taken into consideration, we have

$$\tilde{H}_x = \tilde{G}_{xy}^{HJ}\ \tilde{J}_{sy} \tag{6.48}$$

and

$$H_x(x,y) = \frac{1}{(2\pi)^2}\int_{-\infty}^{\infty}\int_{-\infty}^{\infty} \tilde{G}_{xy}^{HJ}\ \tilde{J}_{sy}\, e^{-jk_x x - jk_y y} dk_x dk_y, \tag{6.49}$$

where

$$\tilde{G}_{xy}^{HJ} = \left(\mu'^{-1}\cdot\tilde{\nabla}\times\underline{\underline{\tilde{G}}}^{A}\right)_{xy} = \frac{1}{2}\left(I_i^h + I_i^e\right) + \frac{1}{2}\cos 2\varphi\left(I_i^h - I_i^e\right). \tag{6.50}$$

The spectral current distribution is expressed in closed form

$$\tilde{J}_{sy}(k_x, k_y) = \frac{\pi W}{2}\left[\frac{\cos\left(k_y\frac{W}{2}\right)}{\left(\frac{\pi}{2}\right)^2 - \left(\frac{k_y W}{2}\right)^2}\right]\ \operatorname{sinc}\left(k_x\frac{L}{2}\right). \tag{6.51}$$

The SDI integral in Eq. (6.49) can be further performed in (k_ρ, ϕ) plane as

$$H_x(\rho,\theta) = \frac{1}{(2\pi)^2} \int_0^{2\pi} \int_0^{\infty} \tilde{G}_{xy}^{HJ}\, \tilde{J}_{sy}\, e^{-jk_\rho \rho \cos(\varphi-\theta)} k_\rho dk_\rho d\varphi. \tag{6.52}$$

6.5 Further Discussion

The above method only discussed the singular integrals appearing in self-term element matrix evaluation in MFIE formulation. The nearly singular interactions also need to be considered in order to further increase the accuracy of system matrix and obtain an accurate solution. Nearly singular scenarios includes cases such as two adjacent elements both sitting on the same interface as shown in the left part of Figure 6.11, and one element sitting on the interface with the other element having one edge or one vertex attached to it as shown in the right part of Figure 6.11.

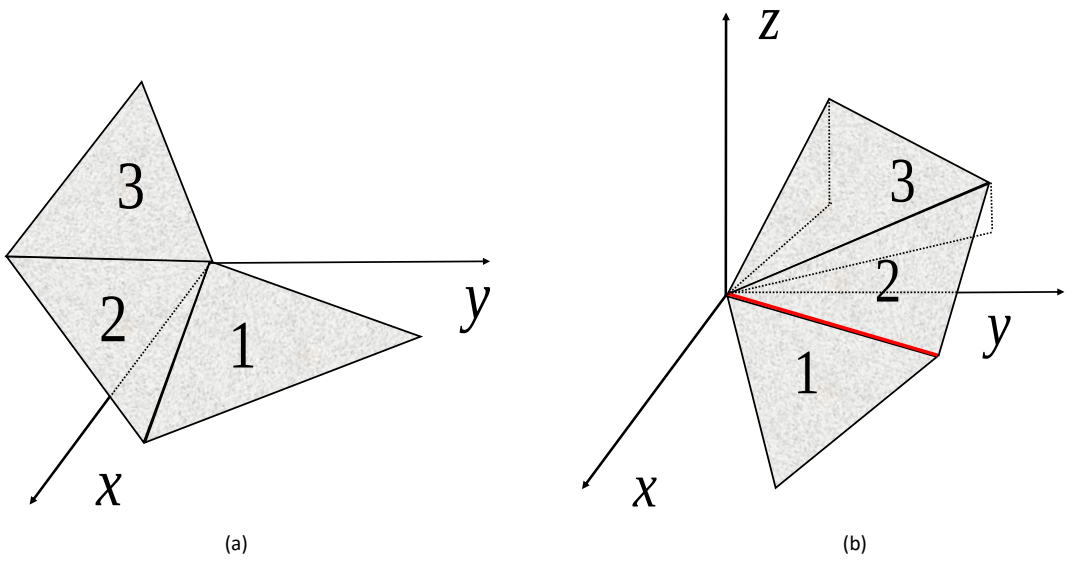

Figure 6.11. Illustration of singular and nearly singular integral scenarios: (a) both the source and testing triangles are on the interface, (b) only source triangle sits on the interface and the test triangle share a common edge or vertex with it.

Advanced numerical integration and special treatment should be applied to accurately evaluate these interactions for the following reasons:

1) For the near-singular case, the singular source behavior is rather rich and complicated if the vertical distance from the observation point to the source element is not zero. When ς is not zero, more terms will emerge in the singular kernel.

2) The singular behavior of the off-diagonal terms involving the z direction: G_{xz}^{HJ}, G_{yz}^{HJ}, G_{zx}^{HJ}, G_{zy}^{HJ} should be analyzed as well because the normal component of the source vector integral needs to be taken into consideration for near singular interactions. The corresponding independent integrals are I_{11} and I_{12}.

3) The standard quadrature scheme becomes inefficient for testing integrals because the source integral, though resulting in bounded potentials, has higher order singularities near the source domain boundaries when test and source domain boundaries overlap or coincide.

Studies of these topics has received renewed interest in computational community recently and interested readers can refer to related publication for details [87], [92], [95], [97].

Chapter 7

Applications and Results

In this chapter, we apply the algorithm developed in previous chapters to model the electromagnetic wave propagation and scattering for various problems in layered medium. This chapter is divided into three parts, each concentrating on different problems: a geophysical problem, an antenna problem and a scattering problem, respectively.

7.1 Geophyscial Prospecting Problems

As a first example, we study an induction logging simulation in a three-layered anisotropic formation [98] shown in Figure 7.1. The conductivity of the top and bottom layer is 1 S/m and the middle layer is an anisotropic medium with horizontal conductivity of 0.55 S/m and vertical conductivity of 0.18182 S/m. A triaxial induction logging tool [99] which consists of three orthogonal transmitter coils and three orthogonal receiver coils is used. The distance between transmitter and receiver is 40 inches and the operating frequency is 20.0 kHz. The deviated angle of the well trajectory is 0 degree. Figure 7.2 shows the received x-component of the magnetic field by a x-directed dipole and Figure 7.3 shows the received z-component of the magnetic field by a z-directed dipole. The y-axis logging location is at the center of the transmitter and receiver coil. The results described by blue dots is calculated using the finite difference admittance method in the reference [100]. The example used here is from the paper [101]. Since the dipole moment they defined has a ratio of $j\omega\mu$ compared to our result, we normalize our results to compare against them. Better results are observed for the Hxx component when the tool crosses the boundaries compared to theirs.

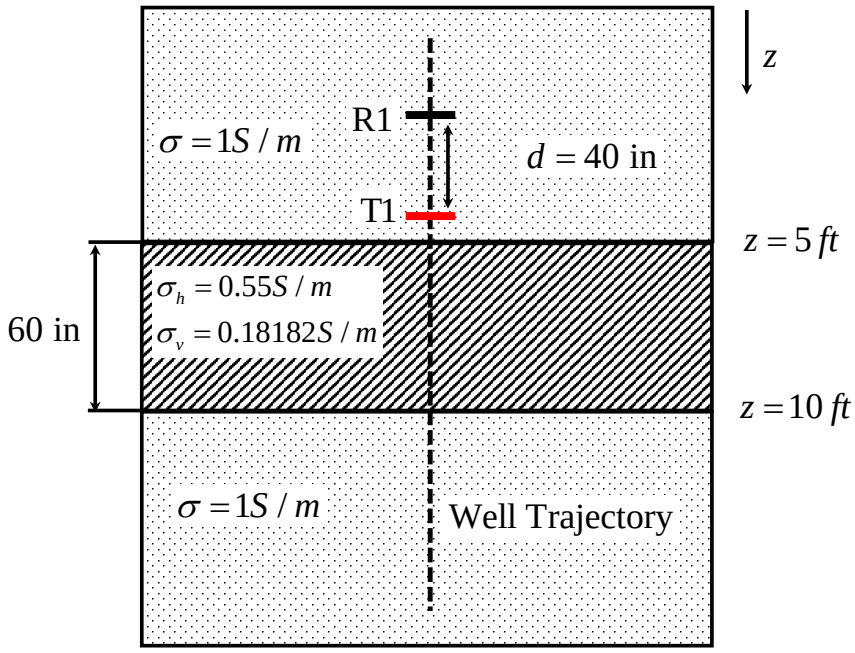

Figure 7.1. Illustration of induction logging environment in a three-layered formation.

The second example considered here is a three-layered formation shown in Figure 7.4, where the upper and bottom layer has a conductivity of 1 S/m, and the middle layer has a conductivity of 0.2 S/m. The conductivity of drilling mud (borehole fluid) is a water-based mud with a conductivity of 2 S/m. The diameter of the borehole is 10 inches and the thickness of the middle layer is 60 inches. The distance between transmitter T1 and receiver R1, receiver R1 and receiver R2 is 24 inches and 6 inches respectively.

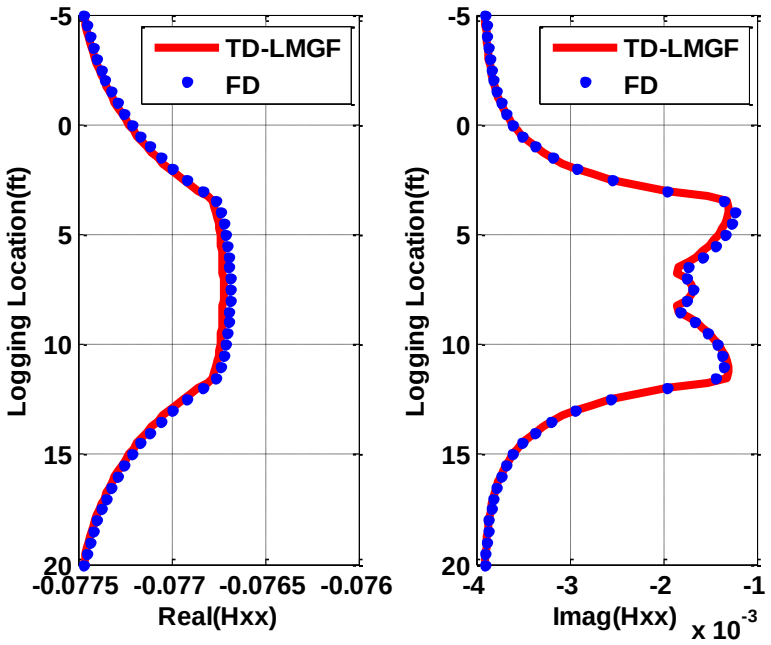

Figure 7.2. The H_x component of the magnetic field due to x-directed magnetic dipole in a three-layered formation.

The system has three operating frequencies: 400 KHz, 1 MHz and 2 MHz. In our method, the PMCHWT formulation is used to calculate the induced current on the interface of the borehole. The scattered field inside the borehole at the receiver locations are then calculated using the solved induced currents. In the PMCHWT formulation, all the mixed-potential layered medium Green's function components are used and the second-level singularity extraction is employed when we use the simplex interpolation scheme to accelerate the matrix filling. The amplitude ratio is defined as the ratio of the magnitude of the received voltages at R1 to that at R2, while the phase shift is defined as the difference of phases between R1 and R2 [102]. As we can see from Figures 7.5, 7.6 and 7.7, the amplitude ratio and phase shift increases with increasing frequency. The results from our method agree well with the results computed using a commercial solver, Maxwell2D.

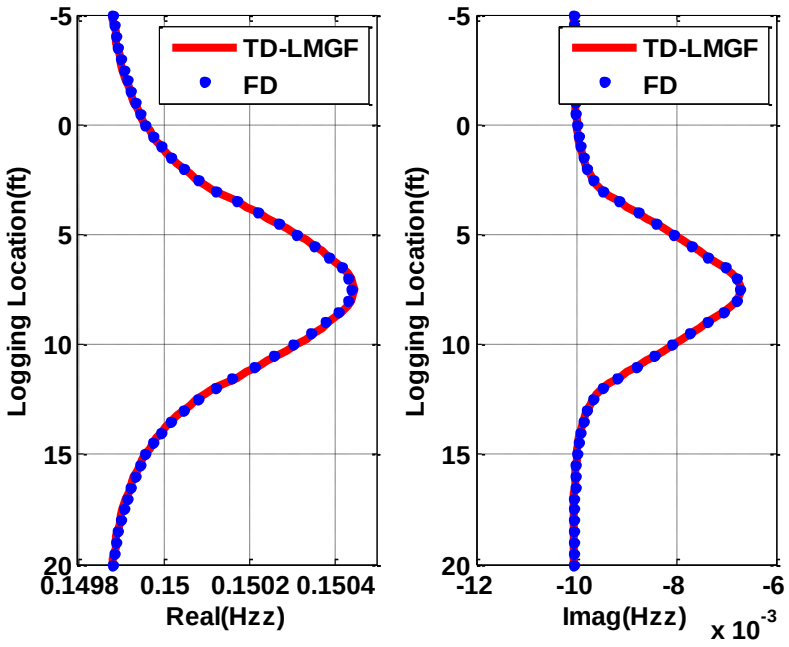

Figure 7.3. The H_z component of the magnetic field due to z-directed magnetic dipole in a three-layered formation.

7.2 Antenna Problem

As another example, we consider a cuboid sitting on the interface between two layers as shown in Figure 7.8. The length of the cube is 0.16 m and the cross section of the cube is a square with side length of 0.02 m. A voltage source with 50 Ω impedance is excited at the center of the cuboid. For layer 2 , the region is air and for layer 1, both sandy soil and sea water cases are investigated. The corresponding material property constants are listed in Table 7.1. The operating frequency is from 0.02 GHz to 1.5 GHz. We employed two kinds of meshes: a uniform mesh and an adaptive mesh as shown in Figure 7.9 and their corresponding number of triangles are 2008 and 2524 respectively. The adaptive mesh has a relatively dense mesh along the edges in order to capture their effects on input impedance. The input impedance seen from the feed and the return loss are calculated for comparison.

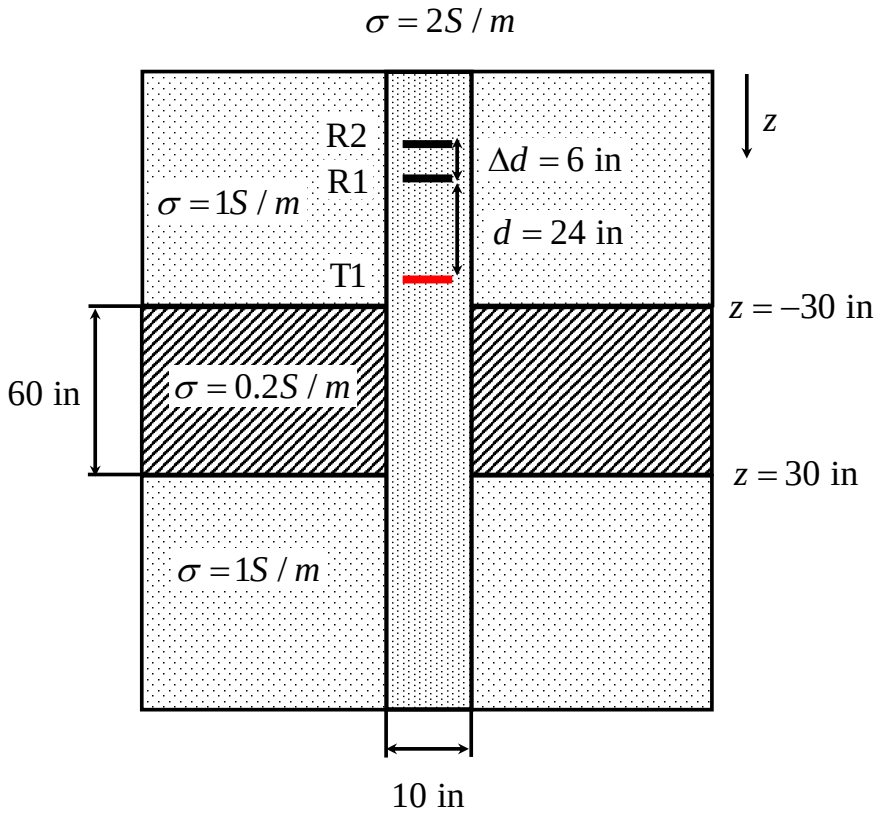

Figure 7.4. Illustration of a three-layered log-whiling-drilling environment.

Table 7.1. Material property constants

Material	Relative Permitivitty	Relative Permeability	Conductivity (S/m)
Air	1.0	1.0	0
Soil	2.53-j0.009108	1.0	0
Sea Water	74	1.0	3.53

When layer 1 is sandy soil, the input impedance and return loss are shown in Figures 7.10 and 7.11. As a comparison, we also plot the results when the antenna is in free space as shown in Figures 7.12 and 7.13. The resonant frequency of the antenna on sandy soil layer decreases due to the increase of effective permitivity. The return loss bandwidth is enlarged due to the lossy soil. When layer 1 is sea water, the

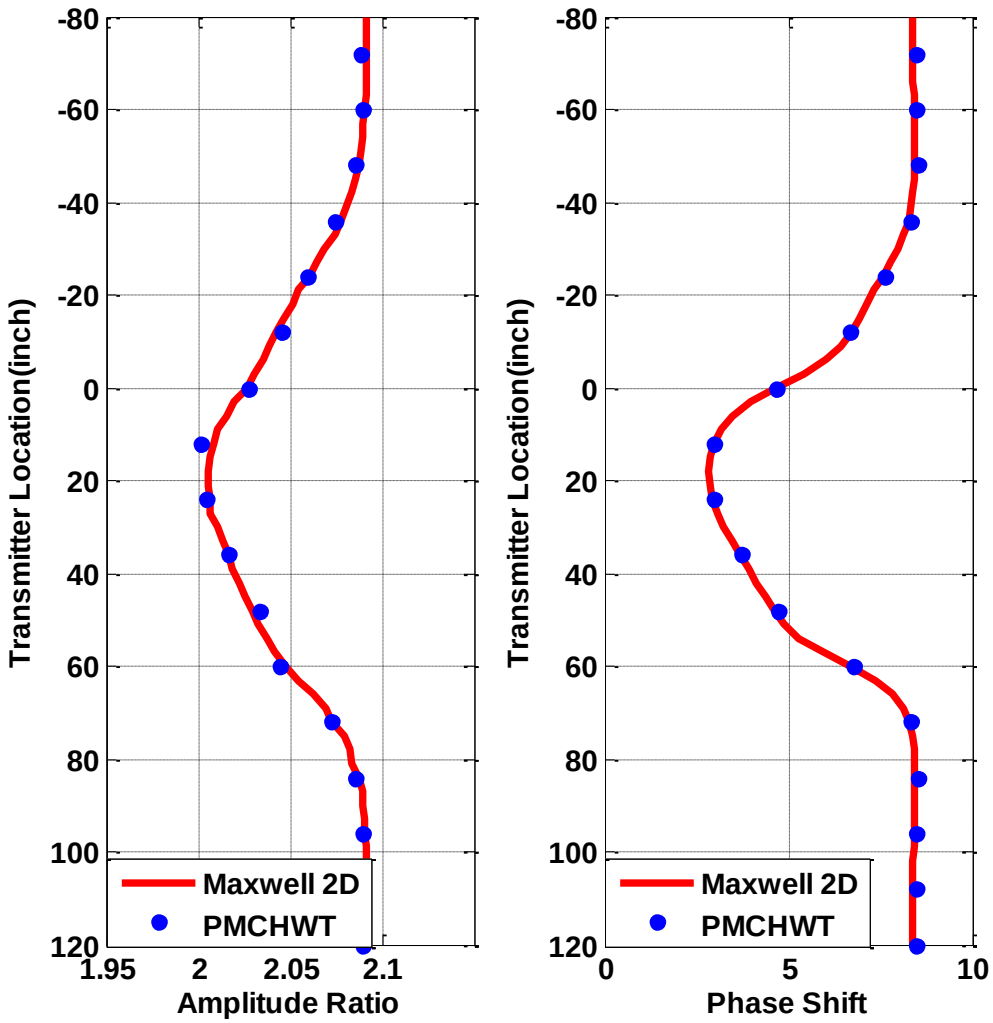

Figure 7.5. The amplitude ratio and phase difference between two receiving coils (400KHz).

input impedance and return loss are shown in Figures 7.14 and 7.15. Great influence of the input impedance and return loss by sea water is observed. In all cases, good agreement between the uniform mesh and adaptive mesh is reached.

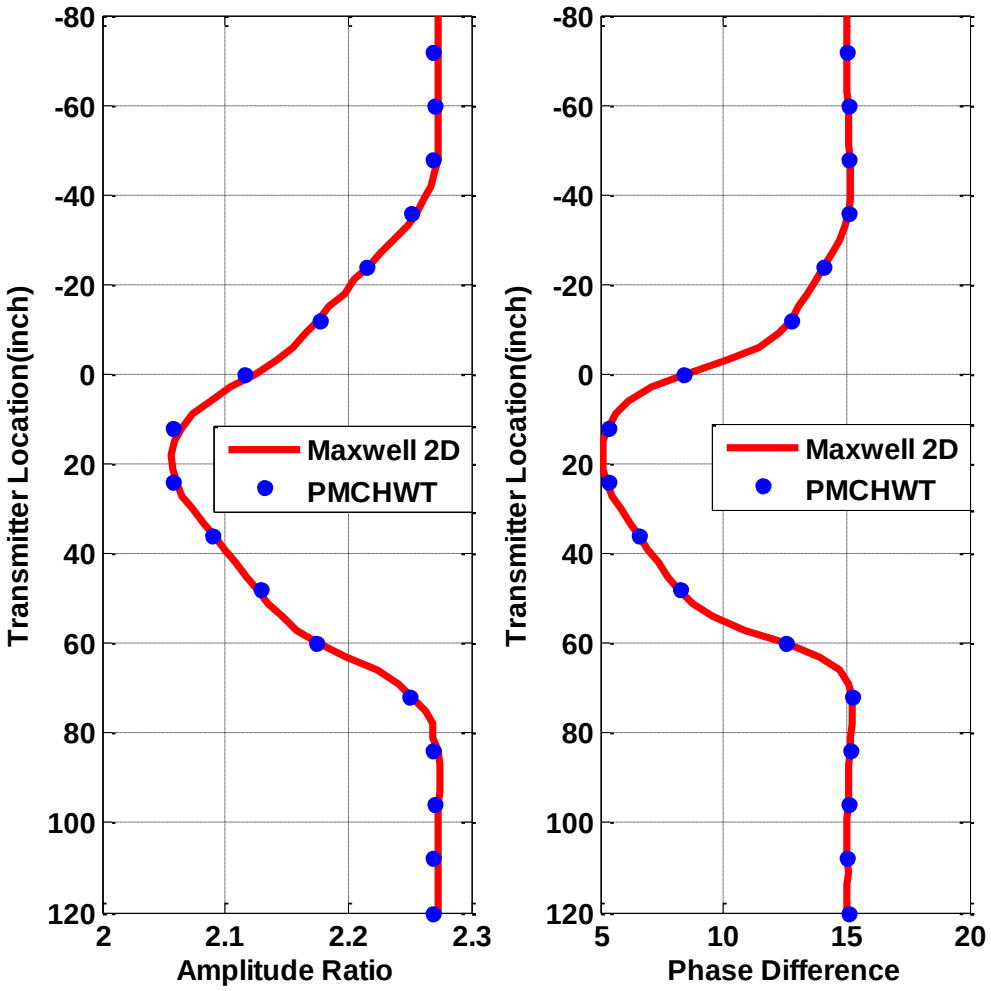

Figure 7.6. The amplitude ratio and phase difference between two receiving coils (1MHz).

7.3 Scattering Problem

The third example is a scattering problem. Consider a perfect electric conducting cube above the sandy soil. The length of the cube is 0.1 m and its centroid is located at the origin. The cubic is excited by a vertical electric dipole located 1 m to the left of the centroid as illustrated in Figure 7.16. The operating frequency is 1.5 GHz and we observe the scattered field along the observation line ($-0.5 \leq x \leq 0.5, y =$

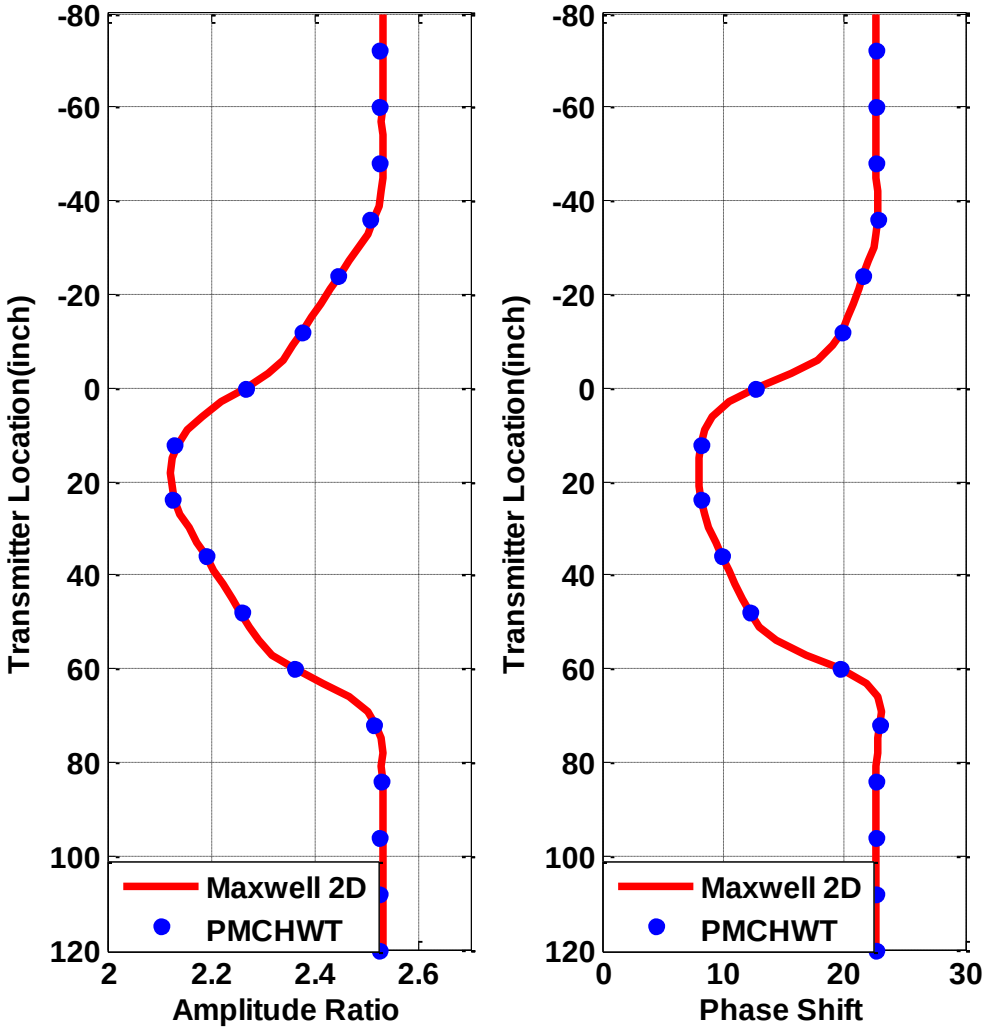

Figure 7.7. The amplitude ratio and phase difference between two receiving coils (2MHz).

$0, z = -0.09)$ m. Good agreement is observed between electric field integral equation (EFIE) and magnetic integral equation method (MFIE).

Lastly, we consider a cube sitting on the interface between the air and sandy soil. The boundary of the interface is moved to -0.05 m and the other parameters are kept the same as shown in Figure 7.19. In this case, since the bottom surface sits exactly on the interface, the MFIE formulation is corrected in order to capture the

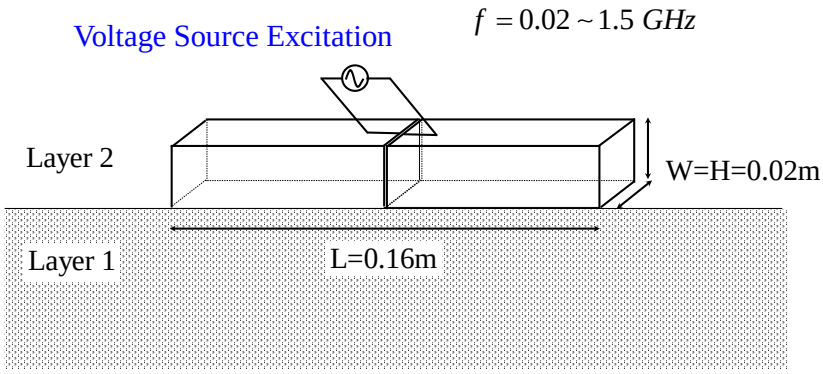

Figure 7.8. The cuboid antenna sitting on the interface of a two-layered medium.

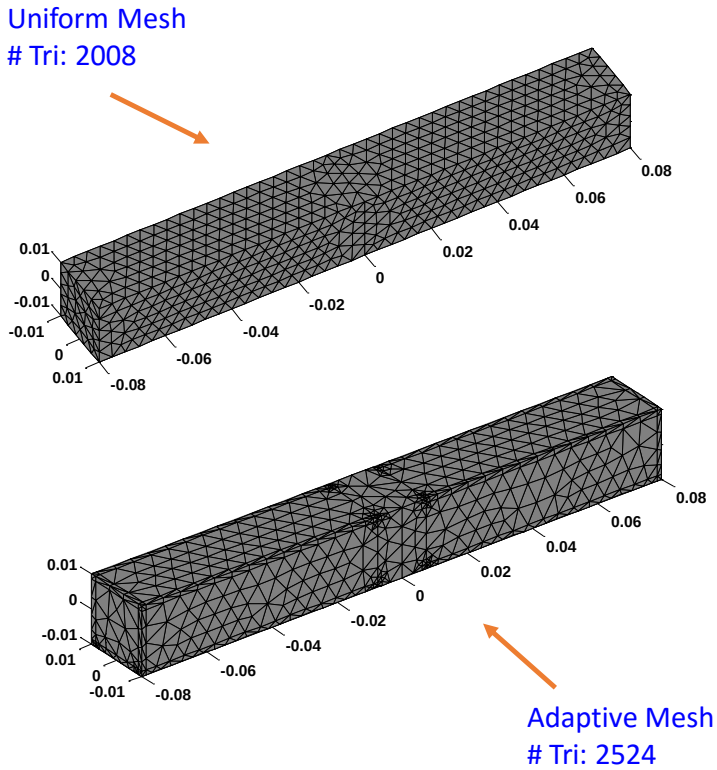

Figure 7.9. Illustration of two mesh schemes: uniform mesh (above) and adaptive mesh (below).

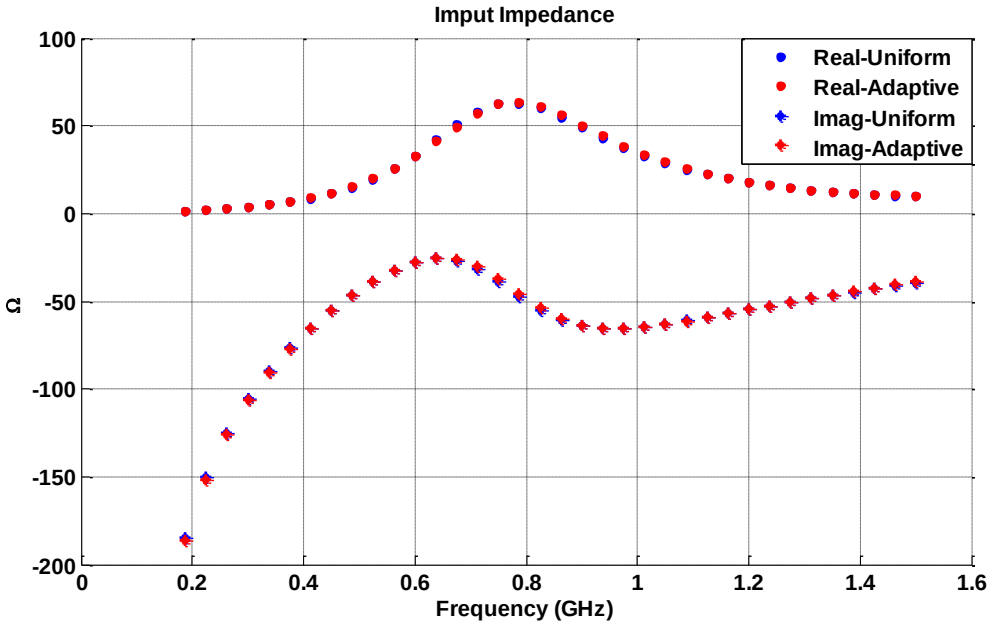

Figure 7.10. Broadband response of input impedance when the antenna is above sandy soil.

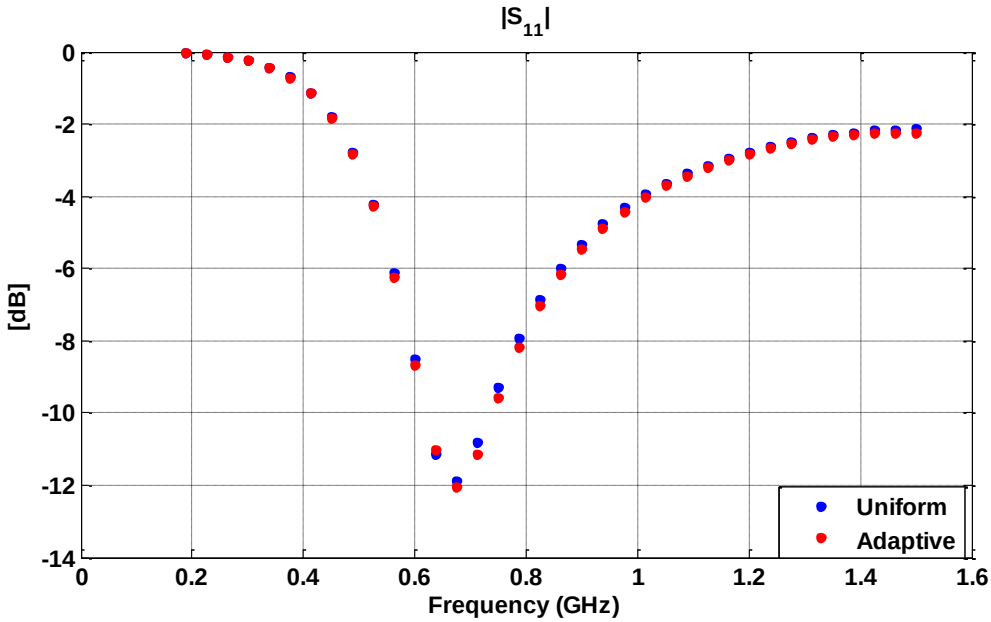

Figure 7.11. Broadband response of return loss when the antenna is above sandy soil.

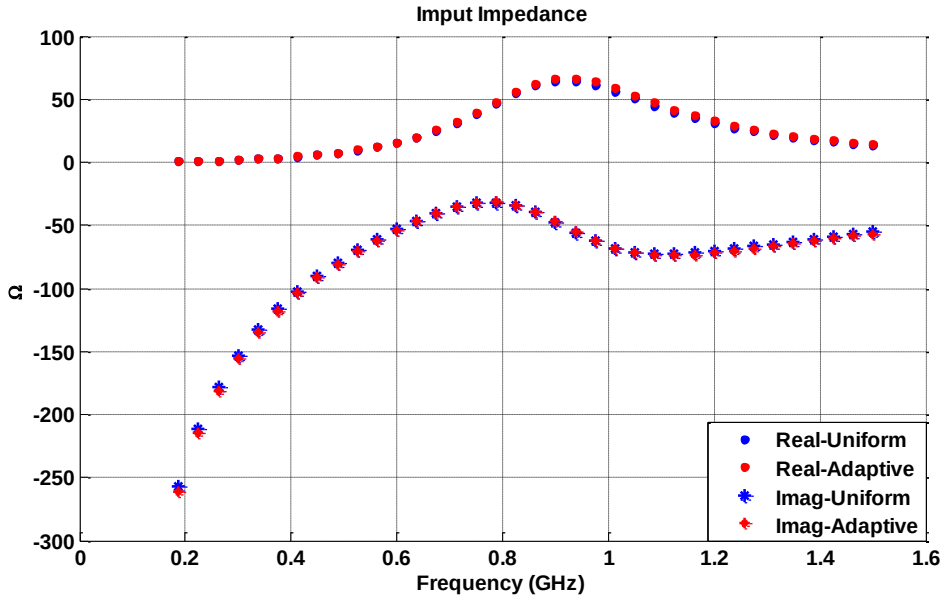

Figure 7.12. Broadband response of input impedance when the antenna is in free space.

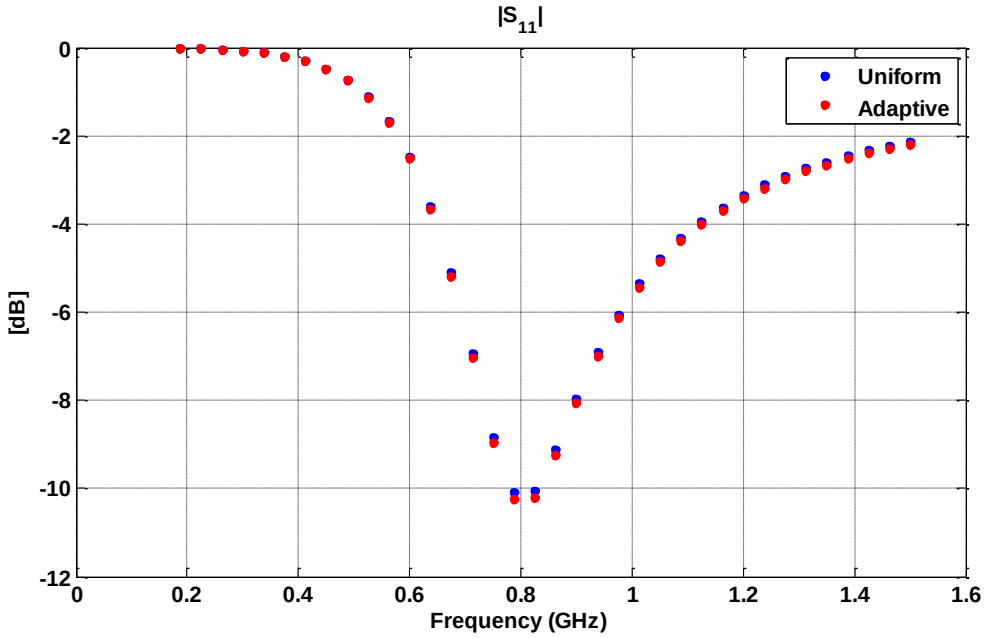

Figure 7.13. Broadband response of return loss when the antenna is in free space.

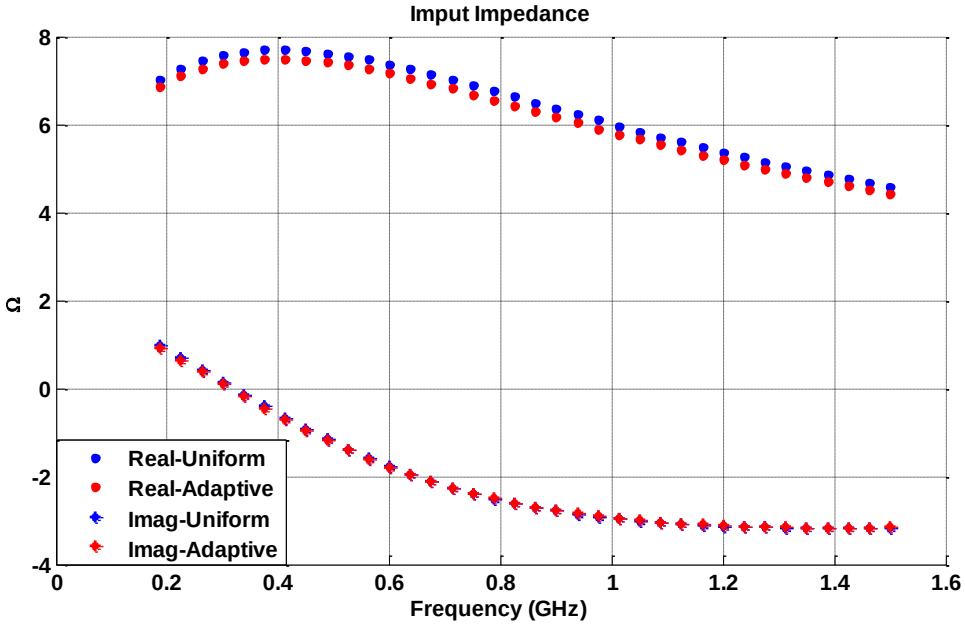

Figure 7.14. Broadband response of input impedance when the antenna is above sea water.

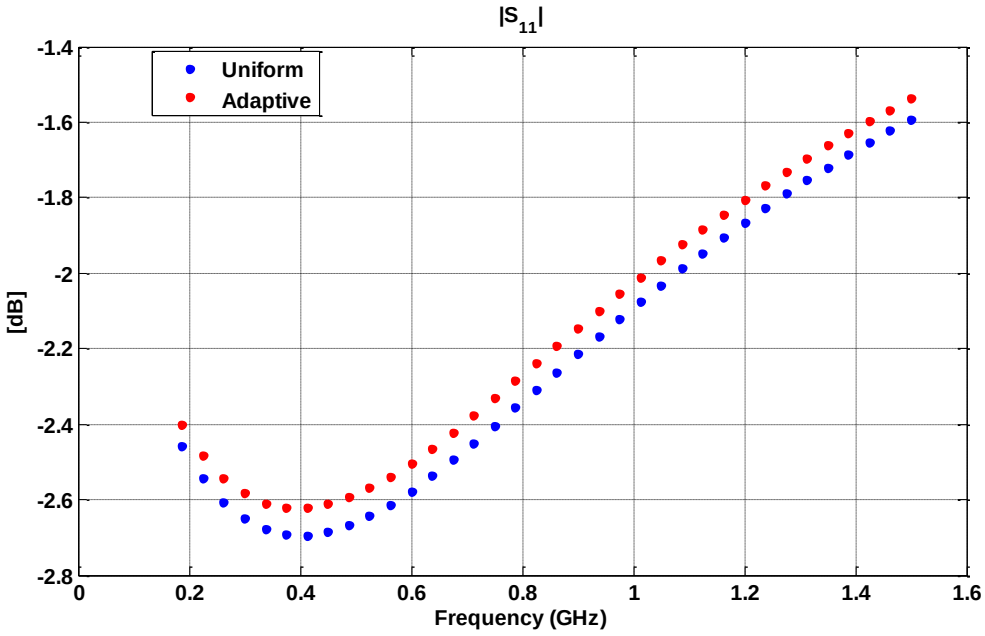

Figure 7.15. Broadband response of return loss when the antenna is above sea water.

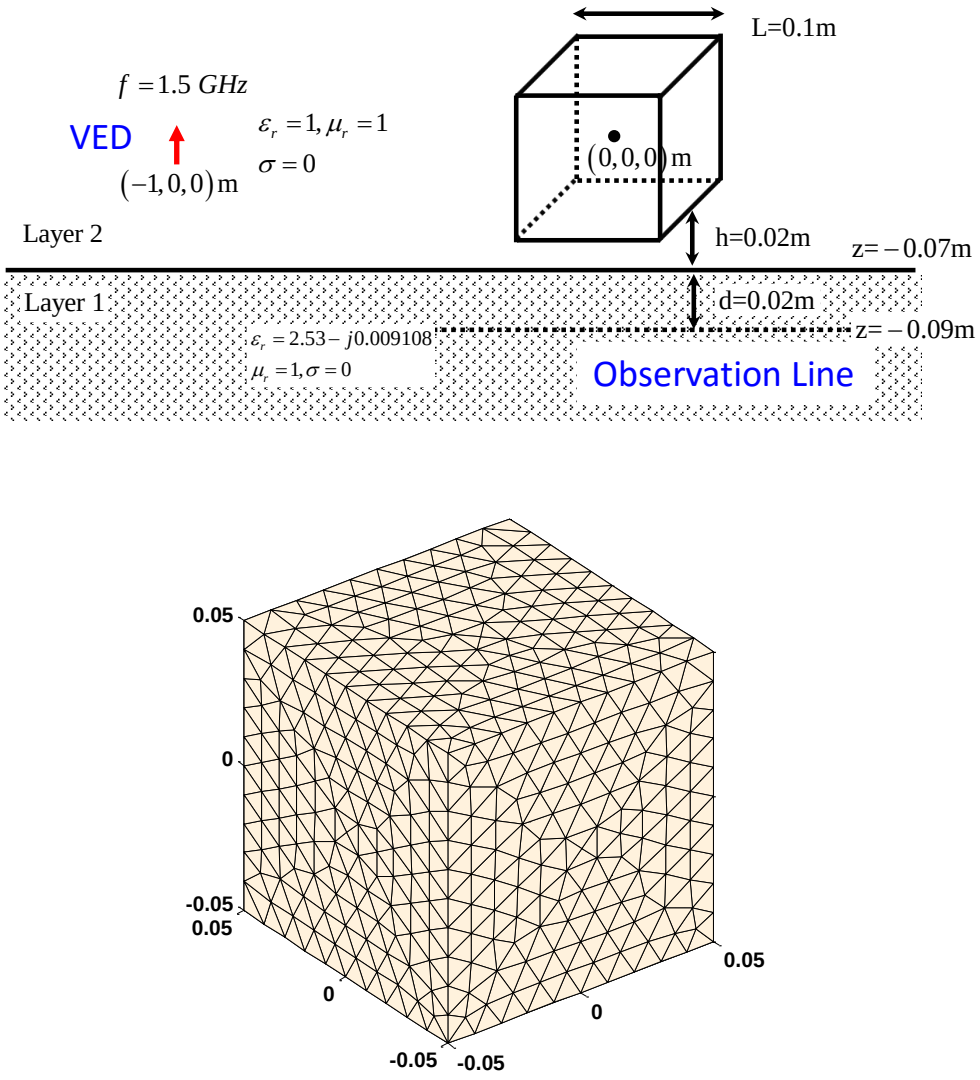

Figure 7.16. A cubic perfect electric conductor sits above the soil sand. It is excited by a vertical electric dipole. The operating frequency of the system is 1.5 GHz (Above). Uniform mesh view of the cube (triangle edge length ≈ 0.01 m)(Below)

delta singularity rising from reflection.

$$\frac{1}{2}\left(1+\frac{\overleftarrow{\Gamma}^{e,\infty}+\overleftarrow{\Gamma}^{h,\infty}}{2}\right)\mathbf{J}^{\mathbf{s}}-\hat{n}\times\int\limits_{p.v}\nabla\times\underline{\underline{\mathcal{G}}}\left(\mathbf{r},\mathbf{r}'\right)\cdot\mathbf{J}^{\mathbf{s}}ds'=\hat{n}\times\mathbf{H}^{i}_{\tan},\underline{r}\uparrow S \quad (7.1)$$

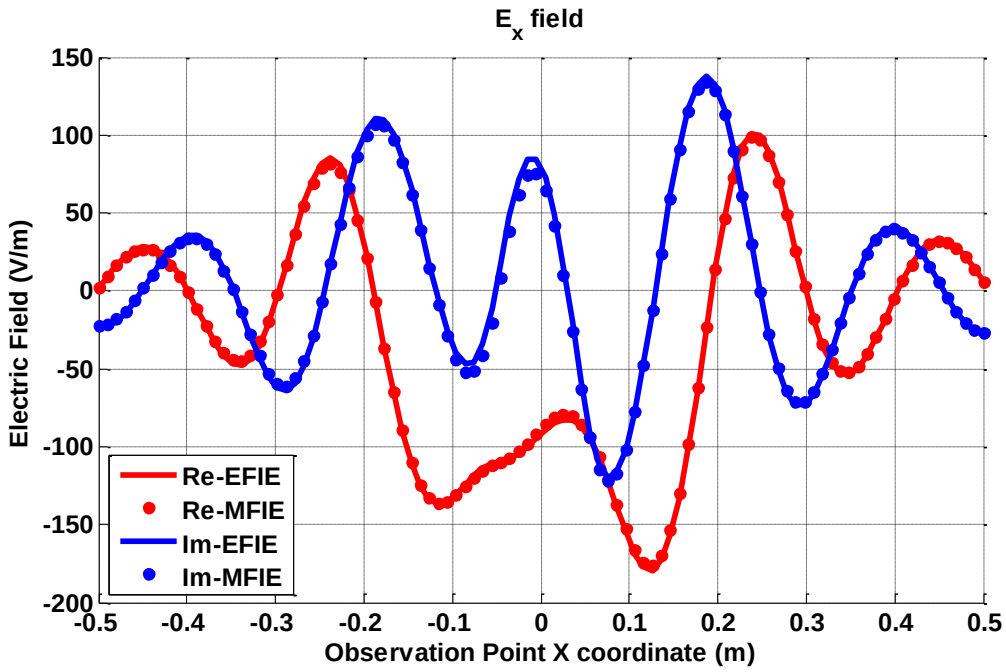

Figure 7.17. Comparison of x-component of scattered electric field along the observation line between EFIE and MFIE when the cube is above sandy soil.

Again the x component and z component of the scattered electric field is calculated for comparison in Figure 7.20 and Figure 7.21. The solid line is the results calculated using EFIE and the solid dots are the results calculated using the MFIE without any special treatment. The circles denote the results calculated using the corrected MFIE. The last formulation takes into account the delta contribution from reflections for self-term interactions when the triangular element sits on an interface. The result obtained via EFIE can be viewed as a reference value and we can see the corrected MFIE gives a better agreement around the peak value of the results.

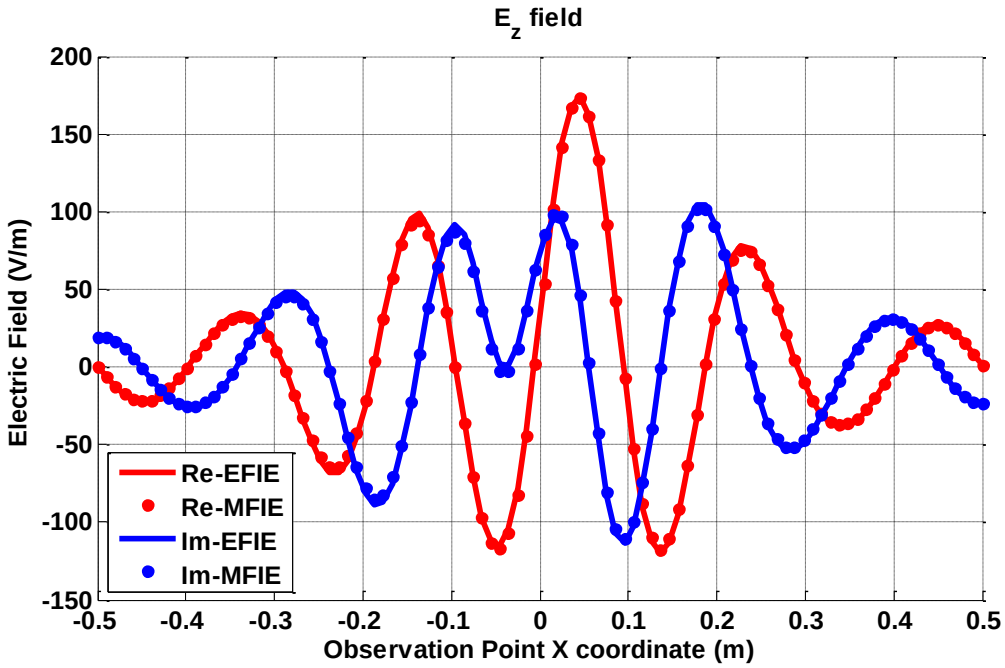

Figure 7.18. Comparison of z-component of scattered electric field along the observation line between EFIE and MFIE when the cube is above sandy soil.

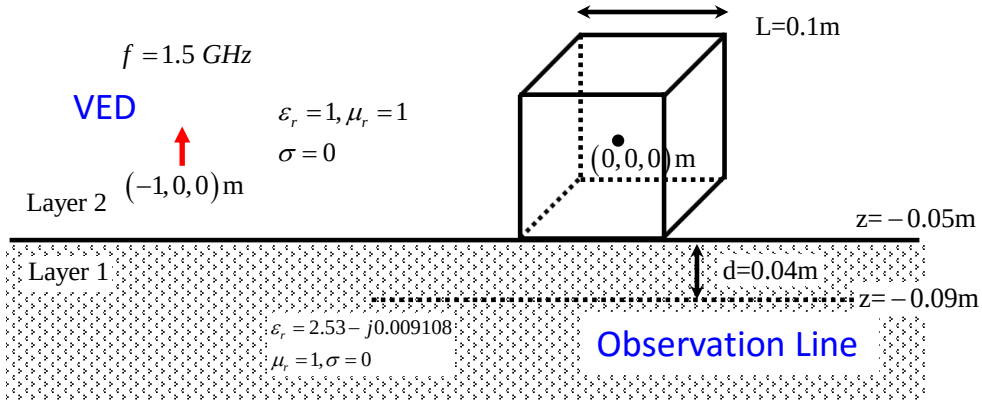

Figure 7.19. The cube sits on the interface between air and sandy soil.

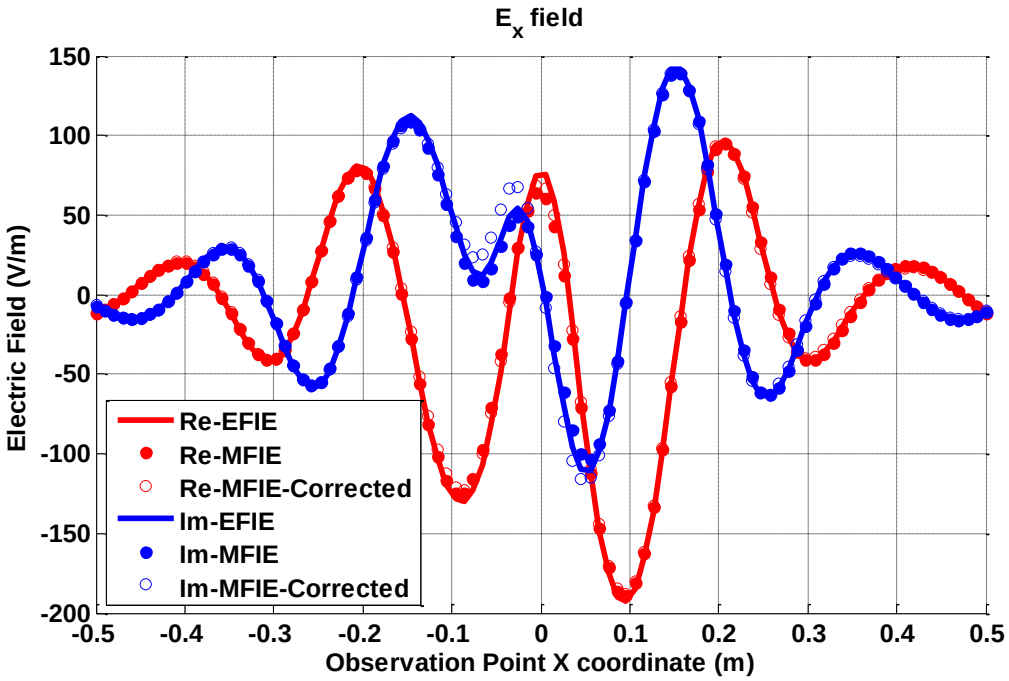

Figure 7.20. Comparison of x-component of scattered electric field along the observation line between EFIE, traditional MFIE and corrected MFIE when the cubic sits on the interface between air and sandy soil.

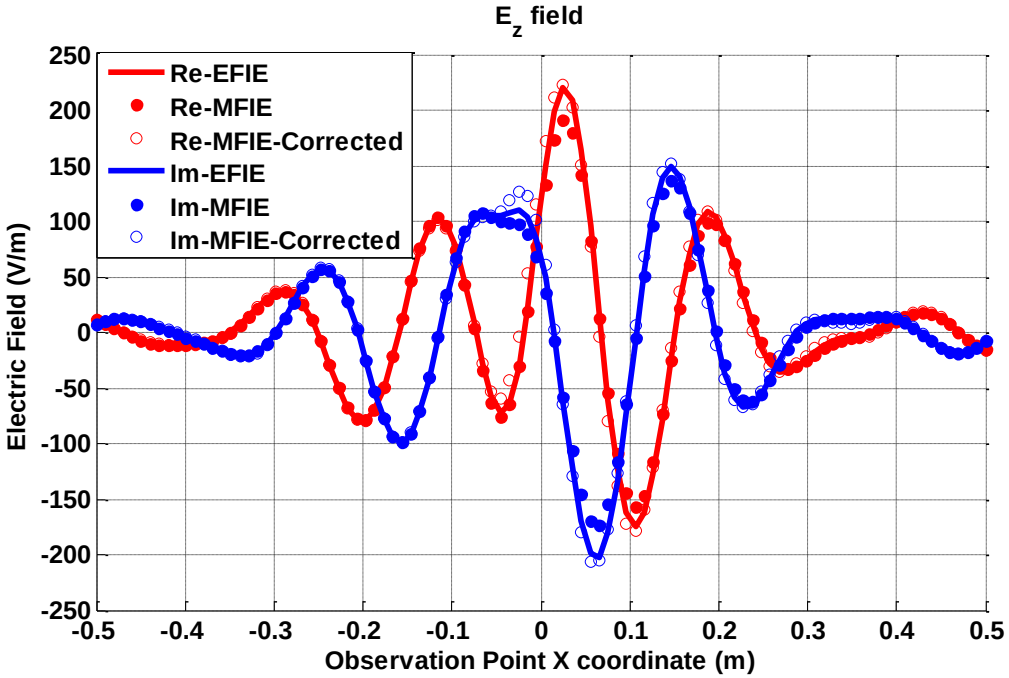

Figure 7.21. Comparison of z-component of scattered electric field along the observation line between EFIE, traditional MFIE and corrected MFIE when the cubic sits on the interface between air and sandy soil.

Chapter 8

Conclusion and Future Work

8.1 Conclusion

In this dissertation, the traditional, mix-potential LMGFs and their gradients are discussed and developed using various techniques, namely asymptotic subtraction and singularity extraction, weighted average method and simplex interpolation. Based on them, a few fast and efficient algorithms are arrived at to compute the electromagnetic wave propagation and interaction with complex scatters in multi-layered media.

In order to study wave propagation in uniaxial anisotropic media in our model, a number of Sommerfeld and related identities are extended to uniaxial anisotropic media with the introduction of ratios of horizontal to vertical medium parameters. For lossy media, the effective distances between source and observation points appearing in the spatial-domain forms become complex quantities involving the anisotropy ratios depending on TE or TM polarization. Moreover, half-line source potential definitions and methods for evaluating them are also extended to the complex domain through analytic continuation.

The second-level of asymptotic extraction is developed with two purposes: (1) After removing all unbounded singularities for curl-type operators, the spectral-domain integral terms can be further regularized to permit interpolation using a uniform tabulation density, and (2) The second-level of singularity extraction can be used to study the singular behavior of curl-type operators in the MFIE formulation.

Three types of problem, geophysical prospecting, antenna and radiation problems, are employed to demonstrate the efficiency of the algorithms and wide-range of applications for which our algorithms can be applied.

8.2 Future Work

8.2.1 Multiple Thin/High Contrast Layers

Numerical difficulties might exist for some extreme cases such as the computation of LMGFs in thin stratified multi-layered media and layers with extremely high contrasts between adjacent layer parameters. In the first case, the convergence acceleration may not be achieved significantly since the layers are too thin to have the transmission quantities and integrands in SIs decay fast enough, while in the latter case, when the source and observation points are in adjacent layers, the asymptotic representations might not be accurate enough until we reach extremely high spectral values.

8.2.2 Steepest Decent Path Method

When the distance between source and observation points gets further away from each other, the integrand containing the Bessel function oscillates faster and faster. As a result, denser sampling points are needed to reach convergence, thus the efficiency of our algorithm may be decreased correspondingly. Alternative methods, such as the famous steepest descent path method (SDP), may be used to achieve high efficiency.

8.2.3 Near Singular Integrals

When MFIE in layered medium is used, due to the rich and complicated forms of the singular kernel appearing in the curl-type operator, advanced numerical techniques are needed to evaluate the singular and nearly singular integrals accurately and efficiently.

References

[1] K. A. Michalski and J. R. Mosig, "Multilayered media Green's functions in integral equation formulations," *IEEE Transactions on Antennas and Propagation*, vol. 45, no. 3, pp. 508–519, 1997.

[2] N. K. Das and D. M. Pozar, "A generalized spectral-domain Green's function for multilayer dielectric substrates with application to multilayer transmission lines," *IEEE Transactions on Microwave Theory and Techniques*, vol. 35, no. 3, pp. 326–335, 1987.

[3] J.-S. Zhao, W. C. Chew, C.-C. Lu, E. Michielssen, and J. Song, "Thin-stratified medium fast-multipole algorithm for solving microstrip structures," *IEEE Transactions on Microwave Theory and Techniques*, vol. 46, no. 4, pp. 395–403, 1998.

[4] Z. Sipus, P.-S. Kildal, R. Leijon, and M. Johansson, "An algorithm for calculating Green's functions of planar, circular cylindrical, and spherical multilayer substrates," *Applied Computational Electromagnetics Society Journal*, vol. 13, pp. 243–254, 1998.

[5] P. E. Wannamaker, G. W. Hohmann, and W. A. SanFilipo, "Electromagnetic modeling of three-dimensional bodies in layered earths using integral equations," *Geophysics*, vol. 49, no. 1, pp. 60–74, 1984.

[6] R. H. Hardman and L. C. Shen, "Theory of induction sonde in dipping beds," *Geophysics*, vol. 51, no. 3, pp. 800–809, 1986.

[7] S. Ali and S. Mahmoud, "Electromagnetic fields of buried sources in stratified anisotropic media," *IEEE Transactions on Antennas and Propagation*, vol. 27, no. 5, pp. 671–678, 1979.

[8] T. M. Habashy, S. M. AIi, J. A. Kong, and M. D. Grossi, "Dyadic Green's functions in a planar stratified, arbitrarily magnetized linear plasma," *Radio Science*, vol. 26, no. 3, pp. 701–715, 1991.

[9] K. A. Michalski, "Mixed-potential integral equation (MPIE) formulation for nonplanar microstrip structures of arbitrary shape in multilayered uniaxial media (invited article)," *International Journal of Microwave and Millimeter-Wave Computer-Aided Engineering*, vol. 3, no. 4, pp. 420–431, 1993.

[10] N. G. Alexopoulos, "Integrated-circuit structures on anisotropic substrates," *IEEE Transactions on Microwave Theory and Techniques*, vol. 33, no. 10, pp. 847–881, 1985.

[11] J. A. Kong, "Electromagnetic fields due to dipole antennas over stratified anisotropic media," *Geophysics*, vol. 37, no. 6, pp. 985–996, 1972.

[12] L. Tsang, C.-J. Ong, C.-C. Huang, and V. Jandhyala, "Evaluation of the Green's function for the mixed potential integral equation (MPIE) method in the time domain for layered media," *IEEE Transactions on Antennas and Propagation*, vol. 51, no. 7, pp. 1559–1571, 2003.

[13] C.-J. Ong, B. Wu, L. Tsang, and X. Gu, "Full-wave solver for microstrip trace and through-hole via in layered media," *IEEE Transactions on Advanced Packaging*, vol. 31, no. 2, pp. 292–302, 2008.

[14] B. Wu and L. Tsang, "Signal integrity analysis of package and printed circuit board with multiple vias in substrate of layered dielectrics," *IEEE Transactions on Advanced Packaging*, vol. 33, no. 2, pp. 510–516, 2010.

[15] C. T. Tai, "Dyadic Green's functions in electromagnetic theory," IEEE Press Series on Electromagnetic Waves, 1994.

[16] T. M. Habashy and A. Abubakar, "A general framework for constraint minimization for the inversion of electromagnetic measurements," *Progress In Electromagnetics Research*, vol. 46, pp. 265–312, 2004.

[17] M. S. Zhdanov, "Chapter 5 - electromagnetic fields in horizontally stratified media," in, ser. Methods in Geochemistry and Geophysics, M. S. Zhdanov, Ed., vol. 43, Elsevier, 2009, pp. 153 –231.

[18] Y. L. Chow, J. J. Yang, D. G. Fang and G. E. Howard, "A closed-form spatial Green's function for the thick microstrip substrate," *IEEE Transactions on Microwave Theory and Techniques*, vol. 39, no. 3, pp. 588–592, 1991.

[19] F. Ling and J.-M. Jin, "Discrete complex image method for Green's functions of general multilayer media," *IEEE Microwave and Guided Wave Letters*, vol. 10, no. 10, pp. 400–402, 2000.

[20] A. Alparslan, M. I. Aksun, and K. A. Michalski, "Closed-form Green's functions in planar layered media for all ranges and materials," *IEEE Transactions on Microwave Theory and Techniques*, vol. 58, no. 3, pp. 602–613, 2010.

[21] M. Yuan, T. K. Sarkar, and M. Salazar-Palma, "A direct discrete complex image method from the closed-form Green's functions in multilayered media," *IEEE Transactions on Microwave Theory and Techniques*, vol. 54, no. 3, pp. 1025–1032, 2006.

[22] V. N. Kourkoulos and A. C. Cangellaris, "Accurate approximation of Green's functions in planar stratified media in terms of a finite sum of spherical and cylindrical waves," *IEEE Transactions on Antennas and Propagation*, vol. 54, no. 5, pp. 1568–1576, 2006.

[23] E. Karabulut, A. T. Erdogan, and M. Aksun, "Discrete complex image method with spatial error criterion," *IEEE Transactions on Microwave Theory and Techniques*, vol. 59, no. 4, pp. 793–802, 2011.

[24] Y. P. Chen, W. C. Chew, and L. Jiang, "A novel implementation of discrete complex image method for layered medium Green's function," *Antennas and Wireless Propagation Letters, IEEE*, vol. 10, pp. 419–422, 2011.

[25] T.J.Cui and W.C.Chew, "Efficient evaluation of Sommerfeld integrals for tm wave scattering by buried objects," *Journal of Electromagnetic Waves and Applications*, vol. 12, no. 5, pp. 607–657, 1998.

[26] T. J. Cui and W. C. Chew, "Fast evaluation of sommerfeld integrals for EM scattering and radiation by three-dimensional buried objects," *IEEE Transactions on Geoscience and Remote Sensing*, vol. 37, no. 2, pp. 887–900, 1999.

[27] B. Hu and W. C. Chew, "Fast inhomogeneous plane wave algorithm for scattering from objects above the multilayered medium," *IEEE Transactions on Geoscience and Remote Sensing*, vol. 39, no. 5, pp. 1028–1038, 2001, ISSN: 0196-2892.

[28] B. Wu and L. Tsang, "Fast computation of layered medium Green's functions of multilayers and lossy media using fast all-modes method and numerical modified steepest descent path method," *IEEE Transactions on Microwave Theory and Techniques*, vol. 56, no. 6, pp. 1446–1454, 2008.

[29] W. C. Chew and Q. H. Liu, "Inversion of induction tool measurements using the distorted Born iterative method and cg-ffht," *IEEE Transactions on Geoscience and Remote Sensing*, vol. 32, no. 4, pp. 878–884, 1994, ISSN: 0196-2892.

[30] J. L. W. Li, P. P. Ding, S. Zouhdi, and S. P. Yeo, "An accurate and efficient evaluation of planar multilayered Green's functions using modified fast Hankel transform method," *IEEE Transactions on Microwave Theory and Techniques*, vol. 59, no. 11, pp. 2798–2807, 2011, ISSN: 0018-9480.

[31] P. P. Ding, C. W. Qiu, S. Zouhdi, and S. P. Yeo, "Rigorous derivation and fast solution of spatial-domain Green's functions for uniaxial anisotropic multilayers using modified fast Hankel transform method," *IEEE Transactions on Microwave Theory and Techniques*, vol. 60, no. 2, pp. 205–217, 2012, ISSN: 0018-9480.

[32] G. Valerio, S. Paulotto, P. Baccarelli, D. R. Jackson, D. R. Wilton, W. A. Johnson, and A. Galli, "Efficient computation of 1-d periodic layered mixed potentials for the analysis of leaky-wave antennas with vertical elements," *IEEE Transactions on Antennas and Propagation*, vol. 63, no. 6, pp. 2396–2411, 2015.

[33] E Simssek, Q. H. Liu, and B. Wei, "Singularity subtraction for evaluation of Green's functions for multilayer media," *IEEE Transactions on Microwave Theory and Techniques*, vol. 54, no. 1, pp. 216–224, 2006.

[34] K. Michalski, "Extrapolation methods for Sommerfeld integral tails," *IEEE Transactions on Antennas and Propagation*, vol. 46, no. 10, pp. 1405–1418, 1998.

[35] J. Mosig, "The weighted averages algorithm revisited," *IEEE Transactions on Antennas and Propagation*, vol. 60, no. 4, pp. 2011–2018, 2012.

[36] R. Golubovic, A. G. Polimeridis, and J. R. Mosig, "Efficient algorithms for computing Sommerfeld integral tails," *IEEE Transactions on Antennas and Propagation*, vol. 60, no. 5, pp. 2409–2417, 2012.

[37] J. Chen, A. A. Kishk, and A. W. Glisson, "A 3d interpolation model for the calculation of the Sommerfeld integrals to analyze dielectric resonators in a multilayered medium," *Electromagnetics*, vol. 20, no. 1, pp. 1–15, 2000.

[38] M. A. Francavilla, D. R. Wilton, S Paulotto, and D. R. Jackson, "3-simplex interpolation of the mixed-potential Green's functions in layered media," *Eu-*

ropean conference on Antennas and Propagation (EuCAP), pp. 2864–2868, 2011.

[39] P. R. Atkins, "Fast computation of the dyadic Green's function for layered media via interpolation," *IEEE Antennas and Wireless Propagation Letters*, vol. 9, no. 6, pp. 493–496, 2010.

[40] F. T. Celepcikay, D. R. Wilton, D. R. Jackson, S. Paulotto, and W. a. Johnson, "Efficient evaluation of half-line source potentials and their derivatives," *IEEE Transactions on Antennas and Propagation*, vol. 60, no. 12, pp. 5834–5842, 2012.

[41] J. M. Jin and V. V. Liepa, "Application of hybrid finite element method to electromagnetic scattering from coated cylinders," *IEEE Transactions on Antennas and Propagation*, vol. 36, no. 1, pp. 50–54, 1988.

[42] X.-Q. Sheng, J.-M. Jin, J. Song, C.-C. Lu, and W. C. Chew, "On the formulation of hybrid finite-element and boundary-integral methods for 3-d scattering," *IEEE Transactions on Antennas and Propagation*, vol. 46, no. 3, pp. 303–311, 1998.

[43] J. Liu and J.-M. Jin, "A novel hybridization of higher order finite element and boundary integral methods for electromagnetic scattering and radiation problems," *IEEE Transactions on Antennas and Propagation*, vol. 49, no. 12, pp. 1794–1806, 2001.

[44] T. F. Eibert and V. Hansen, "3-D FEM/BEM-hybrid approach based on a general formulation of Huygens' principle for planar layered media," *IEEE Transactions on Microwave Theory and Techniques*, vol. 45, no. 7, pp. 1105–1112, 1997.

[45] K. A. Michalski and A. A. Kucharski, "On the surface limit in the boundary integral equations of electromagnetics," *IEEE Transactions on Antennas and Propagation*, vol. 62, no. 1, pp. 257–263, 2014.

[46] H. Doll, "Introduction to induction logging and application to logging of wells drilled with oil base mud," *Journal of Petroleum Technology*, vol. 1, no. 06, pp. 148–162, 1949, ISSN: 0149-2136.

[47] J. Moran and K. Kunz, "Basic theory of induction logging and application to study of two-coil sondes," *Geophysics*, vol. 27, no. 6, pp. 829–858, 1962.

[48] J. A. Kong, "Theory of electromagnetic waves," *New York, Wiley-Interscience, 1975. 348 p.*, vol. 1, 1975.

[49] D. M. Pozar, "Radiation and scattering from a microstrip patch on a uniaxial substrate," *IEEE Transactions on Antennas and Propagation*, vol. 35, no. 6, pp. 613–621, 1987.

[50] K.-L. Wong and H.-T. Chen, "Electromagnetic scattering by a uniaxially anisotropic sphere," in *Microwaves, Antennas and Propagation, IEE Proceedings H*, IET, vol. 139, 1992, pp. 314–318.

[51] V. Losada, R. R. Boix, and M. Horno, "Full-wave analysis of circular microstrip resonators in multilayered media containing uniaxial anisotropic dielectrics, magnetized ferrites, and chiral materials," *IEEE Transactions on Microwave Theory and Techniques*, vol. 48, no. 6, pp. 1057–1064, 2000.

[52] W. C. Chew, "Waves and fields in inhomogenous media," *2nd Edition, Wiley-IEEE Press*, 1995.

[53] L. B. Felsen and N. Marcuvitz, "Radiation and scattering of waves," *John Wiley & Sons*, vol. 31, 1994.

[54] C.-I. Hsu, R. F. Harrington, J. R. Mautz, and T. Sarkar, "On the location of leaky wave poles for a grounded dielectric slab," *IEEE Transactions on Microwave Theory and Techniques*, vol. 39, no. 2, pp. 346–349, 1991.

[55] R. E. Collin, "Hertzian dipole radiating over a lossy earth or sea: Some early and late 20th-century controversies," *Antennas and Propagation Magazine, IEEE*, vol. 46, no. 2, pp. 64–79, 2004.

[56] D. R. Jackson and A. A. Oliner, "A leaky-wave analysis of the high-gain printed antenna configuration," *IEEE Transactions on Antennas and Propagation*, vol. 36, no. 7, pp. 905–910, 1988.

[57] C. I. G. Hsu, R. F. Harrington, J. R. Mautz, and T. K. Sarkar, "On the location of leaky wave poles for a grounded dielectric slab," *IEEE Transactions on Microwave Theory and Techniques*, vol. 39, no. 2, pp. 346–349, 1991.

[58] G Dural and M. I. Aksun, "Closed-form Green's functions for general sources and stratified media," *IEEE Transactions on Microwave Theory and Techniques*, vol. 43, no. 7, pp. 1545–1552, 1995.

[59] Y. P. Chen, W. C. Chew, and L. Jiang, "A new Green's function formulation for modeling homogeneous objects in layered medium," *IEEE Transactions on Antennas and Propagation*, vol. 60, no. 10, pp. 4766–4776, 2012.

[60] K. Michalski and D. Zheng, "Electromagnetic scattering and radiation by surfaces of arbitrary shape in layered media. i. theory," *IEEE Transactions on Antennas and Propagation*, vol. 38, no. 3, pp. 335–344, 1990.

[61] M. Abramowitz, I. A. Stegun, *et al.*, "Handbook of mathematical functions," *Applied mathematics series*, vol. 55, p. 62, 1966.

[62] A. Taflove and S. C. Hagness, "Computational electrodynamics: The finite-difference time-domain method," *Norwood, 2nd Edition, MA: Artech House*, 1995.

[63] J.-M. Jin, "The finite element method in electromagnetics," *3nd Edition, John Wiley & Sons*, 2014.

[64] R. F. Harrington, "Field computation by moment methods," *Wiley-IEEE Press*, 1993.

[65] D. R. Wilton, "Computational methods," in *Scattering: Scattering and Inverse Scattering in Pure and Applied Science*, R. Pike and P. Sabbatier, Eds., Academic Press, 2002.

[66] J.-P. Berenger, "A perfectly matched layer for the absorption of electromagnetic waves," *Journal of computational physics*, vol. 114, no. 2, pp. 185–200, 1994.

[67] S. Gedney, "An anisotropic perfectly matched layer-absorbing medium for the truncation of FDTD lattices," *IEEE Transactions on Antennas and Propagation*, vol. 44, no. 12, pp. 1630–1639, 1996.

[68] F. Teixeira and W. Chew, "General closed-form PML constitutive tensors to match arbitrary bianisotropic and dispersive linear media," *Microwave and Guided Wave Letters, IEEE*, vol. 8, no. 6, pp. 223–225, 1998.

[69] J. B. Schneider and C. L. Wagner, "FDTD dispersion revisited: Faster-than-light propagation," *IEEE Microwave and Guided Wave Letters*, vol. 9, no. 2, pp. 54–56, 1999.

[70] W. C. Chew, M. S. Tong, and B. Hu, "Integral equation methods for electromagnetic and elastic waves," *Synthesis Lectures on Computational Electromagnetics*, vol. 3, no. 1, pp. 1–241, 2008.

[71] M. Khayat and D. Wilton, "Numerical evaluation of singular and near-singular potential integrals," *IEEE Transactions on Antennas and Propagation*, vol. 53, no. 10, pp. 3180–3190, 2005.

[72] M. A. Khayat, D. R. Wilton, and P. W. Fink, "An improved transformation and optimized sampling scheme for the numerical evaluation of singular and

near-singular potentials," *IEEE Antennas and Wireless Propagation Letters*, vol. 7, no. 2, pp. 377–380, 2008.

[73] A. G. Polimeridis, F. Vipiana, J. R. Mosig, and D. R. Wilton, "DIRECTFN: Fully numerical algorithms for high precision computation of singular integrals in Galerkin sie methods," *IEEE Transactions on Antennas and Propagation*, vol. 61, no. 6, pp. 3112–3122, 2013.

[74] W. C. Chew, E. Michielssen, J. Song, and J.-M. Jin, "Fast and efficient algorithms in computational electromagnetics," in, Artech House, Inc., 2001.

[75] E Bleszynski, M Bleszynski, and T Jaroszewicz, "Aim: Adaptive integral method for solving large-scale electromagnetic scattering and radiation problems," *Radio Science*, vol. 31, no. 5, pp. 1225–1251, 1996.

[76] V. Jandhyala, E. Michielssen, S. Balasubramaniam, and W. C. Chew, "A combined steepest descent-fast multipole algorithm for the fast analysis of three-dimensional scattering by rough surfaces," *IEEE Transactions on Geoscience and Remote Sensing*, vol. 36, no. 3, pp. 738–748, 1998.

[77] N. Geng, A. Sullivan, and L. Carin, "Multilevel fast-multipole algorithm for scattering from conducting targets above or embedded in a lossy half space," *IEEE Transactions on Geoscience and Remote Sensing*, vol. 38, no. 4, pp. 1561–1573, 2000.

[78] D. V. Ginste, H. Rogier, F. Olyslager, and D. D. Zutter, "A fast multipole method for layered media based on the application of perfectly matched layers - the 2-D case," *IEEE Transactions on Antennas and Propagation*, vol. 52, no. 10, pp. 2631–2640, 2004.

[79] S. Yan, J.-M. Jin, and Z. Nie, "A comparative study of Calderón preconditioners for PMCHWT equations," *IEEE Transactions on Antennas and Propagation*, vol. 58, no. 7, pp. 2375–2383, 2010.

[80] Y. Beghein, K. Cools, F. P. Andriulli, D. De Zutter, and E. Michielssen, "A Calderon multiplicative preconditioner for the PMCHWT equation for scattering by chiral objects," *IEEE Transactions on Antennas and Propagation*, vol. 60, no. 9, pp. 4239–4248, 2012.

[81] R. F. Harrington, "Time-harmonic electromagnetic fields," *Wiley-IEEE Press*, 2001.

[82] A. J. Poggio and E. K. Miller, "Integral equation solutions of three-dimensional scattering problems," in *Computer Tachniques for Electromagnetics*, R. Mittra, Ed., 2nd Edition, Hemisphere, New York, 1987, pp. 159–264.

[83] S. Yan, J. M. Jin, and Z. Nie, "Improving the accuracy of the second-kind Fredholm integral equations by using the Buffa-Christiansen functions," *IEEE Transactions on Antennas and Propagation*, vol. 59, no. 4, pp. 1299–1310, 2011.

[84] S. Rao, D. Wilton, and A. Glisson, "Electromagnetic scattering by surfaces of arbitrary shape," *IEEE Transactions on Antennas and Propagation*, vol. 30, no. 3, pp. 409–418, 1982.

[85] J. R. Mautz and R. F. Harrington, "A combined-source solution for radiation and scattering from a perfectly conducting body," *IEEE Transactions on Antennas and Propagation*, vol. 27, no. 4, pp. 445–454, 1979.

[86] M. M. Botha, "A family of augmented Duffy transformations for near-singularity cancellation quadrature," *IEEE Transactions on Antennas and Propagation*, vol. 61, no. 6, pp. 3123–3134, 2013.

[87] F. Vipiana and D. R. Wilton, "Numerical evaluation via singularity cancellation schemes of near-singular integrals involving the gradient of Helmholtz-type potentials," *IEEE Transactions on Antennas and Propagation*, vol. 61, no. 3, pp. 1255–1265, 2013.

[88] M. M. Botha, "Numerical integration scheme for the near-singular green function gradient on general triangles," *IEEE Transactions on Antennas and Propagation*, vol. 63, no. 10, pp. 4435–4445, 2015.

[89] J. Ma, V. Rokhlin, and S. Wandzura, "Generalized Gaussian quadrature rules for systems of arbitrary functions," *SIAM Journal on Numerical Analysis*, vol. 33, no. 3, pp. 971–996, 1996.

[90] D. R. Wilton and N. J. Champagne, "Evaluation and integration of the thin wire kernel," *IEEE Transactions on Antennas and Propagation*, vol. 54, no. 4, pp. 1200–1206, 2006.

[91] N. J. Champagne, D. R. Wilton, and J. D. Rockway, "The analysis of thin wires using higher order elements and basis functions," *IEEE Transactions on Antennas and Propagation*, vol. 54, no. 12, pp. 3815–3821, 2006.

[92] F. Vipiana, D. R. Wilton, and W. A. Johnson, "Advanced numerical schemes for the accurate evaluation of 4-D reaction integrals in the method of moments," *IEEE Transactions on Antennas and Propagation*, vol. 61, no. 11, pp. 5559–5566, 2013.

[93] P. W. Fink, D. R. Wilton, and M. A. Khayat, "Simple and efficient numerical evaluation of near-hypersingular integrals," *IEEE Antennas and Wireless Propagation Letters*, vol. 7, pp. 469–472, 2008.

[94] M. S. Tong and W. C. Chew, "A novel approach for evaluating hypersingular and strongly singular surface integrals in electromagnetics," *IEEE Transactions on Antennas and Propagation*, vol. 58, no. 11, pp. 3593–3601, 2010.

[95] A. G. Polimeridis, J. M. Tamayo, J. M. Rius, and J. R. Mosig, "Fast and accurate computation of hypersingular integrals in Galerkin surface integral equation formulations via the direct evaluation method," *IEEE Transactions on Antennas and Propagation*, vol. 59, no. 6, pp. 2329–2340, 2011.

[96] A. G. Polimeridis, F. Vipiana, J. R. Mosig, and D. R. Wilton, "Directfn: Fully numerical algorithms for high precision computation of singular integrals in galerkin sie methods," *IEEE Transactions on Antennas and Propagation*, vol. 61, no. 6, pp. 3112–3122, 2013.

[97] L. Gürel and Ö. Ergul, "Singularity of the magnetic-field integral equation and its extraction," *Antennas and Wireless Propagation Letters, IEEE*, vol. 4, pp. 229–232, 2005.

[98] J. H. Moran and S. Gianzero, "Effects of formation anisotropy on resistivity-logging measurements," *Geophysics*, vol. 44, no. 7, pp. 1266–1286, 1979.

[99] A. Abubakar, T. M. Habashy, V. Druskin, L. Knizhnerman, and S. Davydycheva, "A 3D parametric inversion algorithm for triaxial induction data," *Geophysics*, vol. 71, no. 1, G1–G9, 2006.

[100] Z. Xiong, S. Feng, R. Kautz, S. Chandra, N. Altunyurt, and J. Chen, "Multi-GPU accelerated admittance method for high-resolution human exposure evaluation," *IEEE Transactions on Biomedical Engineering*, vol. 62, no. 12, pp. 2920–2930, 2015.

[101] L. Zhong, J. Li, A. Bhardwaj, L. C. Shen, and R. C. Liu, "Computation of triaxial induction logging tools in layered anisotropic dipping formations," *IEEE Transactions on Geoscience and Remote Sensing*, vol. 46, no. 4, pp. 1148–1163, 2008.

[102] D. Wu, J. Chen, and C. R. Liu, "An efficient FDTD method for axially symmetric LWD environments," *IEEE Transactions on Geoscience and Remote Sensing*, vol. 46, no. 6, pp. 1652–1656, 2008.

Appendix A

Gradient of Scalar Potential Layered Medium Green's Function

In the mixed-potential representation, the electric field due to an electric current is denoted as

$$\mathbf{E} = -j\omega\mathbf{A} - \nabla\Phi. \tag{A.1}$$

In order to calculate the scattered field due to induced currents representing by RWG basis functions in layered medium, the gradient of the scalar potential LMGF is needed in the following forms:

$$\mathbf{E} = -j\omega\mu_0 \left\langle \underline{\underline{\mathcal{G}}}^A, \mathbf{J}^s \right\rangle + \frac{1}{j\omega\varepsilon_0} \left(\left\langle \nabla K^\Phi, \nabla' \cdot \mathbf{J}^s \right\rangle + \left\langle \nabla P_z, J_z^s \right\rangle \right), \tag{A.2}$$

where ∇K^ϕ and ∇P_z are the gradient of scalar potential K^ϕ and P_z, respectively. Again, their spectral forms are expressed using transmission line Green's functions and the corresponding Sommerfeld integration should be performed to obtain their spatial forms.

A.1 Gradient of K^ϕ

In the spectral domain, we have K^ϕ expressed as

$$\tilde{K}^\phi = \frac{j\omega\varepsilon_0}{k_\rho^2} \left(V_i^e - V_i^h \right). \tag{A.3}$$

By taking the gradient in the spectral domain, the x and y derivatives become multiplication by $-jk_x$ and $-jk_x$, while the z derivative remains in spatial form so

that

$$\tilde{\nabla}\tilde{K}^{\phi} = \left(-jk_x\hat{\mathbf{x}} - jk_y\hat{\mathbf{y}} + \frac{d}{dz}\hat{\mathbf{z}}\right)\frac{j\omega\varepsilon_0}{k_\rho^2}\left(V_i^e - V_i^h\right), \tag{A.4}$$

Writing the gradient component in each direction, we obtain

$$\left(\tilde{\nabla}\tilde{K}^{\phi}\right)_x = \frac{\omega\varepsilon_0 k_x}{k_\rho^2}\left(V_i^e - V_i^h\right), \tag{A.5}$$

$$\left(\tilde{\nabla}\tilde{K}^{\phi}\right)_y = \frac{\omega\varepsilon_0 k_y}{k_\rho^2}\left(V_i^e - V_i^h\right), \tag{A.6}$$

and

$$\left(\tilde{\nabla}\tilde{K}^{\phi}\right)_z = \frac{d}{dz}\frac{j\omega\varepsilon_0}{k_\rho^2}\left(V_i^e - V_i^h\right). \tag{A.7}$$

Because V_i^p satisfies the transmission line equation Eq. (A.8)

$$\frac{dV_i^\alpha}{dz} = -jk_z^\alpha Z^\alpha I_i^\alpha, \tag{A.8}$$

substituting Eq. (A.8) into Eq. (A.7) yields

$$\left(\tilde{\nabla}\tilde{K}^{\phi}\right)_z = j\omega\varepsilon_0\left(-j\omega\mu_0\mu_t\frac{\left(I_i^e - I_i^h\right)}{k_\rho^2} - \frac{v^e}{j\omega\varepsilon_0\varepsilon_t}I_i^e\right). \tag{A.9}$$

A.2 Gradient of P_z

In spectral domain, P_z is expressed as

$$\tilde{P}_z = \frac{k_0^2\mu'_t}{k_\rho^2}\left(V_v^h - V_v^e\right), \tag{A.10}$$

By taking the gradient operator in the spectral domain,

$$\tilde{\nabla}\tilde{P}_z = \left(-jk_x\hat{\mathbf{x}} - jk_y\hat{\mathbf{y}} + \frac{d}{dz}\hat{\mathbf{z}}\right)\frac{k_0^2\mu'_t}{k_\rho^2}\left(V_v^h - V_v^e\right), \tag{A.11}$$

and writing the components of gradient in each direction, we get

$$\left(\tilde{\nabla}\tilde{P}_z\right)_x = -jk_0^2{\mu'}_t\frac{k_x}{k_\rho^2}\left(V_v^h - V_v^e\right), \tag{A.12}$$

$$\left(\tilde{\nabla}\tilde{P}_z\right)_y = -jk_0^2{\mu'}_t\frac{k_y}{k_\rho^2}\left(V_v^h - V_v^e\right), \tag{A.13}$$

and

$$\left(\tilde{\nabla}\tilde{P}_z\right)_z = k_0^2{\mu'}_t\frac{1}{k_\rho^2}\frac{d}{dz}\left(V_v^h - V_v^e\right). \tag{A.14}$$

Again, the z-component of $\tilde{P}_z$ is expressed using the derivative of V_v^p respect with z. Since V_v^p satisfies the transmission line equation,

$$\frac{dV_v^\alpha}{dz} = -jk_z^\alpha Z^\alpha I_v^\alpha + \delta\left(z - z'\right), \tag{A.15}$$

by substituting Eq. (A.15) into Eq. (A.14), we end up with

$$\left(\tilde{\nabla}\tilde{P}_z\right)_z = -jk_0^2\mu_t'\left(\omega\mu_0\mu_t\frac{\left(I_v^h - I_v^e\right)}{k_\rho^2} + \frac{v^e}{\omega\varepsilon_0\varepsilon_t}I_v^e\right). \tag{A.16}$$

One thing worth mentioning is the delta function $\delta\left(z - z'\right)$ is canceled since the excitation itself is independent of TE or TM polarization.

A.3 Gradient of K^ψ and Q_z

As a dual problem, the magnetic field due to magnetic current is denoted as

$$\mathbf{H} = -j\omega\mathbf{F} - \nabla\Psi, \tag{A.17}$$

In layered medium, it has the form

$$\mathbf{H} = -j\omega\varepsilon_0\left\langle\underline{\underline{\mathcal{G}}}^F, \mathbf{M}^s\right\rangle + \frac{1}{j\omega\mu_0}\left(\left\langle\nabla K^\Psi, \nabla'\cdot\mathbf{M}^s\right\rangle + \left\langle\nabla Q_z, M_z^s\right\rangle\right), \tag{A.18}$$

where ∇K^{ψ} and ∇Q_z are the gradients of the scalar potential K^{ψ} and Q_z, respectively. By repeating the same exercise above or imposing duality principle, the gradient of K^{ψ} is

$$\left(\tilde{\nabla}\tilde{K}^{\Psi}\right)_x = \frac{\omega\mu_0 k_x}{k_\rho^2}\left(I_v^h - I_v^e\right), \tag{A.19}$$

$$\left(\tilde{\nabla}\tilde{K}^{\Psi}\right)_y = \frac{\omega\mu_0 k_y}{k_\rho^2}\left(I_v^h - I_v^e\right), \tag{A.20}$$

$$\left(\tilde{\nabla}\tilde{K}^{\Psi}\right)_z = -j\omega\mu_0\left[j\omega\varepsilon_0\varepsilon_t\frac{V_v^h - V_v^e}{k_\rho^2} + \frac{V_v^h}{j\omega\mu_0\mu_z}\right], \tag{A.21}$$

and that of Q_z is

$$\left(\tilde{\nabla}\tilde{Q}_z\right)_x = \frac{-jk_0^2\varepsilon'_t k_x}{k_\rho^2}\left(I_i^e - I_i^h\right), \tag{A.22}$$

$$\left(\tilde{\nabla}\tilde{Q}_z\right)_y = \frac{-jk_0^2\varepsilon'_t k_y}{k_\rho^2}\left(I_i^e - I_i^h\right), \tag{A.23}$$

$$\left(\tilde{\nabla}\tilde{Q}_z\right)_z = k_0^2\varepsilon'_t\left(-j\omega\varepsilon_0\varepsilon_t\frac{V_i^e - V_i^h}{k_\rho^2} + \frac{V_i^h}{j\omega\mu_0\mu_z}\right). \tag{A.24}$$

In order to perform the Sommerfeld integration, the singularity extraction method and the weighted average method described in Chapter 2 can be reused. All the Sommerfeld and related identities needed to calculate the closed-form extracted terms can be easily found in previous introduced identities from A to Q. They are also listed in Appendix C for reference.

Appendix B

Two-Level Asymptotic Transmission Line Green's Function

The asymptotic transmission line Green's function is listed in this appendix. From the wavenumber dispersion relationship, it's easily seen that when $k_\rho > k_t$, we have

$$k_z^\alpha = \sqrt{k_t^2 - v_\alpha k_\rho^2} = -j\sqrt{v_\alpha k_\rho^2 - k_t^2}, \tag{B.1}$$

hence the all voltage and current on the transmission line decay exponentially away from a source at $z = z'$. They behave as

$$e^{-|k_z^\alpha||z-z'|}. \tag{B.2}$$

This suggests the Sommerfeld integration over the spectral variable k_ρ converges exponentially if there is a separation between source and observation planes. When the source and observation points are not well separated, i.e. z and z' are in the same or adjacent layers, the integrand doesn't decay fast enough for efficient numerical computation. In this case, the integral can be accelerated by removing its spectral asymptotic form in spectral domain and adding the extracted term back in the spatial domain using the SIRs listed in appendix C.

A) $n = m$

When the observation and source point are in the same layer, the multi-reflection back and forth from layer boundaries can be ignored and we only consider three parts in the asymptotic forms of the transmission line quantities: direct part, first reflected parts from lower and upper boundaries.

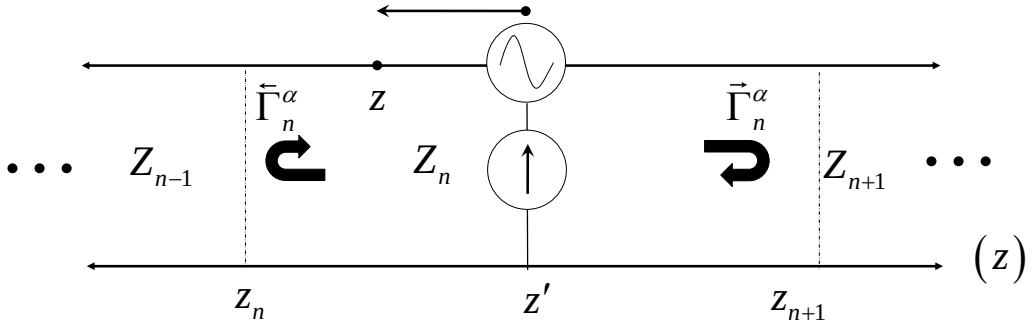

Figure B.1. Asymptotic forms of transmission line Greens functions when both source and observation points are located in the same layer.

$$V_{\mathrm{i}}^{\alpha,\infty} = \frac{Z_n^{\alpha}}{2}\left[e^{-jk_{zn}\varsigma_1} + \overleftarrow{\Gamma}_n^{\alpha,\infty} e^{-jk_{zn}\varsigma_2} + \overrightarrow{\Gamma}_n^{\alpha,\infty} e^{-jk_{zn}\varsigma_3}\right], \tag{B.3}$$

$$I_{\mathrm{i}}^{\alpha,\infty} = \frac{1}{2}\left[\pm e^{-jk_{zn}\varsigma_1} + \overleftarrow{\Gamma}_n^{\alpha,\infty} e^{-jk_{zn}\varsigma_2} - \overrightarrow{\Gamma}_n^{\alpha,\infty} e^{-jk_{zn}\varsigma_3}\right], \tag{B.4}$$

$$V_{\mathrm{v}}^{\alpha,\infty} = \frac{1}{2}\left[\pm e^{-jk_{zn}\varsigma_1} - \overleftarrow{\Gamma}_n^{\alpha,\infty} e^{-jk_{zn}\varsigma_2} + \overrightarrow{\Gamma}_n^{\alpha,\infty} e^{-jk_{zn}\varsigma_3}\right], \tag{B.5}$$

$$I_{\mathrm{v}}^{\alpha,\infty} = \frac{1}{2Z_n^{\alpha}}\left[e^{-jk_{zn}\varsigma_1} - \overleftarrow{\Gamma}_n^{\alpha,\infty} e^{-jk_{zn}\varsigma_2} - \overrightarrow{\Gamma}_n^{\alpha,\infty} e^{-jk_{zn}\varsigma_3}\right], \tag{B.6}$$

where $\varsigma_1 = |z - z'|$, $\varsigma_2 = |z + z' - 2z_n|$, and $\varsigma_3 = |2z_n - z - z'|$ is the traveling distances of each wave component, respectively.

B) $n = m \pm 1$

when the source and observation are in the adjacent layers, we only consider the transmitted contribution. The asymptotic transmission line voltage and current can be written as

$$V_{\mathrm{i}}^{\alpha,\infty} = \frac{Z_n^{\alpha}}{2}\left[e^{-jk_{zn}\varsigma_1}\left(1 + \overrightarrow{\overleftarrow{\Gamma}}_n^{\alpha,\infty}\right)\right], \tag{B.7}$$

$$I_{\mathrm{i}}^{\alpha,\infty} = \frac{1}{2}\left[\pm e^{-jk_{zn}\varsigma_1}\left(1 - \overrightarrow{\overleftarrow{\Gamma}}_n^{\alpha,\infty}\right)\right], \tag{B.8}$$

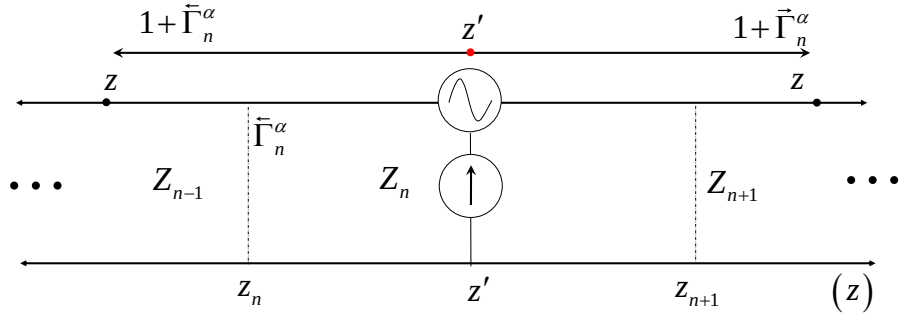

Figure B.2. Asymptotic forms of transmission line Greens functions when source and observation points are located in adjacent layers.

$$V_{\mathrm{v}}^{\alpha,\infty} = \frac{1}{2}\left[\pm e^{-jk_{zn\varsigma 1}}\left(1+\overleftrightarrow{\Gamma}_n^{\alpha,\infty}\right)\right], \tag{B.9}$$

$$I_{\mathrm{v}}^{\alpha,\infty} = \frac{1}{2Z_n^{\alpha}}\left[e^{-jk_{zn\varsigma 1}}\left(1-\overleftrightarrow{\Gamma}_n^{\alpha,\infty}\right)\right]. \tag{B.10}$$

Since the asymptotic reflection coefficient derived in chapter 5 is

$$\Gamma^{\alpha,\infty}(k_\rho) = \Gamma^{\alpha,1,\infty} + \frac{1}{k_\rho^2}\Gamma^{\alpha,2,\infty} + \mathrm{O}\left(k_\rho^{-4}\right), \tag{B.11}$$

if we substitute the expanded reflection coefficient $\Gamma^{\alpha,\infty}$ to the above TLGFs and regroup the terms by their decaying order respect to k_ρ, different levels of asymptotic coefficient of TLGFs can be obtained.

B.0.1 Two-Level Asymptotic Coefficient of TLGFs

Accordingly, if we write $V_{\mathrm{i}}^{\alpha,\infty}$ in the two-level asymptotic form

$$V_{\mathrm{i}}^{\alpha,\infty} = v_{\mathrm{i}}^{\alpha,1,\infty} + \frac{1}{k_\rho^2}v_{\mathrm{i}}^{\alpha,2,\infty}, \tag{B.12}$$

by ignoring the higher-order coefficients in Eq. (B.11), we can obtain the first-level asymptotic coefficient of $V_{\mathrm{i}}^{\alpha,\infty}$ coming from reflected terms. The direct term should also be included in the first-level asymptotic coefficient because it has the same

decaying order respect to k_ρ.

B) $n = m$

Hence when the source and observation point are in the same layer $n = m$, the first-level asymptotic coefficient of $V_{\mathrm{i}}^{\alpha,\infty}$ is

$$v_{\mathrm{i}}^{\alpha,1,\infty} = \frac{Z_n^\alpha}{2}\left[e^{-jk_{zn}\varsigma_1} + \overleftarrow{\Gamma}_n^{\alpha,1,\infty} e^{-jk_{zn}\varsigma_2} + \overrightarrow{\Gamma}_n^{\alpha,1,\infty} e^{-jk_{zn}\varsigma_2}\right]. \tag{B.13}$$

The second-level asymptotic coefficient of $V_{\mathrm{i}}^{\alpha,\infty}$ only comes from the reflected terms

$$v_{\mathrm{i}}^{\alpha,2,\infty} = \frac{Z_n^\alpha}{2}\left[\overleftarrow{\Gamma}_n^{\alpha,2,\infty} e^{-jk_{zn}\varsigma_2} + \overrightarrow{\Gamma}_n^{\alpha,2,\infty} e^{-jk_{zn}\varsigma_3}\right]. \tag{B.14}$$

B) $n = m \pm 1$

When the source and observation point are located in adjacent layers $\ell = \ell' \pm 1$, we only consider the transmitted waves that are the first-level and second-level asymptotic coefficient of $V_{\mathrm{i}}^{\alpha,\infty}$

$$v_{\mathrm{i}}^{\alpha,1,\infty} = \frac{Z_n^\alpha}{2}\left(1 + \overrightleftarrows{\Gamma}_n^{\alpha,1,\infty}\right) e^{-jk_{zn}\varsigma_1}, \tag{B.15}$$

and

$$v_{\mathrm{i}}^{\alpha,2,\infty} = \frac{Z_n^\alpha}{2}\overrightleftarrows{\Gamma}_n^{\alpha,2,\infty} e^{-jk_{zn}\varsigma_1}, \tag{B.16}$$

respectively. The two-level asymptotic coefficients for other components, i.e. I_{i}, V_{v}, I_{v} can be derived similarly.

Appendix C

Summary of Sommerfeld and Related Identities

Defining

$$G^\alpha = \frac{e^{-jk_t R^\alpha}}{4\pi R^\alpha}, R^\alpha = \sqrt{\rho^2/\nu^\alpha + z^2}, \eta = 1 + jk_t R^\alpha, p^\alpha = e^{-jk_z^\alpha |\varsigma|} \tag{C.1}$$

All the Sommerfeld and related identities are summarized here.

$$I_A = S_0 \left\{ \frac{p^\alpha}{2jk_z^\alpha} \right\} = \frac{1}{\nu^\alpha} G^\alpha \tag{C.2}$$

$$I_B = S_0 \left\{ \frac{p^\alpha}{2} \right\} = \frac{|\varsigma|\,\eta}{\nu^p (R^\alpha)^2} G^\alpha \tag{C.3}$$

$$I_C = S_0 \left\{ \frac{jk_z^\alpha p^\alpha}{2} \right\} = \frac{G^\alpha}{(R^\alpha)^2} \left(\varsigma^2 \frac{3\eta - (k_t R^\alpha)^2}{\nu^\alpha (R^\alpha)^2} - \frac{\eta}{\nu^\alpha} \right) \tag{C.4}$$

$$I_D = S_0 \left\{ \frac{k_\rho^2 p^\alpha}{2\,(jk_z^\alpha)} \right\} = \frac{k_t^2 I_A + I_C}{v^\alpha} \tag{C.5}$$

$$I_E = S_1 \left\{ \frac{p^\alpha}{2k_\rho} \right\} = \frac{R^\alpha e^{-jk_t|\varsigma|} - |\varsigma|\, e^{-jk_t R^\alpha}}{4\pi\rho R^\alpha} \tag{C.6}$$

$$I_F = S_1 \left\{ \frac{k_\rho p^\alpha}{2jk_z^\alpha} \right\} = \frac{\rho\eta}{(\nu^\alpha)^2} \frac{G^\alpha}{(R^\alpha)^2} \tag{C.7}$$

$$I_G = S_1 \left\{ \frac{k_\rho p^\alpha}{2} \right\} = \frac{1}{(\nu^\alpha)^2} \frac{\rho\,|\varsigma|}{R^\alpha} \frac{3\eta - (k_t R^\alpha)^2}{(R^\alpha)^3} G^\alpha \tag{C.8}$$

$$I_H = S_1 \left\{ \frac{jk_z^\alpha p^\alpha}{2k_\rho} \right\} = \frac{jk_t e^{-jk_t|\varsigma|}}{4\pi\rho} + \frac{\rho_v^2 - jk_t R^\alpha |\varsigma|^2}{(R^\alpha)^2} \frac{G^\alpha}{\rho} \tag{C.9}$$

$$I_I = S_1 \left\{ \frac{p^\alpha}{2jk_z^\alpha k_\rho} \right\} = \frac{e^{-jk_t|\varsigma|} - e^{-jk_t R^\alpha}}{4\pi jk_t\rho} \tag{C.10}$$

$$I_J = S_2 \left\{ \frac{jk_z^\alpha p^\alpha}{2} \right\} = \frac{2}{\rho} I_H - I_C \tag{C.11}$$

$$I_K = S_2 \left\{ \frac{p^\alpha}{2jk_z^\alpha} \right\} = \frac{2}{\rho} I_I - I_A \tag{C.12}$$

$$I_L = S_2 \left\{ \frac{p^\alpha}{2} \right\} = \frac{2}{\rho} I_E - I_B \tag{C.13}$$

$$I_M = S_0 \left\{ \frac{p^\alpha}{2(jk_z^\alpha)^2} \right\} = \frac{1}{\nu^\alpha} \int_{|\varsigma|}^{\infty} \frac{e^{-jk_t R^\alpha}}{4\pi R^\alpha} ds \tag{C.14}$$

$$I_N = S_0 \left\{ \frac{p^\alpha}{2(jk_z^\alpha)^3} \right\} = -\frac{1}{\nu^\alpha} \left[j \frac{e^{-jk_t R^\alpha}}{4\pi k_t} + |\varsigma| \, G_z^\alpha \left(\rho, |\varsigma|\right) \right] \tag{C.15}$$

$$I_O = S_1 \left\{ \frac{p^\alpha}{2jk_z^\alpha k_\rho} \right\} = \frac{e^{-jk_t|\varsigma|} - e^{-jk_t R^\alpha}}{4\pi j k_t \rho} \tag{C.16}$$

$$I_P = S_1 \left\{ \frac{p^\alpha}{2(jk_z^\alpha)^2 k_\rho} \right\} = \frac{1}{4\pi j k_t \rho} \left(\frac{e^{-jk_t|\varsigma|}}{jk_t} - \int_{|\varsigma|}^{\infty} e^{-jk_t R^\alpha} dz \right) \tag{C.17}$$

$$I_Q = S_2 \left\{ \frac{p^\alpha}{2(jk_z^\alpha)^2} \right\} = \frac{2}{\rho} I_P - I_M \tag{C.18}$$